

1-1-2013

# Engineering Nanoparticle And Nanoring Patterns For The Study Of Molecular Crystallization Under Nanoconfinement

Sunxi Wang  
*Wayne State University,*

Follow this and additional works at: [http://digitalcommons.wayne.edu/oa\\_dissertations](http://digitalcommons.wayne.edu/oa_dissertations)

---

## Recommended Citation

Wang, Sunxi, "Engineering Nanoparticle And Nanoring Patterns For The Study Of Molecular Crystallization Under Nanoconfinement" (2013). *Wayne State University Dissertations*. Paper 806.

This Open Access Dissertation is brought to you for free and open access by DigitalCommons@WayneState. It has been accepted for inclusion in Wayne State University Dissertations by an authorized administrator of DigitalCommons@WayneState.

**ENGINEERING NANOPARTICLE AND NANORING PATTERNS FOR THE  
STUDY OF MOLECULAR CRYSTALLIZATION UNDER NANOCONFINEMENT**

by

**SUNXI WANG**

**DISSERTATION**

Submitted to the Graduate School

of Wayne State University,

Detroit, Michigan

in partial fulfillment of the requirements

for the degree of

**DOCTOR OF PHILOSOPHY**

2013

MAJOR: CHEMICAL ENGINEERING

Approved by:

---

Advisor

Date

---

---

---

## ACKNOWLEDGMENTS

First of all, I would love to deeply appreciate my advisor, Dr. Guangzhao Mao, for all of her generous help and support during past five years and also for the trust she had in me when enrolling me into her group.

I also wish to thank all of my research group members, Dr. Yanhua Zhang, Mr. Yi Zou, Ms. Li Li, Mr. Pedram Jahanian, and Ms. Lingxiao Xie, for their beneficial discussions during our group meetings and daily experiments.

I would like to thank my collaborators, Dr. Bhanu Jena, Dr. Weiping Ren, and Dr. Alan Hudson, for providing novel samples for me to characterize and the opportunity of approaching many interesting research areas.

I also wish to thank my committee members, Dr. Steve Salley, Dr. Yong Xu, and Dr. Rangaramanujam Kannan for their helpful suggestions and valuable recommendations related to this dissertation.

Finally, I wish to express my sincere gratitude to my family for their love, patience, and encouragement.

## TABLE OF CONTENTS

|  |    |
|--|----|
| Acknowledgements.....  | ii |
| CHAPTER 1 Introduction.....  | 1  |
| CHAPTER 2 Literature review.....   | 5  |
| 2.1. Inorganic/organic nanohybrids.....  | 5  |
| 2.1.1. Applications and synthesis methods.....                                       | 5  |
| 2.1.2. SMN and nanoconfinement.....  | 6  |
| 2.2. Crystallization nanoconfinement on GNP seeds.....                               | 8  |
| 2.2.1. Synthesis (size/shape control).....   | 8  |
| 2.2.2. Surface modification.....   | 11 |
| 2.2.3. Immobilization and array formation.....                                       | 13 |
| 2.3. Crystallization nanoconfinement on nanopatterns by particle<br>lithography..... | 18 |
| 2.3.1. Organosilane nanopatterns.....  | 18 |
| 2.3.2. Pattern controlled crystallization.....                                       | 21 |
| CHAPTER 3 Experimental.....  | 23 |
| 3.1. Atomic force microscope.....  | 23 |
| 3.2. TEM (EDS), FE-SEM.....  | 24 |
| 3.3. UV-Vis, FT-IR.....  | 26 |
| 3.4. PXRD, TGA, and contact angle.....   | 27 |
| 3.5. DLS, ICP-MS.....  | 29 |
| 3.6. Conclusions.....  | 29 |
| CHAPTER 4 Formation of carboxylic acid nanorods on OA-GNPs.....                      | 31 |

|  |    |
|--|----|
| 4.1. Introduction.....   | 31 |
| 4.2. Experimental.....   | 33 |
| 4.3. Results and discussion.....   | 35 |
| 4.3.1. NP characterization.....  | 35 |
| 4.3.2. Film structure of n-carboxylic acids on HOPG.....   | 43 |
| 4.3.3. Film structure of n-carboxylic acids on HOPG in the presence<br>of OA-GNPs.....                   | 45 |
| 4.4. Conclusions.....  | 54 |
| CHAPTER 5 A supra-monolayer nanopattern for organic NP array deposition...                               | 56 |
| 5.1. Introduction.....   | 56 |
| 5.2. Experimental.....   | 59 |
| 5.3. Results and discussion.....   | 63 |
| 5.3.1. Supra-monolayer nanopattern formation by particle<br>lithography.....                             | 63 |
| 5.3.2. Supra-monolayer nanoring nanopattern used for organic NP<br>deposition.....                       | 76 |
| 5.4. Conclusions.....  | 87 |
| CHAPTER 6 GNP synthesis, characterization, and interaction with macrophage<br>for immune modulation..... | 89 |
| 6.1. Introduction.....   | 89 |
| 6.2. Experimental.....   | 89 |
| 6.3. Results and discussion.....   | 93 |
| 6.3.1. Purification of the synthesized GNP solution.....   | 93 |

|  |     |
|--|-----|
| 6.3.2. Physical characterization of the GNPs.....              | 96  |
| 6.3.3. THP-1 cell uptake and response to the GNPs.....         | 98  |
| 6.4. Conclusions.....  | 104 |
| CHAPTER 7 Conclusions and recommendations for future work..... | 105 |
| 7.1. Conclusions.....  | 105 |
| 7.2. Recommendations for future work.....                      | 106 |
| Appendix.....  | 107 |
| References.....  | 109 |
| Abstract.....  | 121 |
| Autobiographical Statement.....                                | 122 |

## CHAPTER 1

### INTRODUCTION

In today's nanotechnology research field, inorganic/organic nanohybrid structures have drawn great interests as they combine or enhance the functionalities from the different origins. The high surface area to volume ratio and size effect of the nanomaterials provide unique physical and chemical properties, such as optical, electrical, and magnetic properties, as opposed to bulk materials. This enables various applications in many fields such as optical, electronic devices and sensors. Although a lot of research has been carried out to generate novel hybrid structures, incorporating the two components with controllable properties and geometry still remains very challenging. The underlying mechanism for generating nanohybrids in this work is seed-mediated nucleation (SMN) based nanoconfinement. The crystallization happens at nanoscale, which could be different from bulk state. If we could reveal the fundamental for nanocrystallization, then we would be able to reach a universal strategy to fabricate nanohybrids.

This dissertation focuses on the molecular crystallization directed by nanoparticles (NPs) and nanoring patterns. The effects of NP size and surface functionality on nucleation and crystal growth of molecular crystals are investigated through a variety of surface and nanomaterial characterization methods, including atomic force microscopy (AFM), powder X-ray diffraction (PXRD), and field emission scanning electron microscope (FE-SEM). Gold NPs (GNPs) with different sizes, shapes, and capping ligands are synthesized to

examine the universality of this hypothesis. Also, different molecular crystalline materials have been tested.

For generating nanopatterns such as nanorings, facile and low cost particle lithography method have been adopted by using latex nanospheres and organosilanes' chemical vapor deposition (CVD). Several drug molecules, including 2-acetoxybenzoic acid (aspirin), show potential in forming ordered nanocrystals inside "nano-flasks" for high throughput screening applications in pharmaceutical industries.

Besides the crystallization under nanoconfinement, in-house synthesized citrate capped GNPs have also been tested for immune response of macrophages, such as THP-1 cells. By studying this, the potential uses of low cytotoxicity GNPs in drug delivery can be explored.

This dissertation is organized as follows:

Chapter 2 presents the literature review and background for this research. Three topics have been surveyed, including nanohybrid fabrication with SMN, GNP synthesis and characterizations, and nanopattern generation for high throughput screening.

Chapter 3 describes the detailed characterization techniques and the instruments involved in this study. They include: AFM, Transmission Electron Microscope (TEM), in situ Energy Dispersive X-ray Spectroscopy (EDS), FE-SEM, Fourier Transform Infrared Spectroscopy (FT-IR), Ultraviolet-Visible spectrometry (UV-Vis), PXRD, Thermogravimetric Analysis (TGA), and contact angle.



Chapter 4 illustrates the formation of carboxylic acid nanorods on oleylamide-capped GNPs (OA-GNPs). A methyl-terminated GNP, whose interaction with the crystallizing unit was limited to the dispersive interaction, was employed. GNPs are not subject to photo-induced aggregation, making it easier to perform crystallization experiments. The AFM results demonstrate that dispersive interactions alone can support the seed-mediated mechanism of nanorod formation.

Chapter 5 demonstrates a supra-monolayer nanopattern for organic NP array depositions. This study explores the competitive nature of the surface condensation vs. polymerization reactions of the organosilane molecules on oxidized silicon substrates covered by the lithographical colloidal layers. The supra-monolayer patterns are used as “nano-flasks” to induce area-selective precipitation and nucleation of small organic molecules. We demonstrate that nucleation is influenced by nanoconfinement imposed by nanopatterns and NP nucleation seeds.

Chapter 6 depicts GNP syntheses, characterizations, and interactions with macrophages for immune modulation. The overall goal of this part is to use GNP based materials to modulate immune responses by targeting immune cells. The specific aim is to establish a baseline of macrophage cell uptake and cytokine expression of GNPs of sizes 5, 15, 40, and 65 nm. GNPs have been synthesized and characterized by using a variety of physical characterization methods, and obtained preliminary results on cell uptake and cytokine expression.

Finally in Chapter 7, the conclusions from this study and recommendations for future research are discussed. The overall conclusion is the self-assembled method for fabricating nanohybrids based on SMN has been demonstrated as successful. The novel "nano-flasks" used for nanoconfining drug crystals could be potentially used in high throughput screening.

## CHAPTER 2

### LITERATURE REVIEW

#### 2.1. Inorganic/organic nanohybrids

##### 2.1.1. Applications and synthesis methods

Nature makes inorganic/organic nanohybrids via the biomineralization process, where inorganic crystallization is directed by protein matrices, such as bones and seashells. Many research groups have adopted the biomimetic approach for creating functional nanohybrid materials. For example, room-temperature hybrid light-emitting devices are realized by the incorporation of a dye molecule within a perovskite framework.<sup>1</sup> As the inorganic/organic nanohybrids show many interesting properties, fabricating the functional hybrid systems has drawn great attention. Below are two examples of the nanohybrid applications.

Martins and co-workers<sup>2</sup> reported the synthesis of polystyrene (PS) containing organically capped GNP composites. The optical features of such hybrid structures were dominated by plasmonic effects that depended on the morphology of the nanocomposite. Two well-known effects, interparticle plasmonic coupling and variation of the surrounding dielectric refractive index, were involved in the GNPs. This research provided a general strategy to produce optical-responsive nanocomposites via controlling the morphology of polymer submicro-particles containing GNPs.

Shi and co-workers<sup>3</sup> made gold/carbon nanotubes' (CNTs) hybrid catalysts by modifying CNTs and attaching GNPs in one step. TEM images indicated uniform dispersion of the GNPs on the CNTs surfaces, which enhanced the electrochemical catalytic activity of Gold/CNT hybrids for oxygen reduction reactions. The Gold/CNT hybrids had potential applications in sensors, optical electronics, electrocatalysis, and proton exchange membrane fuel cells.

Another example<sup>4</sup> is growing organic crystals from inorganic particles based on SMN via fast solvent evaporation developed by our group, which is opposite from the biomineralization existing in the nature as protein manipulates bone growth in our body. AFM images show eicosanoic acid ( $C_{20}A$ ) nanorods forming from 11-mercaptoundecanoic acid (MUA) capped CdSe NPs upon spin coating their mixture of alcoholic solution onto Highly Oriented Pyrolytic Graphite (HOPG) substrate. The nanorods have uniform width and height. On the other hand, the carboxylic acids form 2D epitaxial layer patterns on HOPG in the absence of the NPs. During the solvent's fast evaporation, carboxylic acid molecules crystallize from the NP surface into nanorods.

### **2.1.2. SMN and nanoconfinement**

Nanohybrid structures composed of inorganic and organic parts are capable of controlling the desired optical and electrical properties by adjusting the chemical composition and geometry of individual components. A remaining challenge is incorporating the individual parts to form nanohybrid structures. One possible method is to grow organic crystals from inorganic particles based on

SMN via solvent evaporation developed by our group. Another possible method is to use electrochemistry to generate these nanohybrids.

In heterogeneous SMN, a foreign seed lowers the nucleation energy barrier to promote nucleation at supersaturation below the bulk one.<sup>5</sup> The critical nucleation energy  $\Delta G_c^{\text{het}}$  is lowered through the contact angle  $\theta$  between the cap-shaped nucleus and the seed surface. The nucleation energy barrier ratio  $f = \Delta G_c^{\text{het}} / \Delta G_c$ , is used to describe the degree of nucleation barrier lowering due to the foreign particle.  $f$  is a function of  $m$  and  $R'$ .  $m = (\gamma_{\text{sf}} - \gamma_{\text{sc}}) / \gamma_{\text{cf}} \approx \cos\theta$ , ( $-1 \leq m \leq 1$ ) is related to the contact angle;  $R' = R^s / r_c$  is the dimensionless radius, which equals the radius of curvature of the foreign body  $R^s$  scaled by the critical nucleus radius  $r_c$ .<sup>6</sup> The nucleus radius needs to be larger than  $r_c$  to overcome the energy barrier and grow into a stable crystal.  $f$  is the function of  $R'$  for several given  $m$  values. When  $R' > 10$ ,  $f$  is only a function of  $m$ . The foreign body acts as a flat substrate showing no curvature effect. When  $R' < 0.1$ ,  $f$  is a quasi-constant close to 1. The foreign body is ineffective upon nucleation. When  $10 > R' > 0.1$ ,  $f$  will decrease with increasing  $m$  and  $R'$  (equivalent to decreasing  $r_c$ ).

The molecular simulations carried out by Cacciuto and co-workers<sup>7</sup> showed that SMN occurs only when the radius of the seed particle is at least five times of the diameter of the colloidal particle, and the 1D narrow rod grows radially from the seed. When the seed radius was increased to seven times of the colloid size, the initial colloidal cluster tended to wrap around the seed as a 2D layer. In addition, when the colloid size increased to make the ratio smaller

than 7, the cluster became a radially oriented “1D” rod again. It was assumed that the molecular rod was induced by the high curvature of the small seed.

Nanoconfinement is a phenomenon induced by a space measured in nanometers. Some processes (such as crystallization) are confined in the nanoscale volume size and hence lead to different and unique results as opposed to the bulk or even microscale conditions. This nanoconfinement effect probes the impact of size and shape of the critical nucleus on crystal growth. Therefore there are unique mechanisms underlying the organic crystals’ growth from the NPs, resulting in different morphologies and structures.

Therefore when in nanoscale, the NPs shape and size are both playing important roles in the crystallization process. Due to the nanoconfinement effect, crystals with new polymorphism or constrained geometry may be created. The proposed research will explore the science behind NP-mediated nucleation of organic crystals and its electrochemical applications.

## **2.2. Crystallization nanoconfinement on GNP seeds**

### **2.2.1. Synthesis (size/shape control)**

GNPs will be used as model NPs because of their stability, conductivity, and extensive knowledge on its synthesis and surface modification.

The simplest synthesis method is the Turkevich method (one phase in water).<sup>8</sup> Generally this is used to produce relatively monodisperse spherical GNPs with average size in the range of 10-30 nm in aqueous solution. Synthesis of larger particles results in poorer size and shape control. In a typical reaction,

50ml 0.01% (w/v) of boiled chloroauric acid ( $\text{HAuCl}_4$ ) aqueous solution are mixed with 1.75 ml 1% (w/v) of trisodium citrate ( $\text{Na}_3\text{C}_6\text{H}_5\text{O}_7$ ) aqueous solution to form ~12 nm average diameter GNPs as the citrate ions act as both the reducing (to reduce  $\text{Au}^{3+}$  to  $\text{Au}^0$ ) and capping agent (to prevent aggregation of Gold atoms).

The Brust method (two phases between water and toluene)<sup>9</sup> allows GNPs synthesis to be compatible with organic solvents. The method produces GNPs with diameter in the range of 5 and 10 nm. In a typical reaction, 30 ml 30 mM  $\text{HAuCl}_4$  aqueous solution is mixed with 80 ml 50 mM tetraoctylammonium bromide (TOAB) in toluene to allow  $\text{AuCl}_4^-$  transfer into the organic phase. Then a freshly prepared sodium borohydride ( $\text{NaBH}_4$ ) aqueous solution (25 ml, 0.4 M) is slowly added with vigorously stirring.  $\text{NaBH}_4$  is the reducing agent, and TOAB is both the phase transfer catalyst and stabilizing agent. TOAB's capping makes GNPs hydrophobic and enables them to be transferred from water phase into toluene phase.

Our previous studies show that ~8 nm MUA capped CdSe NPs and 4-20 nm GNPs have the ability to nucleate  $\text{C}_{20}\text{A}$  nanorods with typical dimension of 50-250 nm in length and ~1 nm in height upon spin coating on graphite substrate. These results indicate that NPs in the size range of about 5-20 nm exert confinement effects on molecular crystallization. Therefore we synthesize monodisperse GNPs with core diameter in the range of 3-30 nm, e.g., overall particle size of 5, 15, 40, and 65 nm, respectively. Wine-red color could be used as an initial judgment of whether GNPs are synthesized in the right size range.

Plus AFM and TEM are used as the main tools to obtain the statistical average size for GNPs.

The method developed by Frens<sup>10</sup> in 1973 and modified by Grabar<sup>11</sup> in 1995, as a derivative of the Turkevich method, varies the ratio of initial concentration of sodium citrate to gold salt to change the gold core size. The variation in the ratio changes the reduction rate leading to the different critical nucleation size, which in turn leads to the different final particle average diameters. For instance, adding 1.0 mL of 34 mM sodium citrate solution to a boiled 50 mL of  $2.5 \times 10^{-4}$  M chloroauric acid solution will grow controlled sizes of 16 nm; however, a 1.25 ml sodium citrate solution with the same concentration will lead to ~13 nm average size GNPs. From the relationship graphed by Goodman and co-workers<sup>12</sup> in 1981, we can synthesize different sizes by adding different amount of 1% (w/v) sodium citrate aqueous solution into boiling 50 ml of 0.01% (w/v) HAuCl<sub>4</sub> aqueous solution.

Another aspect of the NPs that will be addressed is the shape effect upon the nucleation process. Cubic GNPs capped with polymer synthesized by Seo and co-workers<sup>13</sup> could be tested to determine whether the nanorods are induced by the local curvature at the seed surface. Also cubic NPs may provide a way to control the nanorods' growth directions which could lead to the ultimate goal of fabricating organic network nanostructures. Carboxylic acid capped buckyball synthesized by Cheng's group<sup>14</sup> at The University of Akron could also be a candidate for shape effect study. Since buckyball's diameter is 1.1 nm which is ideally spherical even at angstrom level (different from several nanometer's



GNPs which have a gold atom plane due to the closed packing structure), this system and cubic GNPs could be considered as two extreme cases to study shape effects. Basically, similar nanorods are expected to grow from both kinds of the NPs and further conclusions will be drawn from the future results.

### **2.2.2. Surface modification**

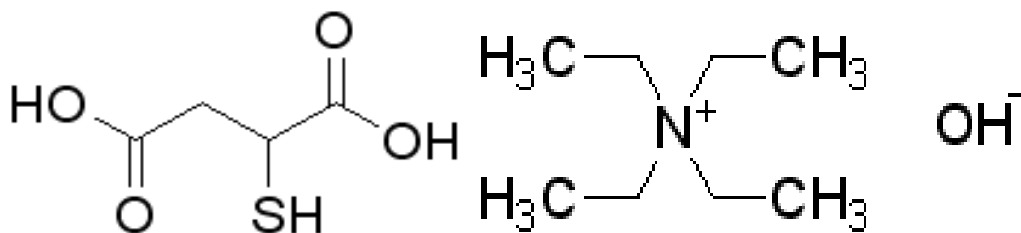
Since neither citrate ion nor TOAB binds strongly to the gold core, it can be replaced with a stronger binding agent such as an alkanethiol, in which sulfur will bind to gold surface covalently with relatively high bonding energy of ~418 kJ/mol to produce a considerably stable GNP dispersion. Mirkin and co-workers<sup>15</sup> developed a synthetic route for making trithiol terminated oligonucleotides, which could be used to prepare more stable DNA-GNP conjugates compared to the monothiol- or dithiol- capped ones proved by the time evolution of UV-Vis spectra.

In the case of synthesizing MUA-GNPs from the citrate-GNPs as discussed by Lin and co-workers,<sup>16</sup> MUA's thiol group strongly bonded onto Gold surfaces (leave the -COOH group as the outmost layer) to replace citrate ions, and then formed a quasi-monolayer on the spherical shaped NPs. They also used a similar method to make other kinds of thiol capped GNPs such as 11-mercaptoundecylamine (MUAM, HS(CH<sub>2</sub>)<sub>11</sub>NH<sub>2</sub>). They concluded that the steric hindrance of long chain capping molecules provided more stable gold colloidal dispersions.

As the surface functional group changes, suitable solvents for dissolving the GNPs need to be chosen, which makes the spin coating method more

difficult since it requires the well dispersed mixture solution of both GNPs and C<sub>20</sub>A. Based on several drawbacks we have discussed, the more controllable and reproducible method of electrochemically fabricating nanohybrids was brought to the table. Nevertheless, if we are able to immobilize GNPs onto the substrates, then the organic nanorods' formation will be isolated from the mixture solution's fast evaporation, which will make the whole process more in control.

Another method for synthesizing carboxylic thiol capped GNPs in aqueous medium has been developed by Chen and Kimura.<sup>17</sup> In a typical reaction, 0.5 mmol of HAuCl<sub>4</sub> was dissolved as a 5% (w/v) aqueous solution and mixed with 100 ml methanol solution of 0.25 mmol mercaptosuccinic acid (MSA as shown below). Then 25 ml of freshly prepared 0.2 M NaBH<sub>4</sub> aqueous solution was added at the rate of 5 ml/min under vigorous stirring. The as-formed gold clusters with average diameter of ~3.5 nm were washed by methanol/water mixture solvents repeatedly through centrifugation/sonication processes. The pellet was vacuum dried to the black powder, which was readily dissolved in 0.005% weight percent tetraethylammonium hydroxide (TEAOH as shown below right) aqueous solution.



The previous study shows that the nanorods formation is not induced by the specific hydrogen bonding between MUA and C<sub>20</sub>A's -COOH groups.

However, the particle/fluid interface is important for SMN because of the contact angle effect. As NPs solubility is mainly determined by the surface functional group, the methyl terminated particles need to be dissolved in chloroform to facilitate the nanohybrids formation. Hence in this dissertation, both MUA-GNPs<sup>18</sup> and oleylamine (OA,  $\text{CH}_3(\text{CH}_2)_7\text{CH}=\text{CH}(\text{CH}_2)_7\text{CH}_2\text{NH}_2$ ) capped GNPs (OA-GNPs)<sup>19</sup> have been successfully produced. In a typical reaction to make MUA-GNPs, adding 25 ml of freshly made 0.2 M  $\text{NaBH}_4$  aqueous solution to a 2:1 molar ratio of  $\text{HAuCl}_4$  and MUA's methanol solution and stirring for at least 2 hours at room temperature will generate ~4 nm average size of MUA-GNPs, where MUA plays as the stabilizer on gold cores to prevent GNPs from growing while  $\text{NaBH}_4$  plays as the reducing agent to reduce  $\text{HAuCl}_4$  to atoms. Making OA-GNPs is adopted by a one phase synthesis method varied from Brust method, which takes place in 50 ml toluene by refluxing 0.15 mmol  $\text{HAuCl}_4$  and 10 mmol OA mixed solution for 2 h, yielding a 15 nm average size of OA-GNPs, where OA is both a stabilizer and a reducing agent.

### **2.2.3. Immobilization and array formation**

GNPs have been immobilized onto different substrates, such as micas, graphites, and Si wafers either by physisorption or chemisorption. Three examples from literature are highlighted below. The immobilization is not limited to GNPs. The general methods for different kinds of NPs are listed in Table 2.1.

**Table 2.1. Immobilization methods for different kinds of NPs on different kinds of substrates depending on outmost group.**

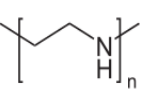
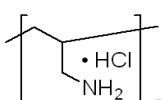
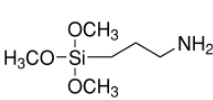
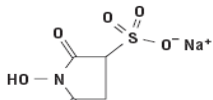
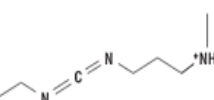
|           |   |                                |  |                                       |
|-----------|---|--------------------------------|--|---------------------------------------|
| NP        | Negative<br>(e.g. citrate ion)              | Negative<br>(e.g. citrate ion) | -COOH (-COO <sup>-</sup> )<br>(deprotonated)                         | -COOH<br>(neutral)                    |
| Substrate | Divalent cation<br>(e.g. Mn <sup>2+</sup> ) | Positive polymer<br>(e.g. PEI) | -NH <sub>2</sub> (-NH <sub>3</sub> <sup>+</sup> )<br>(electrostatic) | -NH <sub>2</sub> (EDC<br>crosslinker) |

One example of immobilizing GNPs by electrostatic force was discussed by Schmitt and co-workers.<sup>20</sup> They were able to prepare citrate-GNP monolayers on polycation modified mica surfaces. The polycations include polyethyleneimine (PEI) or poly(allylamine) hydrochloride (PAH). In this case, negative citrate ions were attracted onto positively charged amino groups from the polymer layer. They also characterized the optical properties of the GNPs quasi-monolayer and indicated the potential applications of the prototypes.

Another immobilization example by electrostatic force is the work done by Park and co-workers.<sup>21</sup> They first fabricated (3-Aminopropyl) trimethoxysilane (APTMS) monolayers on the oxidized Si wafer with -NH<sub>2</sub> as the outmost group. Then they immobilized MUA-CdSe/ZnS core-shell NPs on the substrates by electrostatic forces in acidic conditions, where -NH<sub>2</sub> is protonated to -NH<sub>3</sub><sup>+</sup> and -COOH is deprotonated to -COO<sup>-</sup>. They also showed that by changing the concentration, deposition time, and solution pH, the NPs coverage on the substrates could be controlled.

The immobilization will be more stable if chemical bonding is introduced to replace the electrostatic force. One example is anchoring phage particles (~50 nm in diameter) onto APTMS monolayer on glass substrates by the Mao group.<sup>22</sup> Through EDC crosslinker,  $-\text{COOH}$  group from phage would form amide bonds with  $-\text{NH}_2$  from APTMS. Although this is not an example of metal NPs, it indicates that  $\text{COOH}$ -functionalized particles could also be immobilized by NHS-EDC chemistry on  $\text{NH}_2$ -functionalized substrate. Sulfo-NHS and EDC stand for N-Hydroxy sulfosuccinimide and 1-Ethyl-3-(3-dimethylaminopropyl) carbodiimide hydrochloride crosslinker, respectively.

**Table 2.2. The molecular structures mentioned in this section.**

| PEI   | PAH   | APTMS   | Sulfo-NHS  | EDC   |
|---|---|---|--|---|
|  |  |  |  |  |

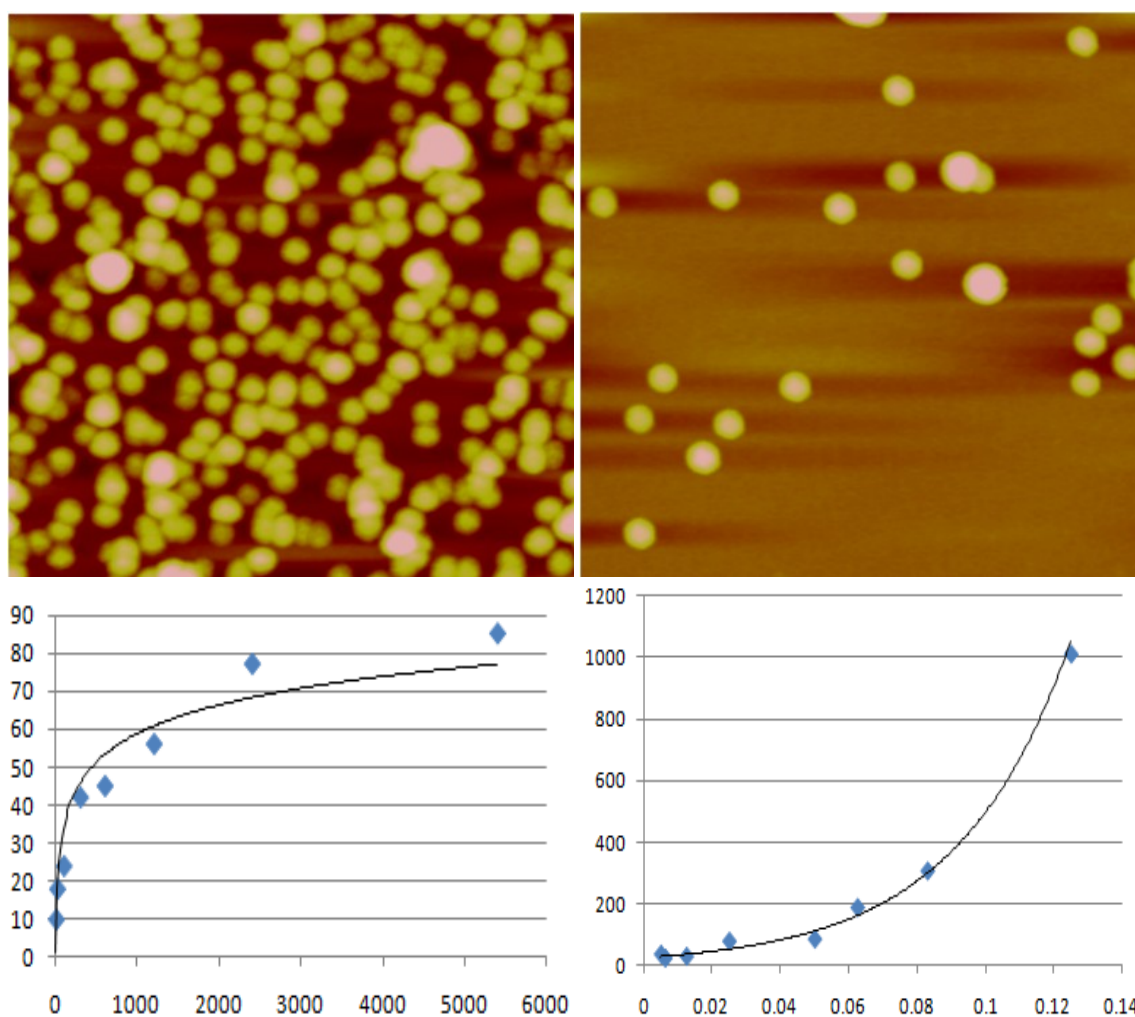
We are able to dip coat the desirable GNP solutions onto the substrates through electrostatic forces, such as PEI treated mica or APTMS (amine group is usually positively charged and promoted by EDC crosslinker) monolayers on the oxidized Si wafers, which are obtained by immersing hand cleaved  $1 \text{ cm}^2$  double-sided polished Si (111) doped with boron into Piranha solution (1:3 ratio of 30%  $\text{H}_2\text{O}_2$  to concentrated  $\text{H}_2\text{SO}_4$ ) for at least one hour.

As for the system of mica surface, negatively charged MUA-GNPs (outmost functional group  $-\text{COOH}$  is deprotonated in water due to MUA's weak acidity) could be immobilized on negative mica by a positive medium. One

method is by using metal cations such as  $\text{Mn}^{2+}$ .<sup>23</sup> One drop of highly diluted ( $10^{-4}$  M)  $\text{MnCl}_2$  aqueous solution is dipped onto the newly cleaved mica surface for 5 minutes to provide scattered positively charged locations for GNPs to launch. The other method is by using the positively charged polymers such as PEI to self-assemble a monolayer on mica, and then immobilize MUA-GNPs onto the substrates.

In Figure 2.1 we are showing the AFM height images for  $\sim 10$  nm citrate-GNPs (also negatively charged as extensive citrate anions on Gold core surface) decorated PEI/mica substrates. By changing the concentration of the GNPs aqueous solution (from 0.1 to 0.01 g/L) and keeping the standing time of gold colloidal the same (90 min), we are able to control the coverage. In bottom 2 plots, the NPs surface coverage on PEI/mica shows some relationship with deposition time and concentration. With these two plots we could find the specific condition to fabricate desired NPs covered substrates. This will facilitate the separation of the NPs with variable distances, enabling us to investigate the so-called nanoconfinement, the nearest NP's influence onto the nanorods formation from one NP and. When NPs are separated very far from each other (about hundreds of nanometers), we are assuming the crystallization process is related to only one NP without other NPs' perturbation.

**Figure 2.1. AFM height images of 0.1 (Top left) and 0.01 (Top right) g/L ~10 nm citrate-GNPs immobilized on PEI monolayer/mica substrates by dip coating method, standing time = 90 min. (z-range = 20 nm and image area is  $2 \times 2 \mu\text{m}^2$ ) Bottom two plots show the relationships between the NPs surface coverage (y-axis, NPs number per  $5\mu\text{m} \times 5\mu\text{m}$ ) and (Left) deposition time (s) for a fixed concentration of 0.01 g/L; (Right) NPs concentration (g/L) for a fixed deposition time of 90 min.**



Above results show that we are able to change the coverage of the NPs on the substrates, enabling us to investigate the deposition time and concentration's effects on the GNPs' immobilization process, similar to the work of CdSe/ZnS NPs discussed before.<sup>21</sup> From the underlying relationship, optimized conditions for the process will reveal and be applied to obtain a series of randomly immobilized MUA-GNPs with different coverage. By assuming the average distance of the nearest two GNPs has a linear relationship with the GNPs' coverage area percentage, the nanoconfinement of the GNPs' separation distances on the fatty acids' nucleation could be studied.

### **2.3. Crystallization nanoconfinement on nanopatterns by particle**

#### **lithography**

##### **2.3.1. Organosilane nanopatterns**

Nanopatterns have been made by PS template gold salt annealing,<sup>24</sup> dip-pen nanolithography,<sup>25</sup> particle lithography,<sup>26</sup> and the most conventional method of the electron beam (e-beam) lithography,<sup>27</sup> which involves programming a SEM's e-beam to write specific patterns on the electron sensitive polymer such as poly(methyl methacrylate). However e-beam lithography is limited in spatial resolution to ~50 nm in practice and its usage is quite expensive. The limitations can be overcome by molecular self-assembly methods.

One example is to use the Atomic Force Microscope (AFM) silicon nitride ( $\text{Si}_3\text{N}_4$ ) pyramid probe with a diameter smaller than 50 nm. Sung and co-workers<sup>25</sup> used a so-called dip-pen nanolithography method to make Gold



nanopatterns on the oxidized Si substrate. By using AFM tip as the pen and  $\text{HAuCl}_4$  solution as the ink, they were able to write varied patterns onto the substrate. After annealing,  $\text{HAuCl}_4$  was decomposed to reveal pure Gold patterns. Programming the AFM tip's writing mechanics would facilitate the desired nanopatterns formation.

Another example is to use uniform nanosize PS spheres ranges from 100 to 900 nm as the template on the oxidized Si wafer developed by Garno and co-workers.<sup>26</sup> By controlling the water menisci dimensions trapped by individual PS sphere, octadecyltrichlorosilane (OTS) vapor deposition, which is essential to replace the water on the surface, could be controlled into some nanopatterns such as nanoholes and nanorings. This so-called particle lithography method, though limited to hexagonal pattern, is easier and cheaper than the e-beam lithography.

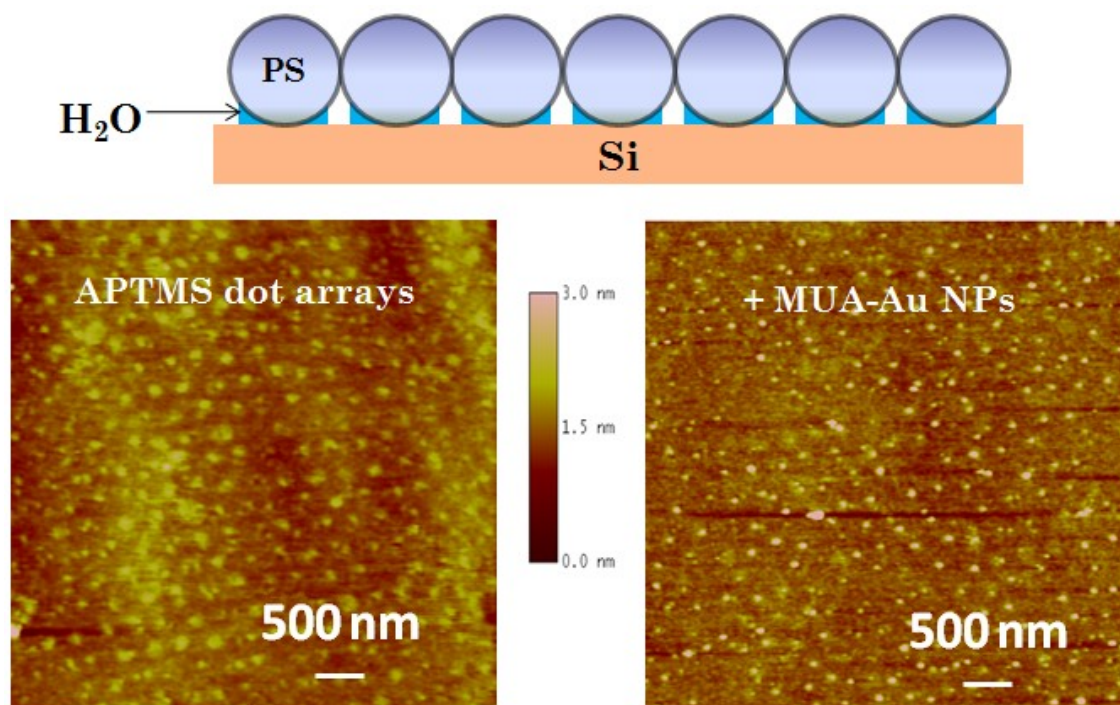
Close-packed monodisperse PS nanospheres are used as an evaporative mask to generate ordered rings or pore-shaped OTS structures via CVD. OTS vapor reacts with water to replace the trace amount of menisci trapped by PS spheres. After at least 6 hours reaction PS spheres are removed away by rinsing and sonication with water and ethanol to reveal the organosilane's nanopatterns. This is a general method which only requires a Si-O-Si bond at the substrate's surface while OTS's outmost group  $-\text{CH}_3$  is quite rigid; therefore, other organosilanes are proposed to be used here for the functionalization. By varying the drying duration and relative humidity, the menisci's dimensions could be controlled, resulting in different nano features such as well-ordered rings or pore-

shaped structures on different substrates (require extensive –OH groups on the surfaces).

There are two ways for the GNPs to decorate on the organosilane's nanopatterns. One is described as followed: firstly OTS holes are fabricated to passivate the surface; then the holes are filled in by specific organosilanes which have strong affinities with GNPs. As for citrate-GNPs, we could refill 3-mercaptopropyl trimethoxysilane (MPTMS) into the nanoholes containing unreacted hydroxyl groups. Sulfur sites for GNPs to form covalent bonds are provided in the ordered nanoholes. By this means, GNPs arrays are obtained, and depending on the PS sphere (determines the size of the hole) and a single GNP size, multiple GNPs might form clusters in individual nanoholes.

The other method is by controlling the menisci down to extremely small sizes, so that the organosilane arrays will be revealed as patterned dots, followed by decoration of GNPs if the organosilane has –NH<sub>2</sub> or –SH functional group at the outmost layer. Figure 2.2 shows our preliminary investigation of APTMS patterns. By using a vacuum on a desiccator with the substrate (right after visible water evaporation with 300 nm PS spheres ordering) and 300 μL APTMS inside, the nanodot arrays are revealed after the organosilane's condensation onto the water menisci trapped PS and the removal of the PS spheres mask by sonication in ethanol and DI water. Further ~4 nm MUA-GNPs' decoration was promoted by EDC chemistry to bond MUA's –COOH and APTMS's –NH<sub>2</sub>.

**Figure 2.2. AFM height images of APTMS nanodots (left) generated by the 300 nm PS lithography, and then functionalized with MUA-GNPs. (right)**



By varying the latex particle size, the separation distance of the ordered nanostructures will be precisely controlled, as well as the GNP arrays. These arrays are suitable templates for studying particle-induced functional molecular rods. The nanoconfinement effect will be addressed using varied GNP sizes and varied separation distances. Monodisperse PS spheres with a series of different sizes are available in ThermoFisher Scientific. Diameter is from as low as decades of nanometers to micrometer level. We use 300 and 900 nm PS spheres to create two types of nanopatterns for nanoconfinement studies.

### **2.3.2. Pattern controlled crystallization**

One example is growing crystals in well-defined pores close to the critical nucleus size. This displays unique characteristics of nucleation due to the confinement effect of the pores imposed on the nuclei. Ward and co-workers<sup>28</sup> presented a new approach to controlling the polymorphism of organic materials in nanometer-scale channels of controlled pore glass (CPG) and porous poly(cyclohexylethylene) (p-PCHE) based diblock copolymers. The resulted nanocrystals exhibited size-dependent polymorphism and thermotropic behavior since the physical confinement imposed by the pores dimensions. By changing the pore size, the percentage of nanocrystals with different polymorphisms could be controlled. By decreasing the channel diameter, which is equivalent to increasing the surface-area-to-volume ratio, the nanocrystals' melting point would be lowered.

Another example is reported by Aizenberg and co-workers,<sup>29</sup> which depicts control of calcite ( $\text{CaCO}_3$ ) crystal nucleation by patterned self-assembled monolayers (SAMS). In that work, they patterned SAMS on the metal substrates by microcontact printing with an elastomeric stamp, poly(dimethylsiloxane) (PDMS). They showed that calcite crystals have different growth patterns on different molecule monolayers as well as metal substrates (Au, Ag, and Pd), which is because the outmost functional group (-COOH and -OH) has different affinity with calcite molecule. For instance, different crystal shapes are found on different combinations of metal and SAMS layers, which reveals the underlying nucleating plane for calcite. While on the  $-\text{CH}_3$  area outside the nanopatterns, crystallization is prohibited.

## CHAPTER 3

### EXPERIMENTAL

#### 3.1. Atomic force microscope

AFM generates detailed topography of material surfaces with nanoscale resolution as well as contrast between different chemical compositions. The lateral resolution is 2 to 10 nm and the vertical resolution could be as accurate as 0.1 nm, which is comparable to TEM. As opposed to electron or optical microscopes, AFM does not use magnetic or glass lenses for producing the sample's image; it uses a sharp tip (probe with cantilever) instead. The other major advantages of AFM over TEM are ease in sample preparation, temperature control and liquid imaging close to physiologic conditions, which facilitates in situ studies.

An AFM tip contains a nano-fabricated Si or Si<sub>3</sub>N<sub>4</sub> probe (pyramidal shape) and a flexible cantilever which has a specific spring constant. A laser beam is focused on the cantilever and reflected from the rear of it, so that the deflection of the cantilever is detected by the photodiode. Due to the surface topography, when tip scans over the sample, the cantilever deflects the topographic image of surface. The underlying theory is: the electrical differential signal obtained from each point was generated by computers and processed to the feedback signal for the piezo scanner to maintain a constant force on the probe. AFM could also generate amplitude (first derivative of height) and phase images other than the height image.

AFM can be operated in three different modes, including contact, non-contact, and tapping mode. Contact and tapping modes are used more popularly in current researches. Tapping mode, most commonly used nowadays, is a technique that maps topography by tapping the surface lightly with an oscillating probe. While in contact mode, the probe is in permanent physical contact with the sample during the scanning. Contact mode is heavily influenced by the adhesive and frictional forces, which may easily distort the data and damage the sample. Non-contact mode can be hampered by the contaminant layer to interfere with oscillation and generally provides low resolution; therefore it is less popular.

Overall, tapping mode could eliminate frictional forces as the probe intermittently contacts the sample and oscillates with sufficient amplitude to prevent itself from being trapped by adhesive forces from meniscus or other contaminants. In this dissertation, tapping mode is used for all imaging unless stated otherwise. Dimension 3100 and MultiMode Nanoscope IIIA from VEECO are the most important characterization techniques involved in this research. The analysis is conducted by Nanoscope software 5.12 from VEECO.

### **3.2. TEM (EDS), FE-SEM**

Besides AFM, TEM is another technique used in this study for characterizing NPs since it combines EDS, which could determine the chemical composition of the NP cores along with their monolayers. Nowadays TEM has been widely applied in nanomaterials, especially inorganic nanocrystal characterizations. TEM resolution strongly depends on the acceleration voltage

of the electron beam. Under ideal environments, high resolution TEM (HR-TEM) could reach angstrom level resolutions. Therefore TEM is able to get the atomic arrangement inside a crystal and provide lattice planes periodicity information, in addition to the particles' morphology. EDS is used to determine the X-ray radiation's energy spectrum. When the electron beam attacks the sample, electrons are ejected from the sample's surface atoms, which results in an electron vacancy to be filled by an electron from a higher shell. In order to balance the energy difference during this process, an X-ray will be emitted. EDS measures the number of emitted X-rays versus their energies respectively, which are dictated by the elemental composition. Thus, the composition of samples can be obtained by EDS.

In this dissertation, the TEM analysis is conducted by a JEOL FasTEM 2010 HR TEM, which is operated in the bright field mode at an accelerating voltage of 200 keV, and the synthesized GNPs are deposited on the carbon-coated copper grid. Both size and shape of the GNP cores are obtained from this characterization (Note that only crystallized GNP cores but not the amorphous organic monolayers are visible under TEM high voltage electron beam). The chemical compositions of inorganic NPs are gained from the in situ EDS combined with TEM. The estimation of the ratio of capping layer to NP and the area per capping molecule on the NPs could be calculated from the measurement.

Another electron microscope that was conducted for this research is also available in CIF at Wayne State Chemistry. Thermal FE-SEM (JEOL JSM-7600F)

scans with a high-energy of about 1-50 keV beam of electrons onto the conductive sample surfaces to produce high-resolution of 1-10 nm images. The electrons interact with the atoms in the sample and produce signals that contain information about the sample's surface topography, composition and so on. The conventional SEM specimen must be electrically conductive to prevent the accumulation of electrostatic charge at the surface. For nonconductive specimen, an ultrathin coating of electrically conductive material (commonly gold or carbon, ~10 nm) needs to be deposited on the sample by low vacuum sputter (EffaCoater) coatings or high vacuum evaporations for better image resolution. The FE-SEM images are obtained at a working distance of 8 nm and voltage of 15 kV.

### **3.3. UV-Vis, FT-IR**

UV-Vis spectroscopy (Varian Cary 50) is also used to measure the sizes of inorganic NP cores. The quantum size effect is involved when the de Broglie wavelength of the valence electrons is of the same order as the size of the particle itself. Freely mobile electrons are trapped in such metal "boxes" and show a characteristic collective oscillation frequency of the plasma resonance, giving rise to the so-called surface plasmon resonance (SPR) band observed near 530 nm in the 5-20-nm-diameter range. There is an approximate relationship between the SPR peak position and citrate-GNPs size from both the experimental data of citrate-GNPs and model calculations.<sup>30</sup> Then the estimated average size of the GNPs could be gained from the SPR peak position. The well-known Beer's Law could also help us to identify the colloidal concentration. The



SPR is also related with the gold colloidal's color. Usually the smallest gold colloids (<5 nm) are yellow-orange, the midrange (5-30 nm) are wine-red, while larger particles (>30 nm) are purplish blue-green.

FT-IR (Perkin Elmer Spectrum 400) is used to characterize the chemical bonds for the organic monolayers on GNPs as well as the crystalline structures of aspirin NPs. The mechanism of IR can be explained by detecting chemical bonds' specific vibrational frequencies corresponding to energy levels in IR regions. It must be related to changes in the permanent dipole of a molecule in order for a vibrational mode to be infrared active. The vibrations' frequency can be associated with a particular bond type to confirm the chemical composition inside a molecule. In this work, FT-IR measurements are conducted on NP powder or dispersion in organic solvents on FT-IR quartz window, which is prepared by dropping droplets of freshly dispersed NP solutions. The FT-IR spectra of the samples are recorded in ambient air at room temperature with a Perkin Elmer Spectrum 400 FT-IR spectrometer equipped with a single reflection diamond Attenuated Total Internal Reflection (ATR) prism, which could enhance the reflected signal.

#### **3.4. PXRD, TGA, and contact angle**

X-ray techniques including PXRD, X-ray reflectivity and small angle X-ray scattering could be carried out in Mao's lab with the Rigaku SmartLab X-ray diffractometer to determine the inorganic NPs core composition, as well as investigate the crystallographic structure and physical properties of materials and

thin films without long range order. When crystallites are less than approximately 1,000 Å in size, appreciable broadening in the PXRD lines will occur. These regions may in fact correspond to the actual size of the particles. By using the well-known Scherrer Equation  $\tau = K\lambda / \beta\cos\theta$ , (where  $K = 0.9$  is the shape factor,  $\lambda = 1.54 \text{ \AA}$  is the wavelength of Cu  $K_{\alpha}$  line,  $\beta$  is the FWHM, full-width at half maximum of the PXRD pattern peak and  $\theta$  is the Bragg angle), one could estimate the intrinsic domain size,  $\tau$  of the nanocrystals.

TGA (Thermal fisher scientific) is a type of testing that is performed on samples to determine changes in weight in relation to change in temperature. Such analysis relies on a high degree of precision in measurements of weight and temperature change. TGA is commonly employed in research and testing the characteristics of materials such as polymers, to determine degradation temperatures and the percentages of inorganic and organic components in materials. In this dissertation, TGA is used to burn out the organic layers on GNPs, for calculating the organic molecule coverage on the cores since organic species could be transferred into gas phase at lower temperature as opposed to the rigid inorganic NPs. The TGA result could be the complementary for the EDS analysis.

The surface hydrophobicity is measured with an NRL contact angle goniometer (Model 100, Rame-Hart) in a laboratory atmosphere. A 10  $\mu\text{L}$  water droplet is placed on the substrate and the static contact angles are measured on both sides of the droplet. Three droplets are placed at various spots on the substrate and the average readings are reported. The typical error is  $\pm 3^{\circ}$ .

### 3.5. DLS, ICP-MS

Dynamic light scattering (DLS) and zeta potential of the GNPs are measured using a Malvern Nano-ZS. DLS samples are prepared by diluting the GNP after its purification into 50  $\mu\text{g}/\text{mL}$  aqueous solution. 1250  $\mu\text{L}$  of the solution is transferred to a 5.0 mL PS cuvette. The Z-average hydrodynamic diameter (HD), polydispersity index (PDI), and zeta potential are measured in pH=7 citrate buffer and temperature of 25°C. The refractive index of the particles was set to 1.5. Each final measurement is ten 2 min measurements averaged together.

ICP-MS (Perkin Elmer NexION 300D) is used to determine gold uptake by cells. Samples (cell pellet at centrifuge tube bottom) are digested in 500  $\mu\text{L}$  of nitric acid and 1500  $\mu\text{L}$  hydrochloric acid for 60 min in 90°C water bath, then diluted into deionized water to make 15 mL solution.

### 3.6. Conclusions

Table 3.1 concludes above characterization methods for 2 main aspects of the GNPs: size and surface layer. In this dissertation, all of the methods are carried out not only for characterizing GNPs but also the surface features of nanopatterns, as well as nanocrystals confined on oxidized Si wafers. FESEM and contact angle were used to characterize nanopatterns while DLS and ICP-MS were used to characterize for GNP's incubation with macrophages.

**Table 3.1. Characterization methods for GNPs' 2 main aspects.**

|               |   |
|---------------|---|
| Size          | AFM: GNPs overall size including organic layer<br>TEM: GNPs core size without organic layer<br>UV-Vis: SPR peak position to estimate size<br>PXRD: Intrinsic crystal domain size from Scherrer Equation |
| Surface layer | FT-IR: Different functional groups correspond vibrational peaks<br>TGA: Organic layer weight percent to calculate surface coverage<br>EDS: Chemical composition (which atom) in organic layer           |

## CHAPTER 4

### FORMATION OF CARBOXYLIC ACID NANORODS ON OA-GNPs

#### 4.1. Introduction

Spatial control and connection of nano-components with distinct interfaces continue to be a major challenge in nanodevice manufacture. Template synthesis of one component in the matrix of another component is an attractive strategy for the creation of hybrid nanomaterials and nanodevices, though methods to connect individual components, such as NPs and nanorods remain few (an example being the biotinylated DNA connection to streptavidin-capped NPs via molecular recognition<sup>31</sup>). Furthermore, most studies focus on inorganic materials, but self-assembly based on small organic molecules or their hybrids with inorganic NPs could also yield useful properties.<sup>32-36</sup> Electron transfer between metal NPs can be manipulated by organic interconnects in single-electron transistor (SET) devices.<sup>37</sup> Ultrasensitive electrochemical sensors based on cyclic voltammetry (CV), ion-sensitive field-effect transistor (ISFET), or enzymatic reactions were constructed using GNP superstructures with improved sensor stability, sensitivity, and selectivity.<sup>38,39</sup> NP electrode materials enhanced electron transfer between redox agents and bulk electrodes and allowed fine tuning of sensitivity via particle size, morphology, and number.<sup>40</sup> Selectivity was improved by specific interactions between the analytes and NP capping ligands.<sup>38,41-43</sup> Other examples of inorganic/organic hybrid devices include GNPs-decorated  $\pi$  – conjugated nano-tapes with enhanced electrical conductivity,<sup>44</sup> GNPs-decorated

carbon nanotube (CNT) catalysts with higher catalytic activities toward oxygen reduction,<sup>3</sup> and enzyme-coated CNTs placed between Gold electrodes showing higher enzymatic detection sensitivity.<sup>45</sup>

Our previous work showed the unique capability of certain NPs to nucleate nanocrystals of extremely small cross-sectional area (nanorods) of n-carboxylic acids. The presence of MUA capped cadmium selenide (MUA-CdSe) NPs was found to alter the self-assembly pattern of eicosanoic acid on highly oriented pyrolytic graphite (HOPG) from a 2-D epitaxial film to 1-D nanorods attached to the NPs.<sup>4</sup> A comprehensive study of a homologous carboxylic acid series found that several of them also form nanorods readily on NPs of different core materials (CdSe, CdS, and Gold).<sup>46</sup> The core chemical composition is therefore immaterial to the nanorod formation. The chemical composition of the capping monolayer, however, plays an important role in the nanorod formation. The role of the capping layer is to provide sufficient colloidal stability for the NPs to be effective nucleation seeds. However, it is unclear from the previous studies whether specific interactions such as polar-polar and hydrogen-bonding interactions between the capping layer and the nucleus are necessary for the nanorod formation. In addition, photo-catalytic properties of CdSe pose a practical problem for the crystallization experiments because of the tendency of MUA-CdSe NPs to aggregate over time.

In order to address the above issues, we employed a methyl-terminated NP whose interaction with the crystallizing unit is limited to the dispersive interaction. OA-GNPs were synthesized and characterized by TEM, EDS, AFM,

PXRD, FT-IR, and TGA. OA-GNPs are not subject to photo-induced aggregation making it easier for the crystallization experiments. In order to compare with previous results of carboxyl-terminated NPs, we used the same homologous series of carboxylic acids as crystallizing compounds and HOPG as substrate. The results show that nanorods of carboxylic acids are nucleated by OA-GNPs with a large fraction been detached from the NPs. The AFM results demonstrate that dispersive interactions alone can support the seed-mediated mechanism of nanorod formation. However, specific interactions may be necessary to maintain an intact NP/nanorod interface.

## 4.2. Experimental

**Materials.** OA (technical grade, Aldrich), hydrogen tetrachloroaurate (III) hydrate (99.9%, Strem Chemicals), and toluene (ACS grade, EMD Chemicals) were used as received. Carboxylic acids including hexadecanoic acid ( $C_{16}A$ , Fluka,  $\geq 99.5\%$ ), eicosanoic acid ( $C_{20}A$ , Sigma,  $\geq 99\%$ ), docosanoic acid ( $C_{22}A$ , Aldrich, 99%), hexacosanoic acid ( $C_{26}A$ , Sigma,  $\geq 95\%$ ), and triacontanoic acid ( $C_{30}A$ , Sigma,  $\geq 95\%$ ) were used as received. Crystallization of the carboxylic acids was conducted in chloroform (Fisher Scientific, 100%). HOPG (Mikromasch, ZYB grade) was hand cleaved just before use with an adhesive tape until a smooth surface was obtained.

**NP synthesis.** OA-GNPs with diameter less than 20 nm were synthesized according to the literature.<sup>19</sup> In one typical reaction, 49 mg (0.15 mmol) of  $HAuCl_4$  was quickly added to a boiling solution of 10 ml (22 mmol) of OA in 50 ml of

toluene. After 15–30 min, the color of the solution changed gradually from bright yellow to grey yellow and finally to deep red. After 2 h heating with reflux, the reaction mixture was allowed to cool to room temperature and 100 mL of methanol was added to precipitate the product. The OA-GNPs were isolated by centrifugation and washed three times with methanol. Vacuum drying of the precipitant yielded a black solid. The product dissolves readily in non-polar solvents such as chloroform.

**Film preparation.** 0.1 mL of freshly made chloroform solution of the carboxylic acid (0.1–0.4 mM) was placed on HOPG during spin coating. In each case, the carboxylic acid concentration was adjusted depending on its solubility and solvent evaporation rate by trial and error in order to achieve near monolayer coverage. The spin rate was 3,000 rpm and the spin time was 60 s. To study the effect of the NP, 0.1 mL of mixed chloroform solution containing the carboxylic acid (0.1–0.4 mM) and OA-GNPs (0.1 mM) was used for spin coating. The spin coated films maintained their nanostructures for at least 1 month at room temperature.

**Characterization.** TEM (JEOL JEM-2010) and PXRD (Rigaku SmartLab) were used to determine the size distribution of the GNP core. TEM was conducted in the bright field mode operating at an accelerating voltage of 200 keV. The particle size was averaged over 100 individual particles measured manually by the ImageJ software. In situ EDS attached to the TEM was used to determine the chemical composition of the OA-GNPs. In addition, the NPs were



analyzed by FT-IR (Perkin Elmer Spectrum 400) and TGA (Thermo Fisher Scientific).

The thin films deposited on HOPG were characterized by AFM (VEECO Dimension 3100G scanner). Height, amplitude, and phase images were obtained in the tapping mode in ambient air. Uncoated silicon probes (TESP, VEECO) with a factory-specified spring constant of 40 N/m, length of 125  $\mu\text{m}$ , width of 40  $\mu\text{m}$ , and nominal probe radius of curvature less than 10 nm were used. The scan rate used was in the range of 0.5–2 Hz depending on the scan size. Integral and proportional gains were approximately 0.4 and 0.8, respectively. AFM height images are reported unless specified. Height images have been plane-fit in the fast scan direction with no additional filtering operation. Images are analyzed using the Nanoscope software from Digital Instruments (Version 5.12). The sectional height analysis was used to measure the vertical and lateral dimensions of the deposited NPs. The lateral width was measured at the half maximum peak height of the NP to minimize tip convolution.

### **4.3. Results and discussion**

#### **4.3.1. NP characterization**

In SMN, the seed size and interfacial properties are important control parameters. The nucleation capability factor of a seed particle,  $f = \Delta G_c^{\text{het}} / \Delta G_c$ , is a function of the contact angle between the cap-shaped nucleus and the seed surface,  $\theta$ , and seed size, which can be defined as  $R' = R^S / r_c$ .  $R^S$  is the radius of curvature of the seed particle and  $r_c$  is the critical nucleus radius. When the seed

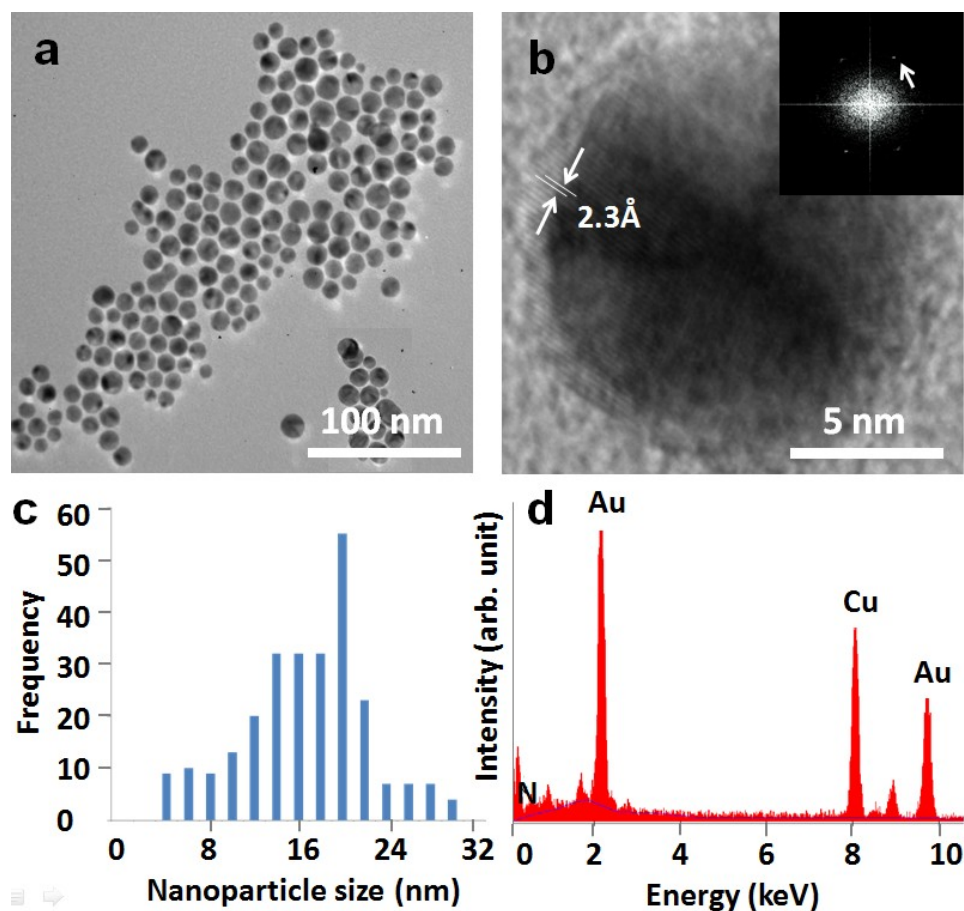
is large, e.g.,  $R' \geq 10$ , the particle surface curvature approaches that of a flat surface, and the energy barrier is dominated by  $\theta$ . When the seed is small, e.g.,  $R' \leq 0.1$ ,  $f$  is close to 1, and the foreign particle is ineffective in nucleation. When  $0.1 \leq R' \leq 10$ ,  $f$  decreases drastically with decreasing  $r_c$  (or increasing  $\Delta\mu$ ). It suggests that small  $r_c$  or the presence of a good structural match compensating for small seed size can render NPs effective nucleation seeds.

Our previous results indicate that well dispersed NPs with high colloidal stability are more likely to nucleate carboxylic acid nanorods. The data point to a seed particle size range that favors nanorod formation, and within this range, the average number of nanorods per NP is proportional to the particle surface area. Most of the previous work was conducted using NPs with carboxyl termination, such as MUA-CdSe and MUA-CdS. However there was insufficient evidence to show whether carboxylic acid nanorod formation requires carboxyl-terminated NP seeds, that is, specific interactions between the seed and the crystallizing agent. Here, we focus on methyl-terminated NPs in the form of OA-GNPs, and we characterize the NPs by TEM, EDS, AFM, PXRD, FT-IR, and TGA.

Figure 4.1a is a TEM image of the OA-GNPs dispersed on the TEM copper grid. The NIH ImageJ software was used to analyze the sphericity of the particles ( $N \approx 100$ ) by measuring the area ( $A$ ) and perimeter ( $P$ ) of each particle. The average circularity of the OA-GNPs,  $F$  ( $F = 1$  for a perfect circle), was calculated to be  $F = 4\pi A/P^2 = 0.98$ . In the following discussion a spherical shape of the NP is assumed. Figure 4.1b shows a single NP with 2.3 Å fringes consistent with the interplanar spacing of face-centered cubic (FCC) Gold [111]

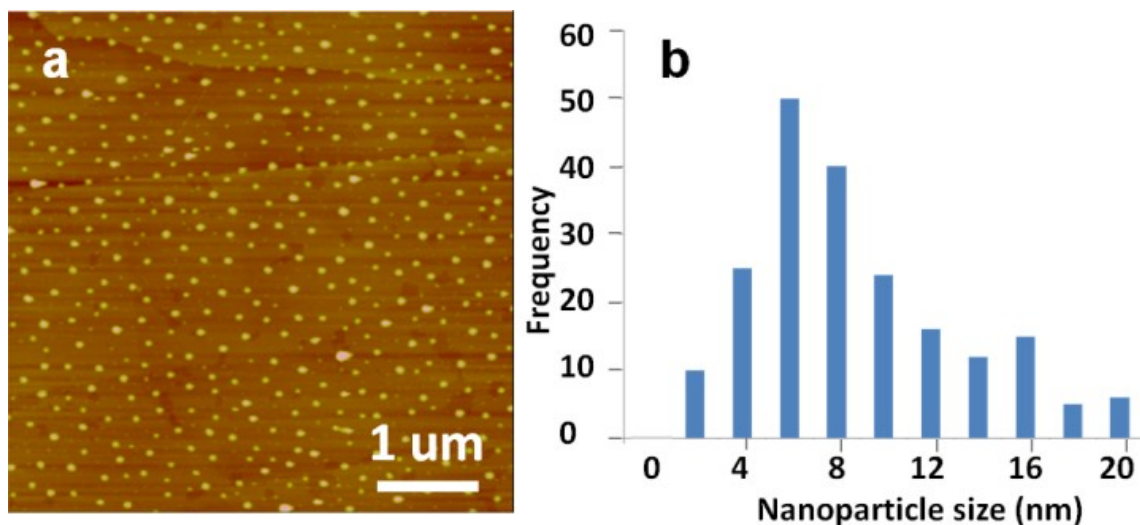
planes. The arrow points to the reciprocal spacing in the 2D-FFT analysis (inset). Figure 4.1c shows the size histogram of the NPs obtained from TEM images with a particle diameter range of 3–30 nm and an average diameter of  $15.7 \pm 5.6$  nm. 80% of the particles are smaller than 20 nm. The atomic ratio of Au to N was determined to be  $\sim 0.25$  from the EDS spectrum (Figure 4.1d). The Cu signal is from the TEM sample grid.

**Figure 4.1. TEM images of OA-GNPs at (a) low magnification ( $300 \times 300$  nm<sup>2</sup>) and (b) high magnification ( $15 \times 15$  nm<sup>2</sup>) with a 2-D FFT image as the inset. (c) Histogram of OA-GNP diameters based on TEM. (d) EDS spectrum of OA-GNP chemical composition.**



The size distribution of OA-GNPs was also measured using AFM. Figure 4.2a is a typical AFM image of OA-GNPs on HOPG. The AFM samples were prepared by spin coating of 0.1 mL 0.1 mM OA-GNPs chloroform solution on HOPG. Chloroform quickly evaporates leaving a uniform particle layer on HOPG. The AFM images show well dispersed particles with no significant aggregation (a significant improvement over MUA-CdSe NPs), an indication of a close-packed OA monolayer on GNPs. Figure 4.2b shows the particle diameter histogram measured in the z (height) direction using AFM height images. The particle size ranges from 2 to 20 nm with an average height of  $8.2 \pm 4.1$  nm. The average OA-GNP size by AFM is less than that measured by TEM, especially considering that AFM values include the organic capping layer. It is possible that spin coating selectively deposits smaller particles.

**Figure 4.2. (a) AFM image (z-range = 20 nm) of OA-GNPs on HOPG substrate. (b) Size histogram of OA-GNPs measured by AFM sectional height analysis.**



OA-GNPs were examined by PXRD as shown in Figure 4.3. The X-ray peaks at  $2\theta = 38.2^\circ$ ,  $44.5^\circ$ ,  $64.6^\circ$ , and  $77.5^\circ$  correspond to [111], [200], [220], and [311] crystalline planes with the interplanar d-spacing of 2.35 Å, 2.03 Å, 1.44 Å, and 1.23 Å, respectively. The intrinsic crystalline domain size,  $\tau$ , was estimated using the Scherrer equation,  $\tau = K\lambda / \beta\cos\theta$ , where  $K$  is the shape factor equaling 0.9 for single crystal with a spherical shape,  $\lambda$  is Cu  $K_\alpha$  wavelength, and  $\beta$  is the full width at half maximum peak height. The estimated diameters of OA-GNPs using 4 individual peaks are 18.7, 12.5, 14.1 and 13.0 nm, respectively, and the average is 14.6 nm.

Figure 4.3. PXRD pattern of OA-GNPs.

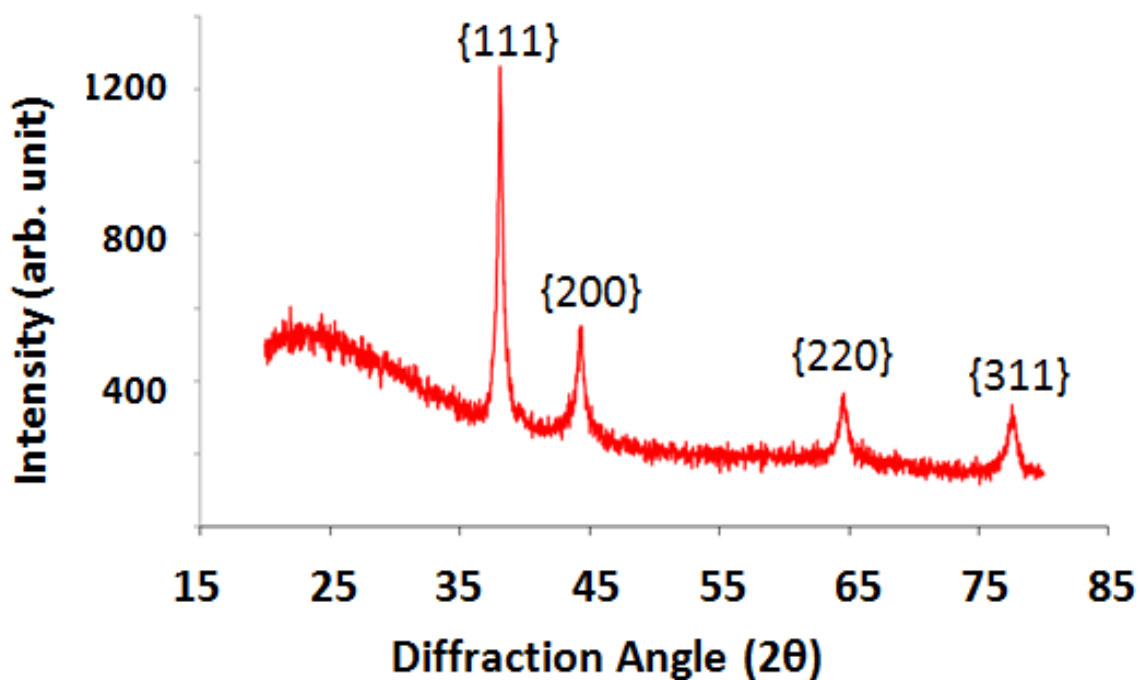
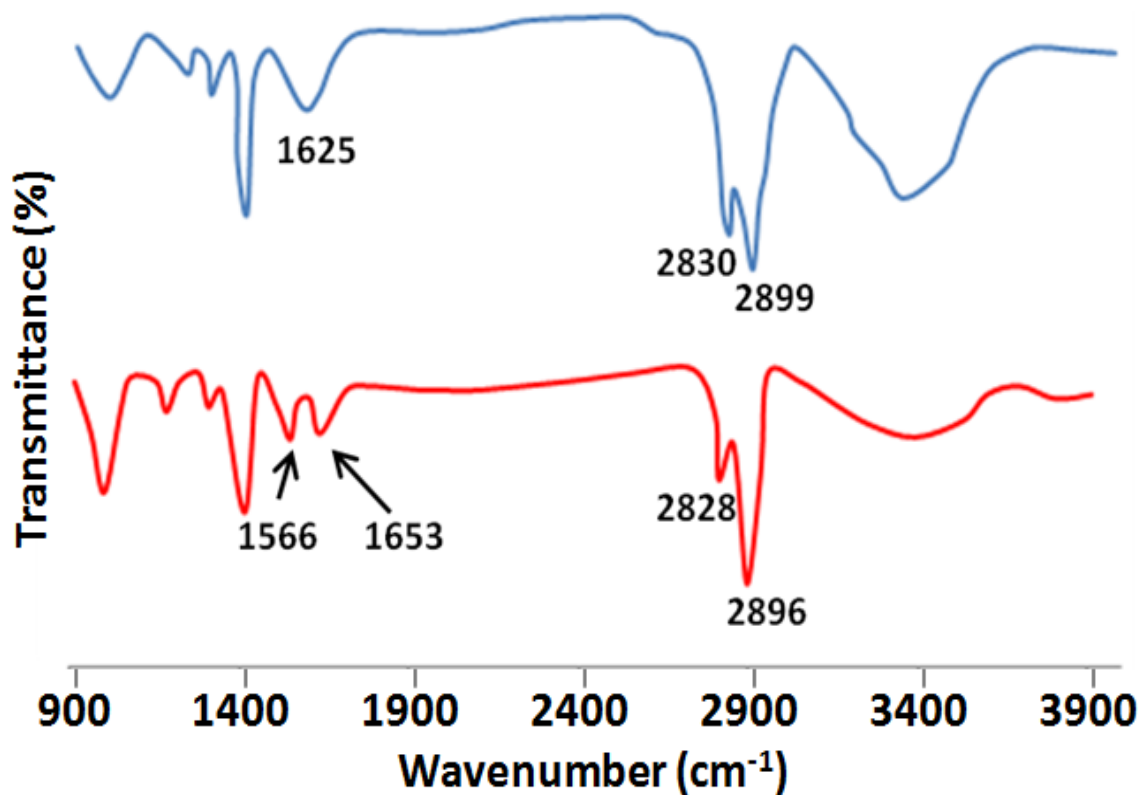


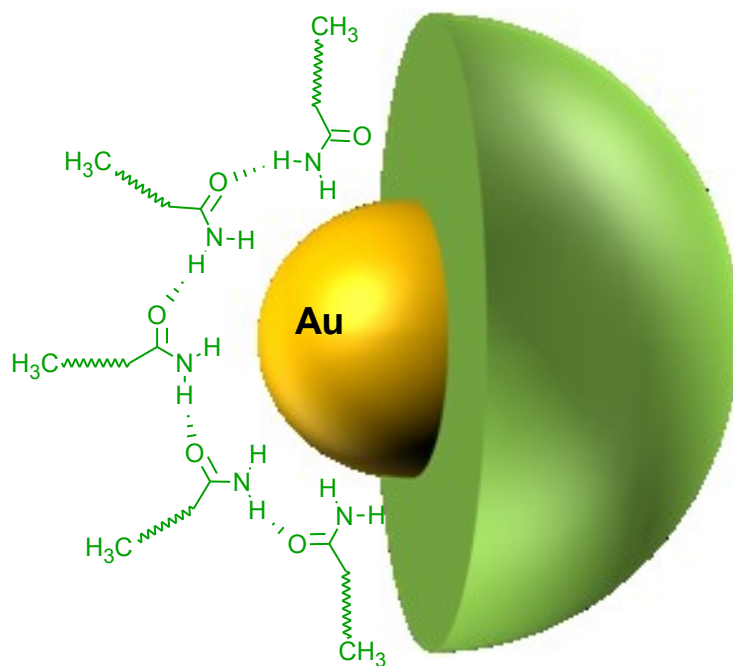
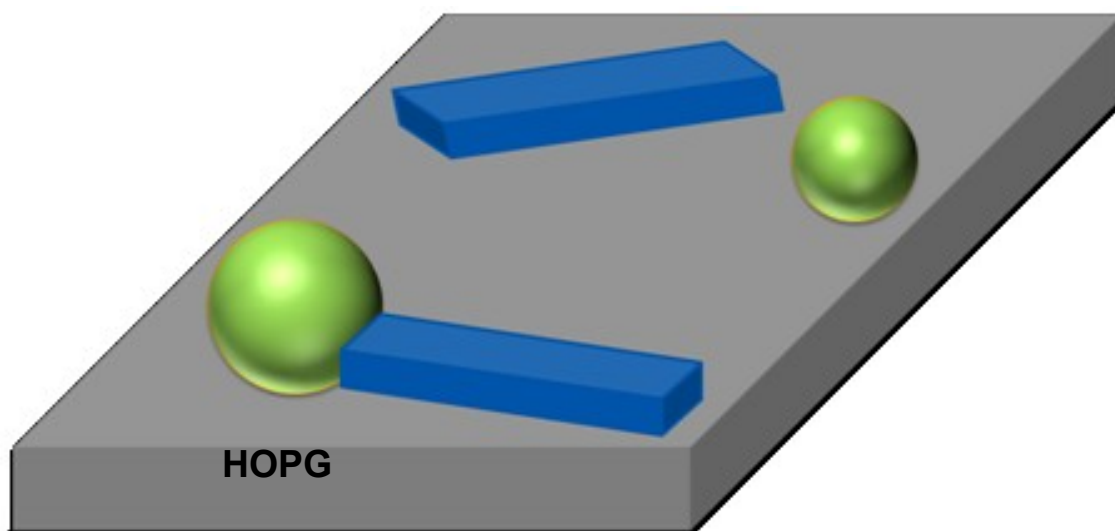
Figure 4.4 shows the FT-IR spectra of OA (blue) and OA-GNPs (red). Both spectra display the characteristic C-H stretching vibration frequencies,

$\sim 2830$  and  $\sim 2900$   $\text{cm}^{-1}$ . After the reaction, the N-H bending peak at  $1625$   $\text{cm}^{-1}$  disappears and new peaks associated with the amide bond,  $1566$  and  $1653$   $\text{cm}^{-1}$ , appear. Our results, consistent with those of others,<sup>47</sup> indicate that oxidation of oleylamine to oleylamide (Figure 4.5) accompanies the reduction of Au(III) to Au(0). The hydrogen bond formation among the amide groups improves the monolayer chemical stability. The OA-GNPs dissolve readily in chloroform. We conclude that the OA-GNPs are terminated by the methyl group rendering them hydrophobic.

Figure 4.4. FT-IR spectra of OA (blue) and OA-GNPs (red) powders.

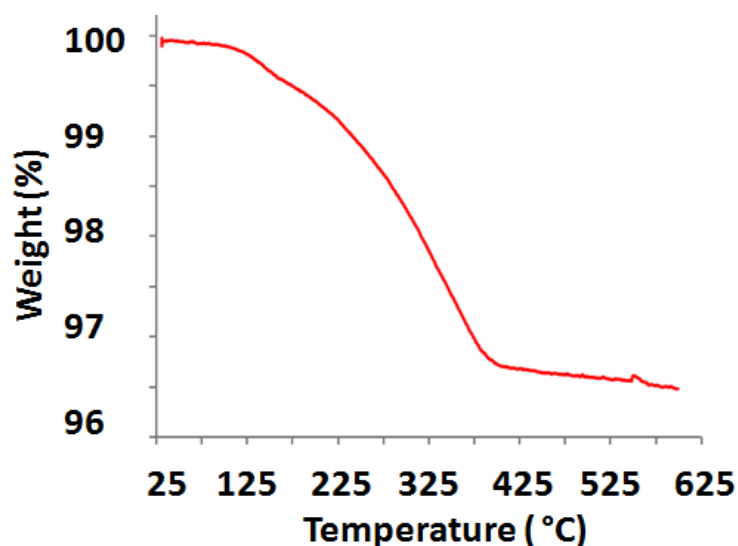


**Figure 4.5. NP/nanorod hybrid system generated by SMN. The NP consists of a core-shell structure with Gold core and H-bonded oleylamide monolayer shell. n-Carboxylic acid nanorods nucleated by the OA-GNP have a tendency to detach from the NP.**



In order to determine the surface coverage of OA monolayer on GNPs, TGA measurements were conducted as shown by Figure 4.6. The weight loss from 100°C to 375°C is attributed to the burn-off of the organic OA layer. The measured weight loss, 3.5% of the initial sample weight, corresponds to a molar ratio of Gold to oleylamide of 39.5. (Note that oleylamide's molecular weight is different from oleylamine's) In contrast, Au : N is 0.25 according to the EDS analysis. EDS overestimates the percentage of elemental N due to environmental impurities. The OA monolayer coverage on GNP surface in area per OA molecule is calculated to be  $27.6 \text{ \AA}^2$  using the average diameter of GNP (= 14.6 nm from PXRD), Au : OA molar ratio (= 39.5 from TGA), and density of Gold (=  $19.3 \text{ g/cm}^3$ ). For comparison, the limiting area per molecule for n-alkyl derivatives including carboxylic acids, amines, amides, and alcohols is 20–22  $\text{\AA}^2$ . The highest coverage of MUA on CdSe NPs in our previous work yields an area per thiolate of  $29.8 \text{ \AA}^2$ .<sup>46</sup>

**Figure 4.6. TGA graph of OA-GNPs.**





### 4.3.2. Film structure of n-carboxylic acids on HOPG

Alkanes and alkane derivatives such as n-carboxylic acids physisorb on HOPG with their carbon chain skeletal plane parallel to the HOPG basal plane. AFM studies of C<sub>14-26</sub>A's spin coated from alcoholic solvents showed a double-chain structure with a periodicity twice the molecular chain length on HOPG.<sup>4,46</sup> C<sub>30</sub>A, on the other hand, displayed an additional single-chain domain with one half of the double-chain periodicity. When switching the solvent from the ethanolic type to chloroform, the film nanostructures of C<sub>16-30</sub>A's on HOPG were found to be largely unchanged. Figure 4.7 shows typical AFM images of the carboxylic acids' films. The periodicity values of the double-chain domain pattern for C<sub>16</sub>A, C<sub>20</sub>A, C<sub>22</sub>A, C<sub>26</sub>A and C<sub>30</sub>A are reported in Table 4.1. C<sub>30</sub>A forms an additional single-chain domain with a periodicity of 3.9 nm. The film thickness is 0.3 ± 0.1 nm indicating a monolayer structure in which the carbon skeleton plane of the carboxylic acid lies parallel to the HOPG basal plane.

**Figure 4.7. AFM height images of C<sub>16-26</sub>A and C<sub>30</sub>A monolayers with double-chain domain and phase image for C<sub>30</sub>A monolayers with single-chain domain on HOPG. The z-range is 1 nm for C<sub>16-26</sub>A and C<sub>30</sub>A with double-chain domain and 5° for C<sub>30</sub>A with single-chain domain.**

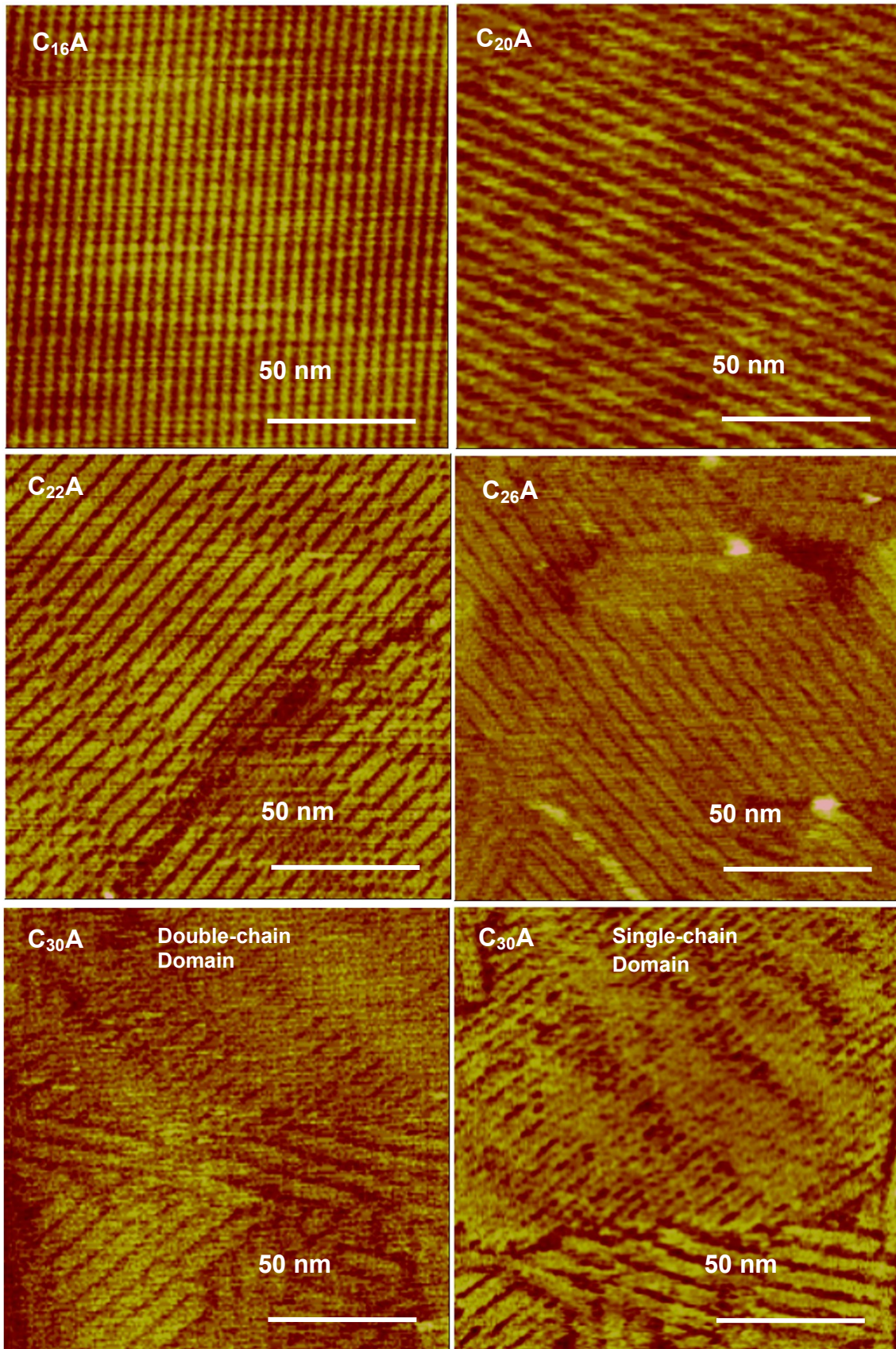


**Table 4.1. AFM results of the periodicity of carboxylic acid stripe patterns and the height and width of carboxylic acid nanorods.**

| Carboxylic acid   | Periodicity by AFM (nm) | Height of nanorods (nm) | Width of nanorods (nm) |
|-------------------|-------------------------|-------------------------|------------------------|
| C <sub>16</sub> A | 4.7                     | 0.8 ± 0.2               | 10.9 ± 2.4             |
| C <sub>20</sub> A | 5.6                     | 0.8 ± 0.3               | 7.0 ± 1.7              |
| C <sub>22</sub> A | 6.1                     | 1.1 ± 0.4               | 7.8 ± 2.3              |
| C <sub>26</sub> A | 7.0                     | 1.0 ± 0.3               | 10.0 ± 2.1             |
| C <sub>30</sub> A | 8.0                     | 0.8 ± 0.2               | 11.4 ± 2.6             |

#### **4.3.3. Film structure of n-carboxylic acids on HOPG in the presence of OA-GNPs**

In order to address the question whether the carboxylic nanorod formation requires a seed surface with the carboxyl group, a series of experiments were carried out using methyl-terminated OA-GNPs in chloroform. Figure 4.8 and 4.9 summarize the results of C<sub>16-30</sub>A's film structure in the presence of OA-GNPs on HOPG in low and high magnifications, respectively. The dimensions of the nanorods by AFM height sectional analysis are reported in Table 4.1. The nanorod structure is identical to the one induced by MUA-CdSe NPs, which displays the characteristic dimensions of the C-form carboxylic acid crystal structure exists in all these systems. No nanorods were obtained with carboxylic acids with fewer than 16 carbons. These shorter molecules formed a 2-D layer

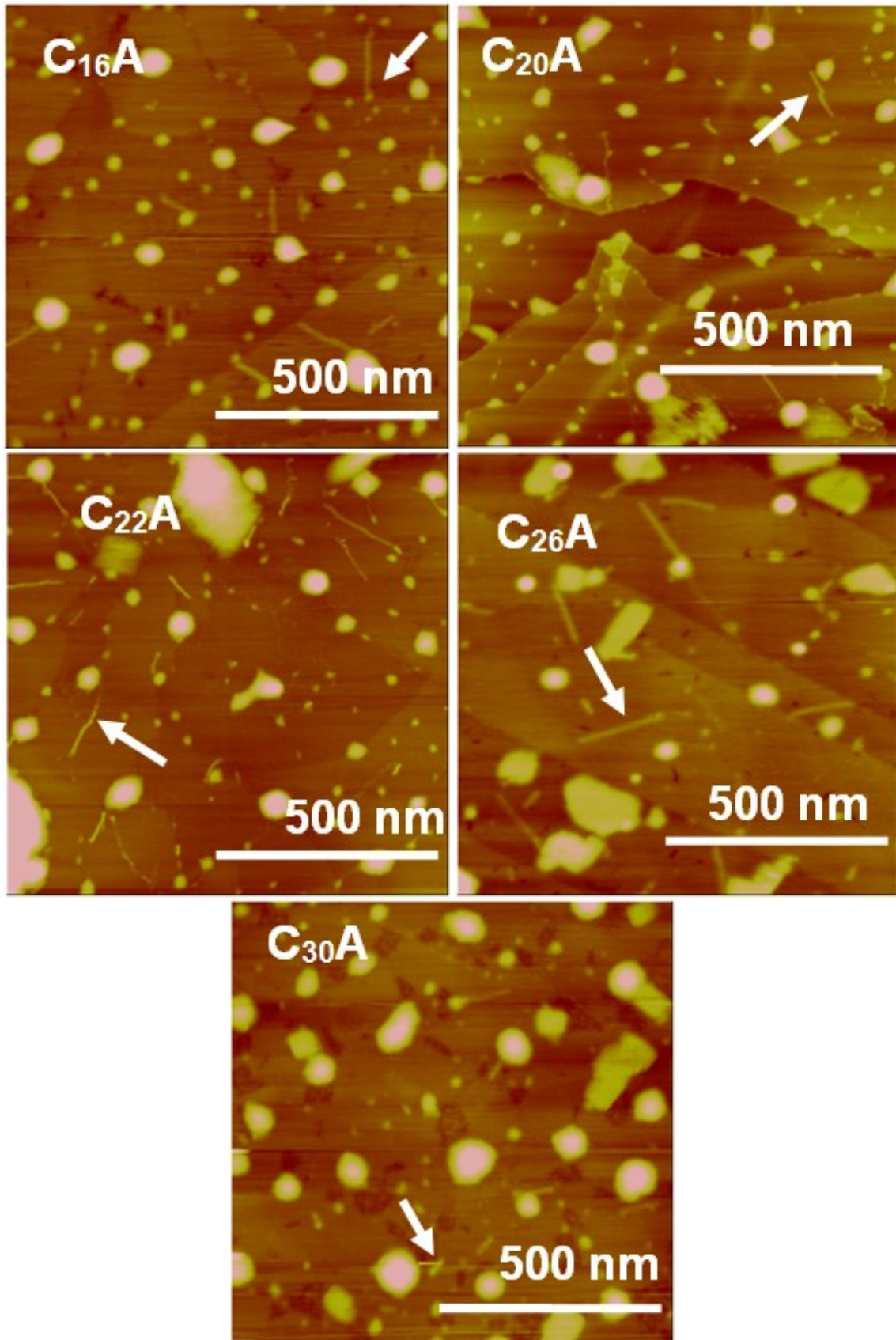
around the NPs. Carboxylic acids with more than 30 carbons were not studied. The C-form crystal structure of  $C_{18}A$  ( $P2_1/a$ ,  $Z = 4$ ) has the following lattice parameters:  $a = 0.9360$  nm,  $b = 0.4950$  nm,  $c = 5.0700$  nm, and  $\beta = 128.250^\circ$ . The individual nanorods display a fixed height,  $\sim 1$  nm, a width close to twice the chain length, and a stochastic length distribution in the range of 50–250 nm. The width of  $C_{20-30}A$ 's nanorods is  $\sim 2.6$  times the respective chain length, an apparent value due to tip convolution. The width of  $C_{16}A$  nanorods is  $\sim 5$  times its chain length suggesting the formation of nanorod doublets.<sup>46</sup> By comparing the nanorod dimensions and its expected crystal structure, we conclude that the nanorods are formed by carboxylic acid unit cells attaching to each other along the  $b$  direction in the C-form crystal structure during crystallization. The carboxylic acid nanorod possesses the unit cell dimensions (the smallest crystalline unit) in both width and height directions and it consists of a single bilayer row in the width direction with H-bonded carboxyl group in the center and terminal methyl groups at the sides.

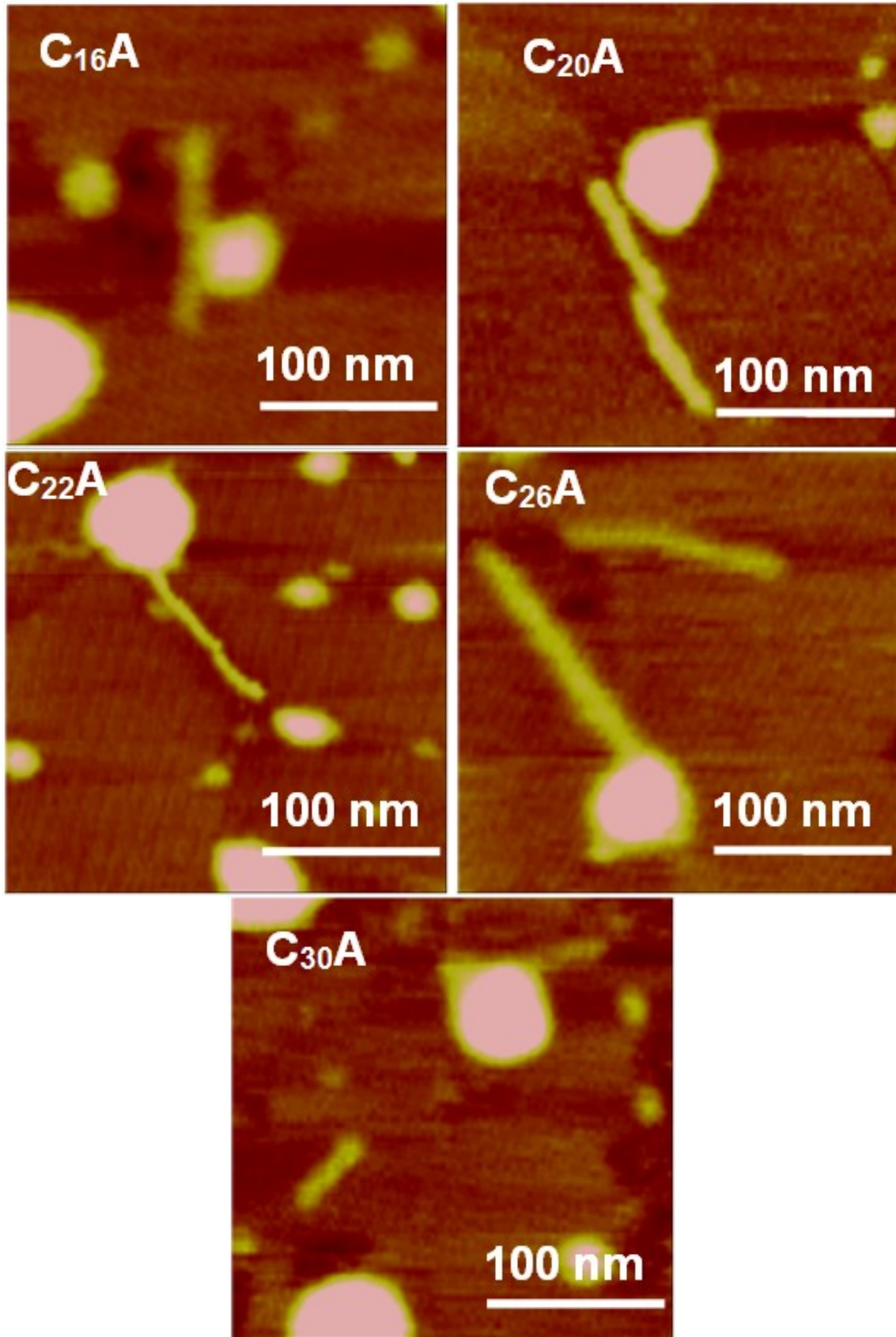
**Figure 4.8. Low-magnification (left column, z-range = 10 nm) AFM height images of n-carboxylic acids on HOPG in the presence of OA-GNPs.**

**(Next page)**

**Figure 4.9. High-magnification (right column, z-range = 5 nm) AFM height images of n-carboxylic acids on HOPG in the presence of OA-GNPs.**

**(Page after next page)**





Other observations consistent with the MUA-CdSe case are summarized here. 1) There is a seed size range that favors nanorod formation, in this case, seed with height of 4–10 nm (Figure 4.10). 2-D stripe layer domains form NPs larger than 10 nm in height. Carboxylic acid stripe domain in rectangular shape is another film feature presented in OA-GNP/C<sub>20-30</sub>A mixture (Figure 4.11). The stripe domain is found around the OA-GNPs. The size of the OA-GNPs ranges from 9.0 to 17.1 nm. The rectangular stripe domains display the same stripe period as the carboxylic acid monolayer stripe pattern. This is understood partially by the classical nucleation treatment of the nucleation energy barrier as a function of seed size and interfacial energies (or contact angle). Small seeds are ineffective nucleation agents because it does not lower nucleation energy. Large seeds effect is dominated by the contact angle as the curvature effect diminishes. In addition, interfacial strain arising from a highly curved interface, i.e., the surface of a small NP, may promote 1-D nanorod growth and suppress 2-D layer growth. 2) For the longest chain C<sub>30</sub>A, fewest nanorods are observed (Figure 4.8). In the competition between HOPG- and NP-mediated molecular ordering, longer carbon chain length favors the epitaxial interaction with HOPG because the epitaxial interaction with HOPG increases with increasing chain length. Thus, the epitaxial mismatch between the HOPG lattice and carboxylic acid molecules in the randomly oriented nanorods nucleated from the NP becomes increasingly prohibitive for nanorods composed of longer chains. Instead, they self-assemble into the nano-stripe pattern on HOPG.

Figure 4.10. Histogram of the percentage (%) of nanorod induced by NPs as a function of the height of the NPs.

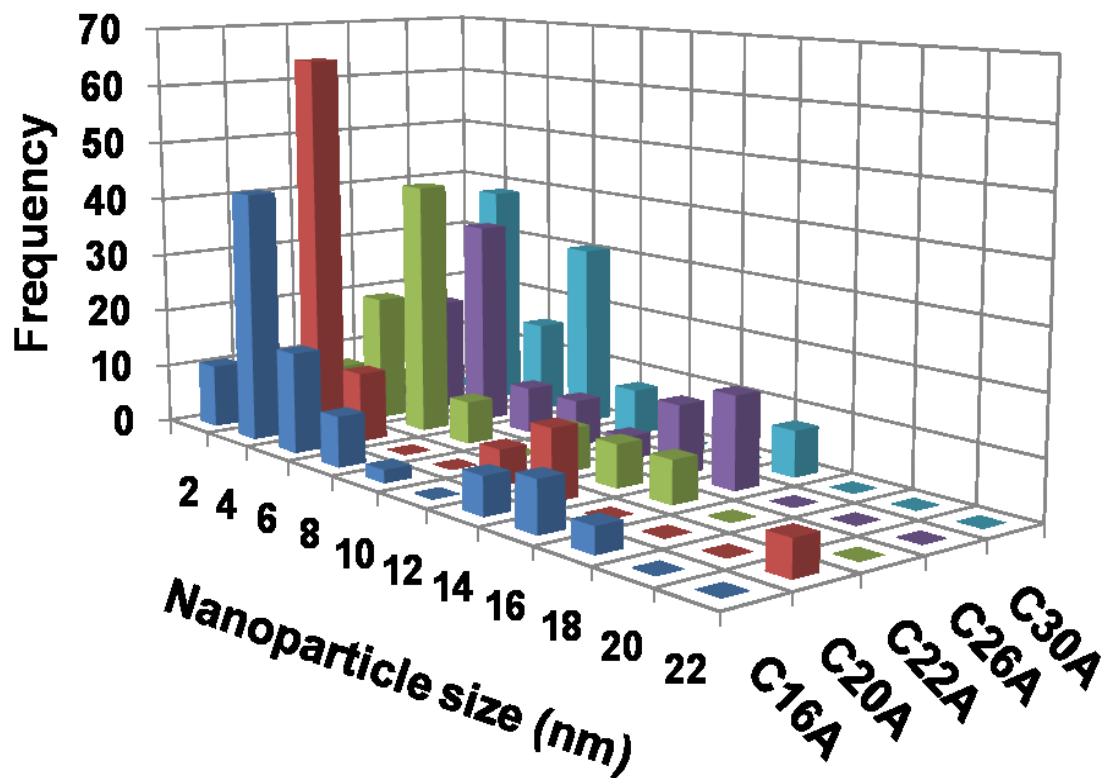
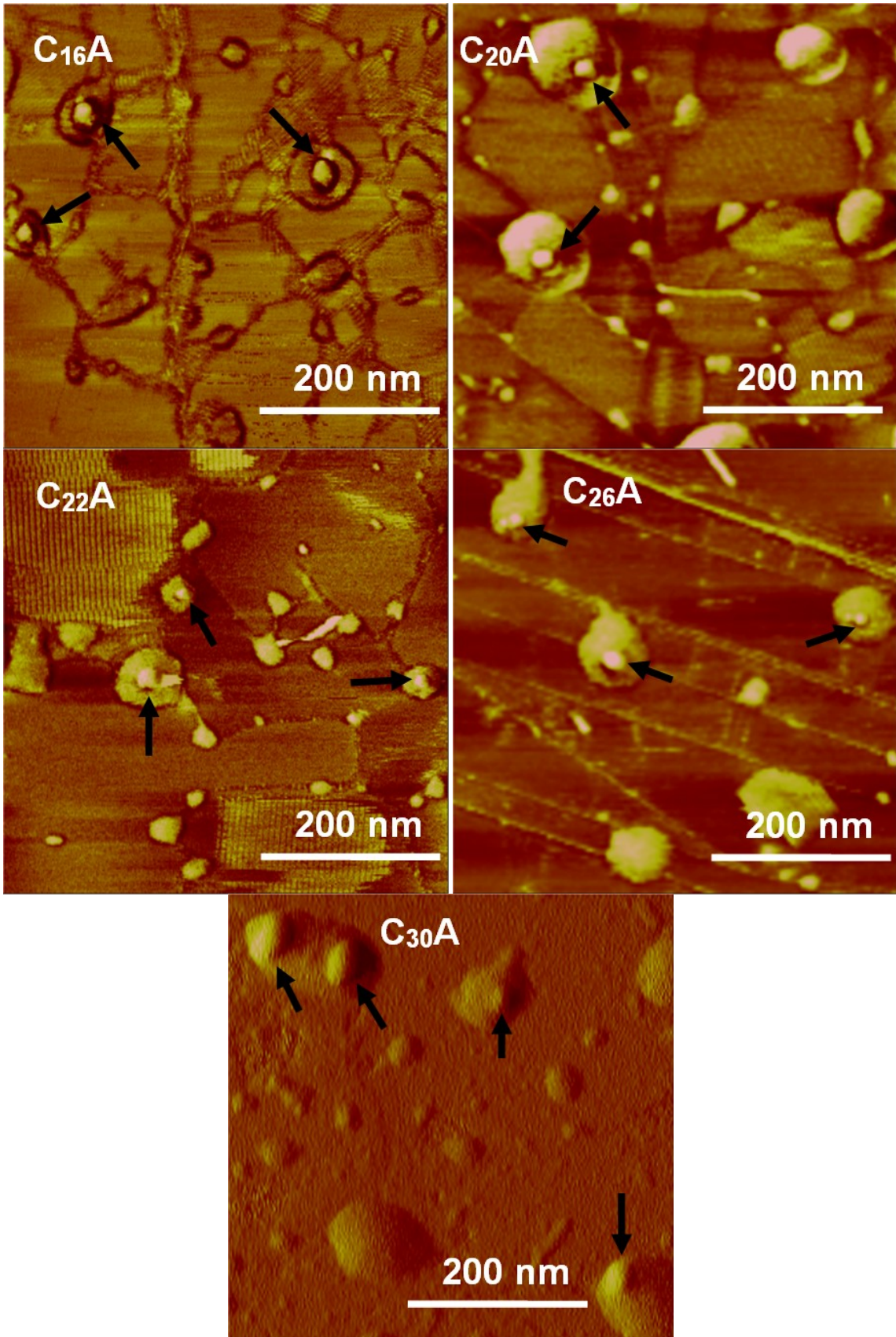


Figure 4.11. AFM phase images of C<sub>16-26</sub>A and amplitude image of C<sub>30</sub>A on HOPG in the presence of OA-GNPs. The z range is 30° for the phase images and 0.1V for the amplitude image.





Major difference between the nanorods induced by OA-GNPs and those produced by MUA-CdSe NPs<sup>4,46</sup> is that 1) fewer nanorods are produced by OA-GNPs and 2) a large percentage of the nanorods produced by OA-GNPs are detached from the seed (arrows pointing to this feature in Figure 4.9). The percentage of the detached nanorods of all nanorods formed was found to increase with increasing chain length. The percentage of detached nanorods is 22% for C<sub>16</sub>A, 26% for C<sub>20</sub>A, 55% for C<sub>22</sub>A, and 74% for C<sub>26</sub>A, respectively. There are not enough nanorods for meaningful statistical evaluation in the case of C<sub>30</sub>A. Among the attached nanorods, there are roughly equal number of nanorods oriented along the radial direction and tangential direction to the NP surface. The similar distribution of the two orientations is consistent with equal attachment probability of carboxyl dimers in the tangential and radial orientations to the particle seed surface. The similar size of the tangentially oriented nanorods and the radially oriented nanorods suggests that at least in this case the strain energy caused by misalignment of carboxylic acid nanorods on carboxylic acid monolayer-covered HOPG plays the more dominant role in limiting crystal growth width direction than the curvature constraint placed by the NP. In contrast, carboxylic acid nanorods are almost always found to be attached to MUA-CdSe NPs. In a molecular dynamics simulation study of seed-mediated colloidal crystallization,<sup>7</sup> elongated colloidal clusters form on the seed particle surface when the seed particle radius is at 5× the size of the colloidal particles. Molecular simulations predict a transition of nucleating clusters from elongated “1-D” shape to 2-D shell wrapping around the seed when the seed to nucleating compound

size ratio changes from 5 to 7. The authors hypothesize that the radially elongated cluster is induced by the high curvature of the small seed, which imposes an unsustainable strain for tangential growth. While the length scale of our system may not be pertinent to the colloidal crystallization simulated, our observations of the 1-D rods and 1-D to 2-D transition as a function of seed particle size are consistent with the 1-D clusters in the simulations. Snapshots show a transition from attached clusters to detached clusters during the nucleation process. An implication of this cluster detachment from the seed particle is that heterogeneous nucleation could still be the primary nucleation mechanism even in cases when nuclei are observed in bulk. Our observation of detached carboxylic nanorods provides experimental evidence of nucleus detaching from the seed surface predicted by the molecular simulation result. One possible reason for the detached nanorods in the OA-GNP case may be the lower interfacial bonding energy between the nanorod and the methyl group at the surface of the OA-GNP as compared to that between the same nanorod and carboxyl-terminated MUA-CdSe NPs. In the latter case, polar-polar and H-bond interactions are likely present to prevent nanorod detachment from the seed surface.

A closer examination of the AFM images shows the nanorods are oriented along the radial and tangential direction of the particle. Table 4.2 summarizes the relative percentage of the radial and tangential oriented nanorods,  $RP = (\text{Number of tangential nanorods}) / (\text{Number of radial nanorods})$ . The RP value is close to 1 for all the investigated carboxylic acids except C<sub>20</sub>A. More tangential nanorods

are observed for C<sub>20</sub>A with a RP value of 3.2. This may be due to the limitation of the collected data. The percentage of individual carboxylic acid nanorods increases with increasing carboxylic acid chain length (Table 4.2). The individual nanorods become a dominant feature (> 50%) for C<sub>22-30</sub>A's. For C<sub>26</sub>A and C<sub>30</sub>A less than 10% NPs have two nanorods attached to them. This is also consistent with our previous results from the MUA-CdSe system.

**Table 4.2. List of percentage of carboxylic acid nanorods in radial, tangential orientation and percentage of individual nanorods.**

| Carboxylic acid   | Radial (%) | Tangential (%) | Individual (%) |
|-------------------|------------|----------------|----------------|
| C <sub>16</sub> A | 40.0       | 38.3           | 21.7           |
| C <sub>20</sub> A | 56.5       | 17.4           | 26.1           |
| C <sub>22</sub> A | 22.6       | 22.6           | 54.8           |
| C <sub>26</sub> A | 12.0       | 14.0           | 74.0           |
| C <sub>30</sub> A | 29.6       | 18.5           | 51.9           |

#### 4.4. Conclusions

The work demonstrates a methodology of using monolayer-protected inorganic NPs as nucleation seeds for the creation of extremely narrow organic nanorods. OA-GNPs of high colloidal stability are synthesized and characterized by AFM, TEM, PXRD, EDS, FT-IR, and TGA. Homologous carboxylic acid films deposited on HOPG in the absence and presence of OA-GNPs are studied by AFM. Carboxylic acids with different chain length self-assemble into a stripe

nanopattern on HOPG due to favorable epitaxial interactions between the carbon chains and the HOPG crystalline lattice. This persistent nanopattern is perturbed by the presence of OA-GNPs and nanorods with random orientations are produced. The narrow width of the nanorod is attributed to two energetic factors. There is a significant mismatch between the carbon chain plane and HOPG for randomly oriented nuclei, which prevents the attachment of carboxyl dimers along the carbon chain direction (the c axis). The second factor is the high strain energy as a result of the highly curved surface of the NP in the tangential direction of the seed surface. This work shows that specific interactions between the seed surface and the crystalline compound are unnecessary for the nanorod formation since nanorods of identical structures are produced by methyl-terminated NPs. However, the tendency of nanorods to detach from the methyl-terminated NP surface points to the role of specific (polar/polar or H-bonding) interactions in keeping nucleating nanorods attached to the NP surface.

## CHAPTER 5

### A SUPRA-MONOLAYER NANOPATTERN FOR ORGANIC NP ARRAY

#### DEPOSITION

#### 5.1. Introduction

The self-assembled monolayers (SAMs) of organosilanes including n-OTS on silicon substrates have been extensively studied because of their potential applications in sensors and electronics.<sup>48-50</sup> OTS molecules chemically adsorb on the substrate surface (silicon dioxide) through the Si–O–Si covalent bond. The stability of the SAMs is further improved by the Si–O–Si bond between neighboring surface-bound OTS molecules. The close-packed OTS monolayer has been characterized by ellipsometry, X-ray reflectivity, and contact angle goniometry to exhibit a thickness of 2.6 nm, molecular packing density about  $21\text{\AA}^2/\text{molecule}$ , and water contact angle reaching  $110^\circ$ .<sup>51,52</sup> In our previous work,<sup>50</sup> we have obtained smoother OTS monolayers using CVD while the OTS monolayers deposited from the liquid phase often contain molecular aggregates. The precise control of the CVD is however complicated by the role of water in the competitive condensation and polymerization reactions of the OTS. Trace water is necessary for organosilane condensation reaction with the hydroxyl groups at the silicon substrate; however, excessive water causes polymerization of the organosilane molecules that result in vertical growth of multilayer islands.<sup>53,54</sup>

Particle lithography (also known as nano-sphere lithography) relies on immersion capillary force between monodisperse colloidal particles to produce

films of colloidal crystals on solid substrates.<sup>55,56</sup> Two-stage mechanism of the colloidal array formation has been proposed. In the first nucleation stage, particles start to order due to the immersion capillary force when the thickness of the water layer is close to the particle diameter. In the second crystal growth stage, water evaporation from the menisci gives rise to a convective flux of particles toward the nucleus. The combination of the organosilane SAM and particle lithography has yielded a simple yet reliable method to manufacture nanoring patterns on silicon substrates.<sup>26,57,58</sup> Organosilanes including OTS and silanes with amine and poly(ethylene oxide) functional groups have been deposited as nanorings on oxidized silicon and mica substrates. The surface density and sizes of the organosilane nanorings can be simply varied by the colloidal particle size. The nanopattern morphology has been found to be sensitive to the drying conditions. It is conceivable that the organosilane nanopattern can be used as a new type of templates to regulate the deposition of NP arrays of diverse materials in a similar way as demonstrated on other types of micropatterns and nanopatterns.<sup>29,59-64</sup> For example, calcite NPs could be deposited on the organosilane nanoring pattern following a similar mechanism of calcite crystallization on micropatterns of alkanethiol SAMs.<sup>29</sup> Hydrophobic drug NPs could be deposited on the organosilane nanoring pattern by utilizing the amphiphilic nanostructure of the substrate as demonstrated in aspirin deposition on self-assembled phospholipid nanopattern on the graphite substrate.<sup>62</sup>

This study explores the competitive nature of the surface condensation vs. polymerization reaction of the OTS molecules on oxidized silicon substrates

covered by the lithographical colloidal layers. Monodisperse PS particles with diameters of 300 nm and 900 nm are used. We investigate the CVD conditions that favor the polymerization reaction in the interstitial space of the colloidal crystal, which results in the OTS supra-monolayer nanopattern with a thickness exceeding that of the predominant OTS monolayer nanopattern. The OTS supra-monolayer patterns are used as “nano-flasks” to induce area-selective precipitation and nucleation of small organic molecules including n-docosane, aspirin, and clarithromycin. We demonstrate that nucleation and crystallization of small organic molecules such as aspirin and n-carboxylic acids are influenced by nanoconfinement imposed by nanopatterns<sup>62,63,65</sup> and NP nucleation seeds.<sup>4,46,66</sup> In this work n-docosane is chosen because it belongs to the n-alkane homologous series with well defined chain length-dependent crystallization behavior. In addition to evaporative crystallization from the solution phase, n-docosane can be re-crystallized from the melt phase at 43 °C, close to room temperature. Aspirin and clarithromycin are active pharmaceutical ingredients (APIs) that are crystalline in nature. Crystallization of the APIs at the nanoscale is relevant to drug formulation to improve bioavailability. The supra-monolayer OTS nanopattern is found to be an effective template for NP array deposition of all three chemicals with uniform particle size and spatial distribution as dictated by the OTS pattern size. The deposited particle size can be varied by the solution concentration. The research demonstrates a particle lithographical method that overcomes the pattern thickness limit of the organosilane SAM and its potential use for high-throughput crystallization trials. The solution-based particle array



formation method can be scaled up for nanomanufacture of small-molecule NPs of drugs, dyes, and semiconductors.

## 5.2. Experimental

**Materials.** The following chemicals have been used as received: n-OTS (95%, Gelest), hydrogen peroxide (30% in water, Fisher), sulfuric acid (98% in water, Fisher), sodium chloride (99%, Fisher), magnesium chloride (> 99%, Fisher), potassium sulfate (> 99%, Fisher), ethanol (200 proof, Fluka), chloroform (99.9%, Fisher), diethyl ether (> 99%, Alfa Aesar), 1-butanol (99.9%, Fisher), heptane (99%, Fisher), n-docosane ( $C_{22}H_{46}$ , 99%, Aldrich), aspirin ( $C_9H_8O_4$ , > 99%, Sigma), clarithromycin ( $C_{38}H_{69}NO_{13}$ , > 95%, Sigma). Deionized water from the Barnstead Nanopure water purification system (electrical resistivity 18 M $\Omega$ -cm) has been used.

One-sided polished N type silicon (111) wafers (test grade, with resistivity of 1–20  $\Omega$ -cm and thickness of  $525 \pm 50$   $\mu$ m) have been purchased from the Wafer World. Organic residues on the silicon wafer have been removed by immersing it in 3:1 mixture of sulfuric acid and 30% hydrogen peroxide for 1 h (caution: this solution is highly corrosive and needs to be handled with care!). The substrate has been washed with copious amounts of deionized water and dried in stream of compressed  $N_2$ .

**Particle lithography.** Monodisperse PS microspheres with diameters of 900 nm (PS900) and 300 nm (PS300) have been used in particle lithography. Both have been purchased from the Thermo Scientific. The PS particle

suspension has been centrifuged for 15 min at 13,000 rpm (Thermo Scientific, Sorvall Legend XTR Centrifuge). The solid pellet at the bottom of the centrifuge tube has been re-dispersed in deionized water to a concentration of 1 w/v%. Approximately 30  $\mu\text{L}$  of the suspension has been placed on a  $1 \times 1 \text{ cm}^2$  silicon wafer substrate for 30–45 min in the ambient laboratory atmosphere (relative humidity 40%) for colloidal crystallization. The substrate has been vacuum-dried for 30 min in order to remove excess water.

The stepwise procedure to create the OTS nanopattern and subsequent deposition of NPs of small organic molecules is illustrated by Scheme 5.1. The OTS nanoring pattern on the PS colloidal crystal template is conducted by modifying a literature procedure.<sup>26,57,58</sup> The PS template is placed in a desiccator with 100  $\mu\text{L}$  OTS. The desiccator is maintained at 70 °C for 90 min for the CVD. The relative humidity in the desiccator is varied by using saturated salt solutions and measured by a humidity meter (HX71-MA, Omega) immediately prior to the OTS reaction. Two desiccators are used. One is 0.13 L in volume and the other is 5.2 L. In both reactors, the sample, silane source, and humidity meter are placed close to each other with the sample placed 2 cm apart from the silane source and the humidity meter 1 cm apart from the sample. After the reaction, the PS particles are removed by sonication (Branson, Ultrasonic Cleaner, 1510R-MTH) in a 1:1 mixture of ethanol and deionized water for 30–60 min to reveal the OTS nanorings.

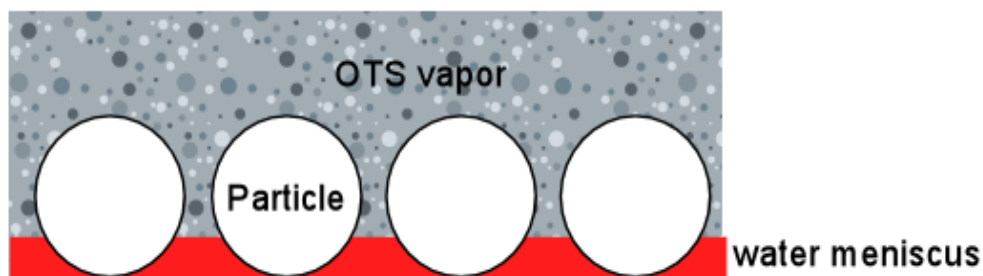
**Scheme 5.1. Side view of steps that lead to OTS supra-monolayer nanoring formation (step 1–4) and deposition of small molecule NP arrays on the**

**OTS nanopattern (step 5).**

Step 1: colloidal crystallization



Step 2: start of the CVD



Step 3: end of the CVD



Step 4: particle template removal



Step 5: small molecule deposition



**Deposition of small organic molecules on the OTS nanoring nanopattern.** By trial and error, we have found that droplet solutions in the range of 40  $\mu\text{L}$  are ideal for organic NP deposition on the 1  $\text{cm}^2$  OTS nanorings by evaporative re-crystallization. Lower amount results in incomplete coverage of the substrate by the solution while higher amount results in thick deposits masking the nanorings. The droplet amount is further adjusted for each type of materials at different solution concentrations. In melt re-crystallization of n-docosane, it is necessary to limit its amount deposited on the substrate so that the nanoring pattern is not completely masked by the n-docosane layer. This has been achieved by evaporative deposition of sufficiently dilute n-docosane solution. The substrate covered by the n-docosane thin film is heated at 90  $^{\circ}\text{C}$  (above its melting temperature) for 30 min. The substrate is cooled immediately to -20  $^{\circ}\text{C}$ .

**Characterization.** The particle lithography and organic NP deposition are characterized by AFM and field-emission SEM (FE-SEM). AFM images are obtained with the J scanner (maximum scan area = 125  $\times$  125  $\mu\text{m}^2$ ) (Nanoscope IIIa, VEECO). Height, amplitude, and phase images are obtained in the tapping mode in ambient air. Uncoated silicon probes (TESP, VEECO) with a factory-specified spring constant of 40 N/m, length of 125  $\mu\text{m}$ , width of 40  $\mu\text{m}$ , and nominal tip radius of curvature less than 10 nm are used. The scan rate used is in the range of 0.5–1 Hz depending on the scan size. Integral and proportional gains are approximately 0.4 and 0.8, respectively. All reported AFM images are height images unless specified. Height images have been plane-fit in the fast

scan direction with no additional filtering operation. Images are analyzed using the Nanoscope software from Digital Instruments (Version 5.12). The various lateral and vertical sizes are measured manually using the sectional height analysis command. The NP volumes are measured by the bearing analysis command.

The nanostructures are characterized by a thermal FE-SEM (JEOL JSM-7600F). A thin layer of gold (~10 nm) is sputter-coated (EffaCoater) on the sample for better image resolution. The FE-SEM images are obtained at a working distance of 8 nm and voltage of 15 kV.

The surface hydrophobicity is measured with an NRL contact angle goniometer (Model 100, Rame-Hart) in the laboratory atmosphere. A 10  $\mu$ L water droplet is placed on the substrate and the static contact angles are measured on both sides of the droplet. Three droplets are placed at various spots on the substrate and the average readings are reported. The typical error is  $\pm 3^\circ$ . The crystalline structure of aspirin NPs is analyzed by FT-IR (Perkin Elmer Spectrum 400).

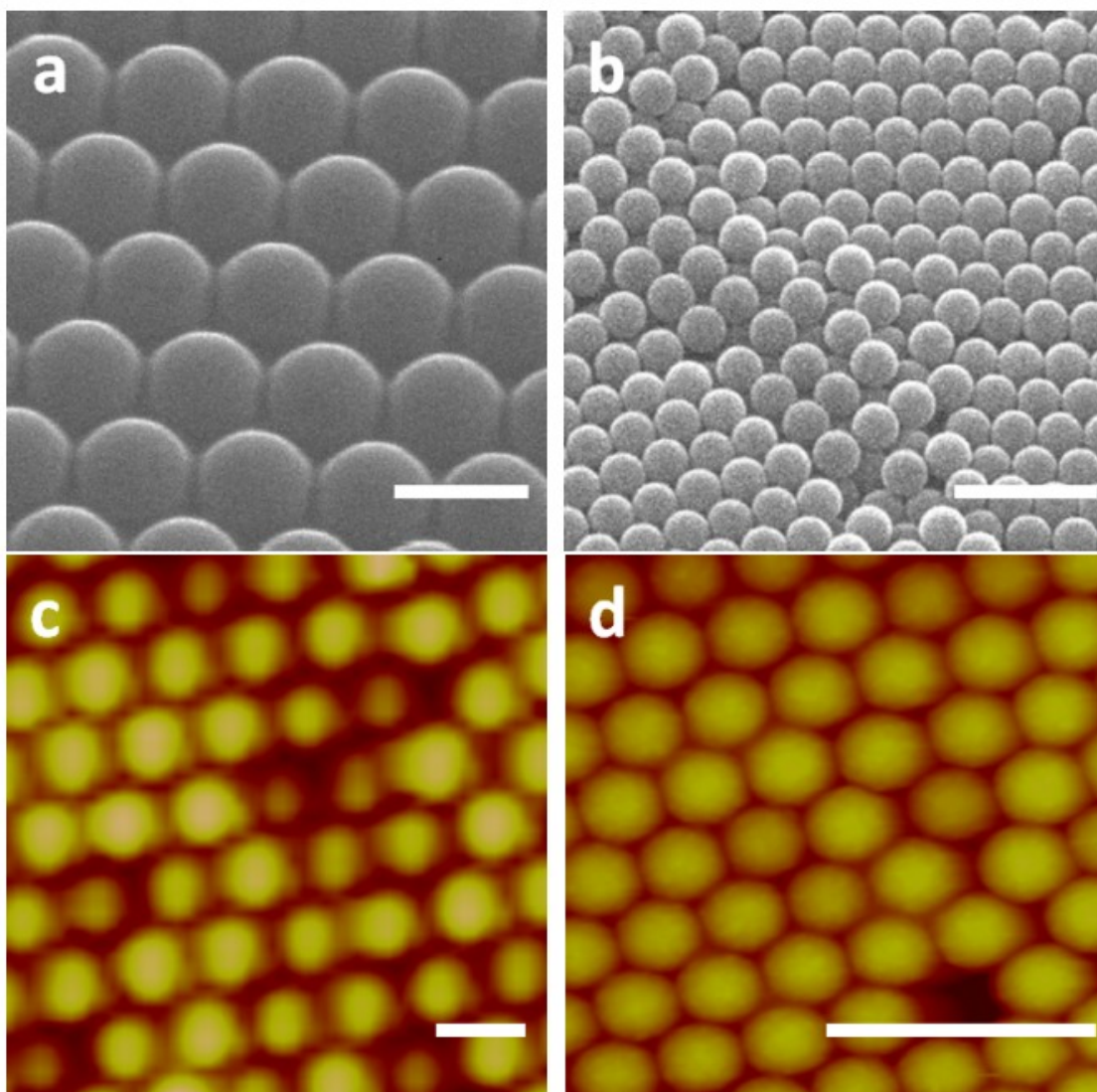
### **5.3. Results and discussion**

#### **5.3.1. Supra-monolayer nanopattern formation by particle lithography**

By following literature methods,<sup>55,56</sup> we are able to form large single crystalline domains of PS colloidal crystals on the oxidized silicon wafer. Figure 5.1 shows the colloidal layers formed by PS900 and PS300 particle lithography on the oxidized silicon wafer. The average single crystalline domain size is

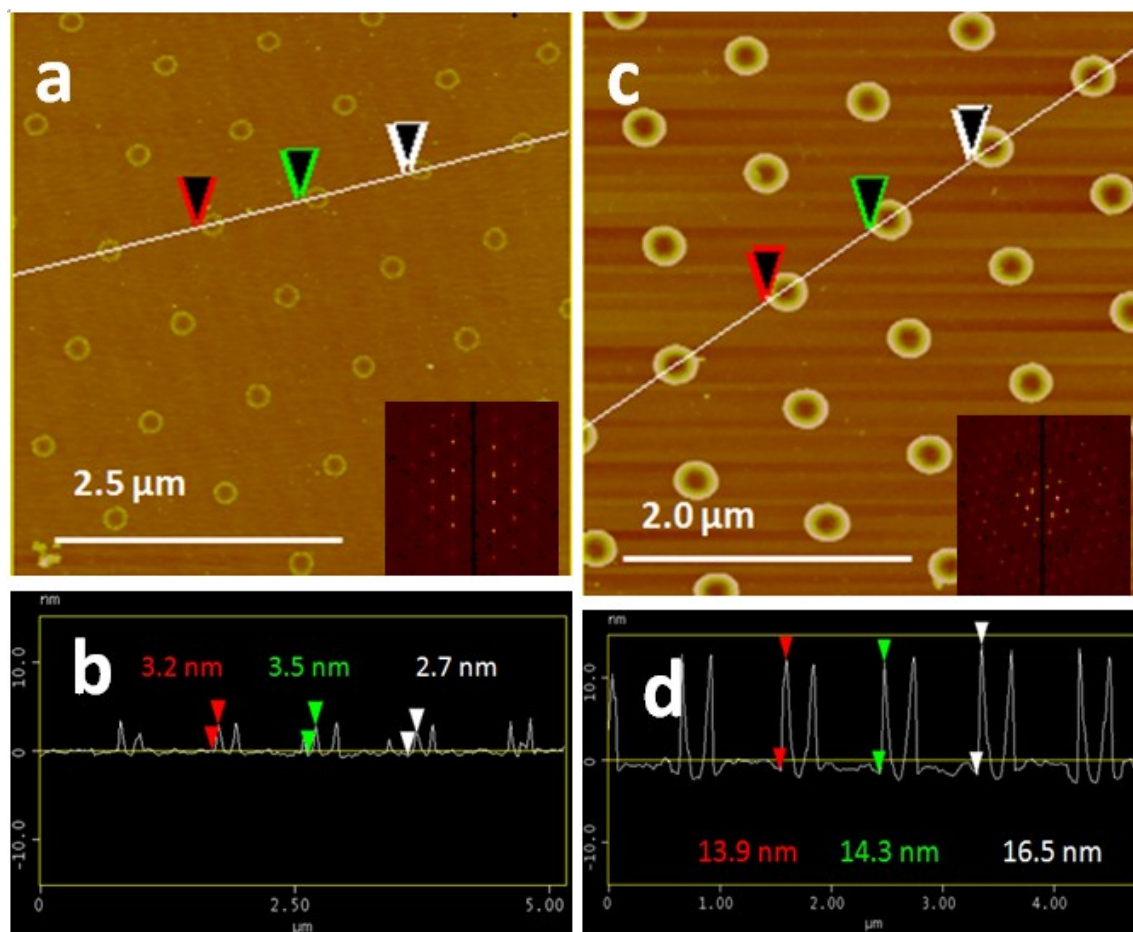
estimated to be 90  $\mu\text{m}$  for the PS900 and 30  $\mu\text{m}$  for the PS300. The SEM and AFM images show that more than one layer of PS particles are deposited though we find that the subsequent OTS pattern is templated only by the immediate interfacial particle layer on the substrate.

**Figure 5.1. SEM (a and b) and AFM height images (c and d, z range = 300 nm) of the PS900 (a and c) and PS300 (b and d) colloidal layers deposited on the oxidized silicon wafer. The bar length = 1  $\mu\text{m}$ .**



The silicon wafer substrates covered by the PS900 and PS300 colloidal layers are used as templates for OTS nanoring formation. The OTS nanorings are the result of surface hydrosilation initiated by nanoscopic amounts of water confined to the substrate by the colloidal particles.<sup>57</sup> We have produced both the expected monolayer pattern and the unexpected thicker pattern (referred here as the supra-monolayer pattern). Figure 5.2a-b shows the expected OTS nanorings made with the PS900 template. The high degree of order of the nanorings is shown by the intense fast Fourier transform (fft) of the AFM image. The nanopattern thickness is measured by AFM sectional height analysis to be  $3.0 \pm 0.5$  nm ( $N = 50$ ), which is consistent with the SAM structure of the OTS monolayer. In contrast, we have also observed OTS nanopatterns with thickness exceeding that of the OTS monolayer using the same particle templates but under different reaction conditions. Figure 5.2c-d shows an OTS supra-monolayer pattern with a pattern thickness of  $14.4 \pm 2.4$  nm ( $N = 50$ ) with the PS900 template. The reaction conditions that yield the supra-monolayer patterns are investigated and are the subject of the remaining report.

**Figure 5.2.** (a) AFM height image of the OTS monolayer nanorings and corresponding fft analysis (inset). Z-range = 30 nm. (b) The sectional height profile along the line in (a). (c) AFM height image of OTS supra-monolayer nanorings and corresponding fft analysis (inset). Z-range = 60 nm. (d) The sectional height profile along the line in (c).



The OTS deposition on colloidal particle templates is studied as a function of reaction time, relative humidity, and reactor volume. The OTS amount is fixed at 100  $\mu\text{L}$ . First, the reaction time is varied from 5 to 720 min at a relative humidity of 5% and temperature of 24  $^{\circ}\text{C}$  in the 0.13 L reactor. The OTS



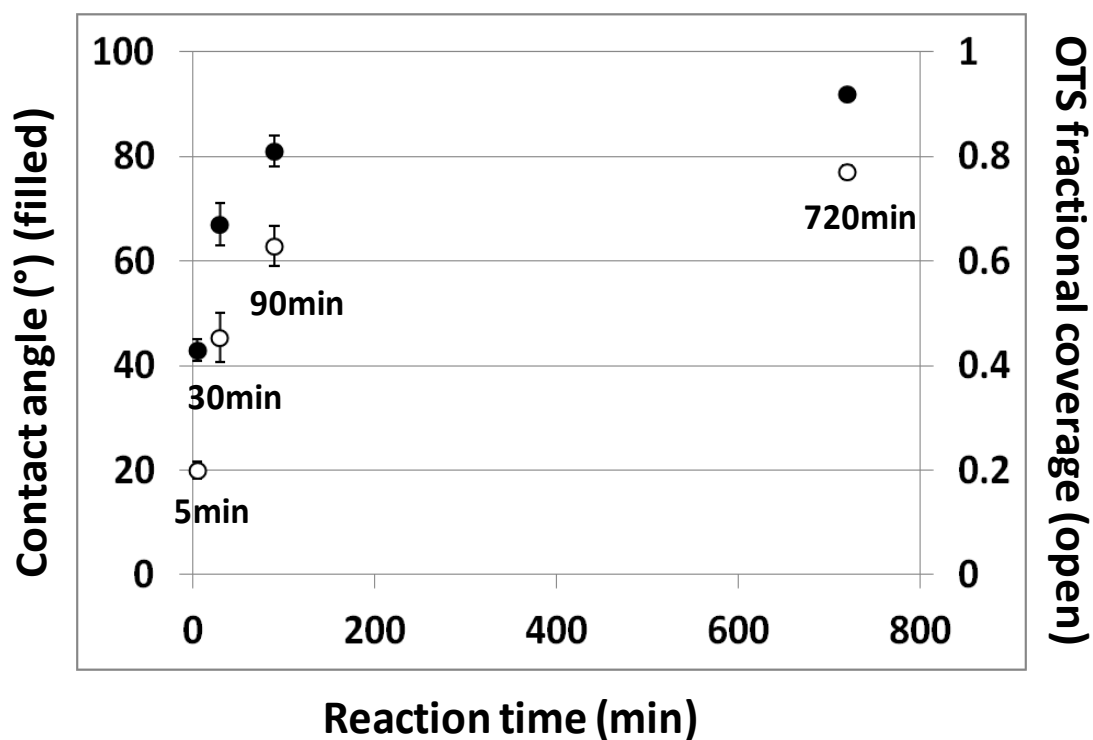
deposition is characterized by contact angle measurements and AFM. Figure 5.3 shows the water contact angle variation with the reaction time. The contact angle increases steadily during the initial 90 min of reaction and reaches a maximum value of  $92^\circ$  at 720 min. The OTS fractional area coverage ( $f$ ) is estimated from the contact angle value ( $\theta$ ) using the Cassie equation (Eq.1) assuming the Wenzel state<sup>67</sup> and is plotted in Figure 5.3:

$$\cos\theta = f*\cos\theta_{\text{OTS}} + (1-f)*\cos\theta_{\text{S}} \text{ (Eq.1)}$$

$\theta_{\text{OTS}}$  and  $\theta_{\text{S}}$  are the contact angles of the OTS monolayer and substrate (oxidized silicon wafer), which are assumed to be  $110^\circ$  and  $0^\circ$ , respectively.<sup>68</sup> The effect of surface roughness is neglected in this calculation.  $f$  is calculated to be 0.20 when  $\theta = 43^\circ$  at 5 min reaction time and 0.77 from when  $\theta = 92^\circ$ . The actual  $f$  value can be determined from the AFM images. The  $f$  value in the PS900 case is determined to be 0.14 by counting an average of 24 OTS rings each with an outer diameter of 379 nm and inner diameter of 160 nm in a  $4 \times 4 \text{ m}^2$  area (Scheme 5.2a). A closer look at the AFM sectional height profile of the nanorings shows a spherical cap bottom indicating various amounts of OTS deposited inside the ring tapering off toward the ring center (Figure 5.4a and Scheme 5.2b). Taking into account the OTS deposition inside the ring by approximating the nanoring to a spherical disk (Scheme 5.2c) with a disk diameter of 379 nm the  $f$  value is calculated to be 0.17. This is closer to the value based on the contact angle. Increasing amount of OTS is deposited outside the rings with increasing reaction time. Figure 5.4b shows the AFM data at 720 min reaction time. In contrast to the 5 min case (Figure 5.4a) there is a height difference between the

area outside the ring and the bottom of the ring. The height difference, ~3 nm, closely matches the OTS monolayer thickness. Therefore one can conclude that the increase in contact angle is due to increasing OTS deposition outside the nanoring with reaction time to yield a hydrophobic nanoring nanopattern (Scheme 5.2d).

**Figure 5.3. Contact angle and corresponding OTS fractional surface coverage on the oxidized silicon wafer as a function of the reaction time.**



**Scheme 5.2. Side view of various proposed nanostructures of the nanorings used in the fractional surface coverage and contact angle calculations.**

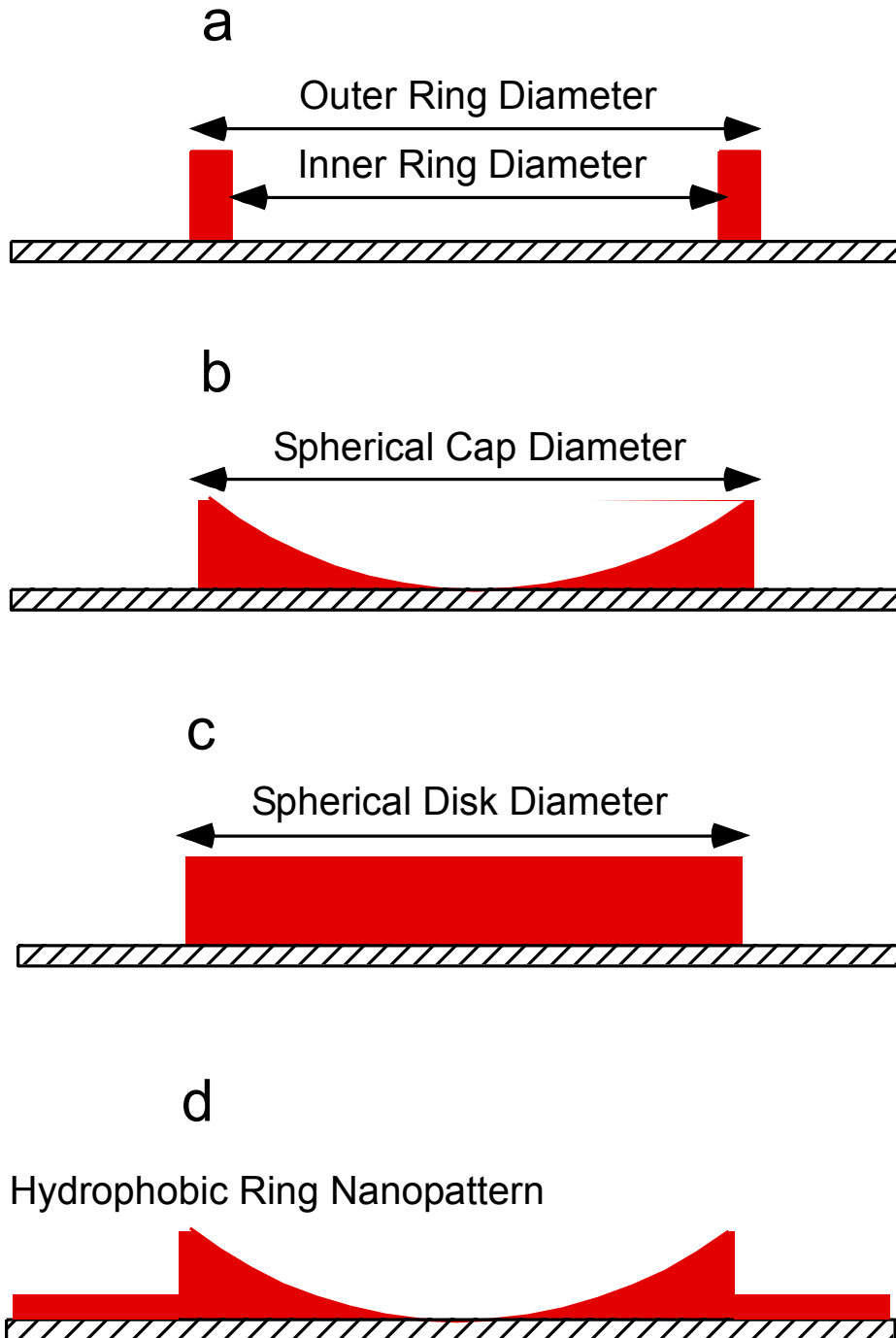
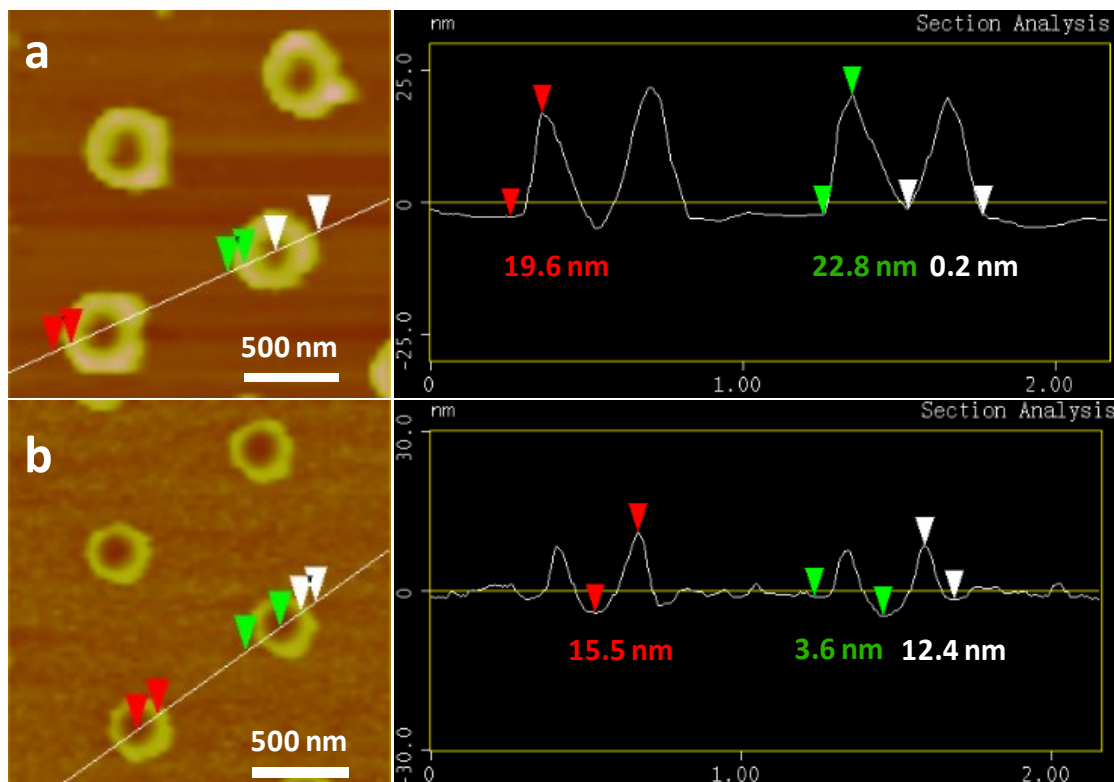


**Figure 5.4. AFM height images of the OTS nanorings after 5 min reaction time (a) and 720 min reaction time (b) using the PS900 template. Z-range = 60 nm.**

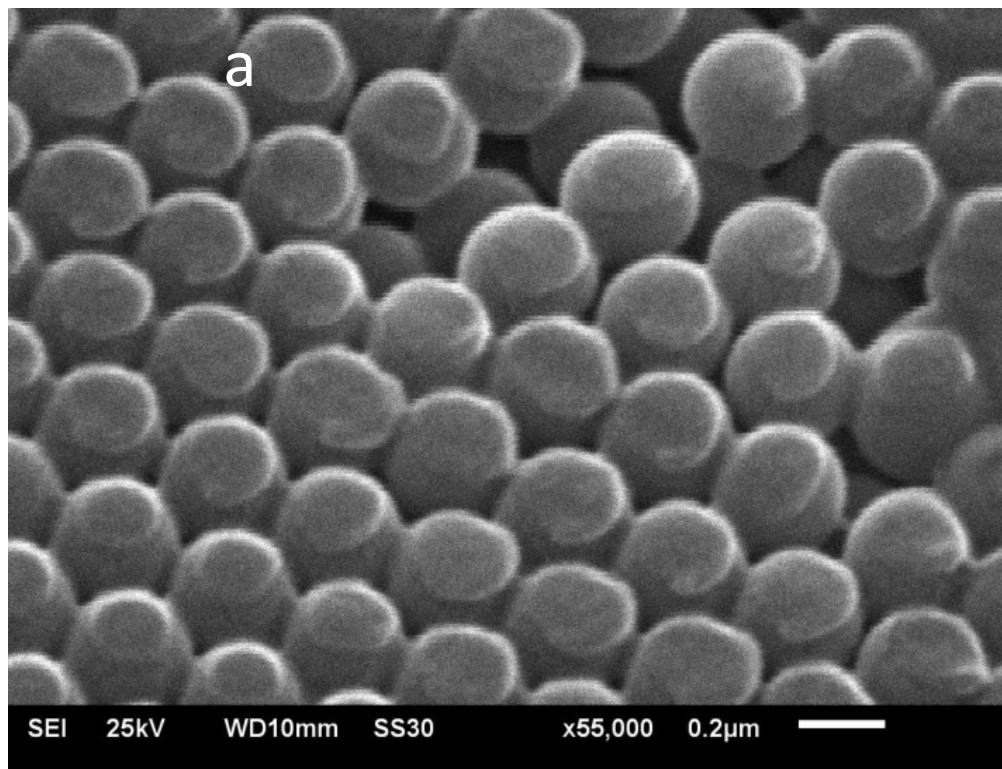


The OTS nanopattern thickness varies between 14 and 23 nm with the maximum value reached at the beginning of the reaction (5 min). After reacting 30 min and longer the nanoring height remains at 14–17 nm. SEM has been used to examine the PS particles removed from the substrate after being used as the template for OTS nanoring formation. Figure 5.5a shows the particles removed from the substrate by an adhesive tape as has been previously demonstrated by others.<sup>69</sup> The round patches of OTS film can be seen on top of the PS particles. Figure 5.5b shows the remnants of the OTS film in the

interstitial region among neighboring PS particles when particles are sheared off the substrate by sonication. Some remnants are broken while others are still connected to the opposing PS particles. This suggests that the top portion of the OTS nanorings may be broken off when the PS particles are sheared off the substrate during the removal process. Such remnants are only observed after prolonged reaction suggesting the higher nanoring height at 5 min is probably due to weaker adhesion at the OTS film and PS particle interface at the beginning of the reaction. It may be possible increase the nanopattern height by preventing tearing of the OTS nanopattern during removal of the PS template.

**Figure 5.5. Electron microscopic images of PS particles PS300 (a, FE-SEM) and PS900 (b, TEM) removed from the substrate after OTS CVD reaction.**

The bar length is 200 nm for (a) and 100 nm for (b).



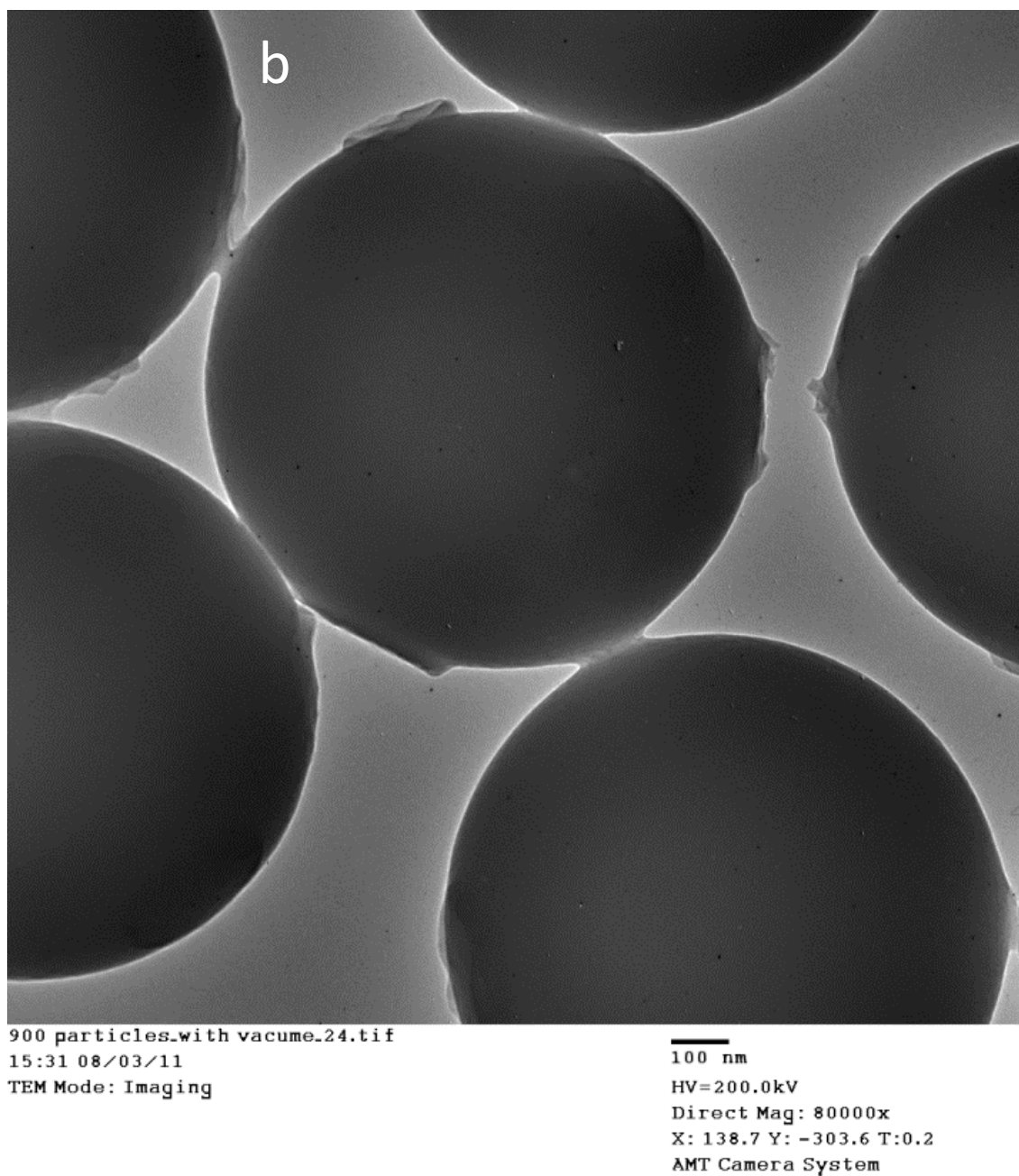
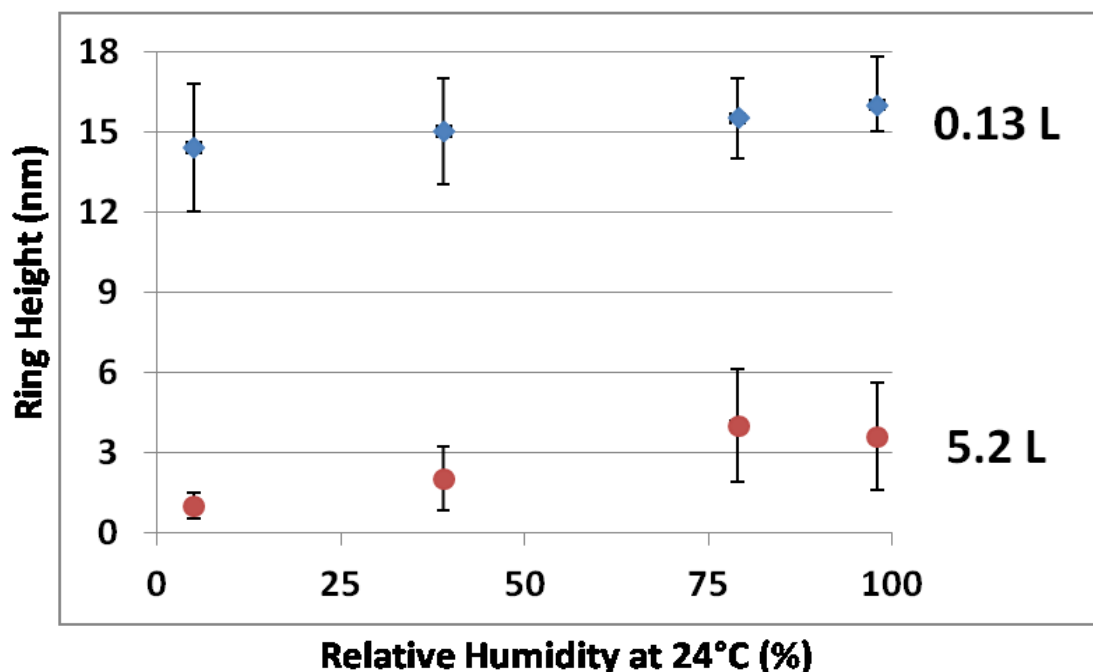


Figure 5.6 plots the nanoring height as a function of relative humidity and reactor volume at 24 °C after 90 min of reaction time with a fixed OTS liquid volume of 100  $\mu$ L. The relative humidity is varied from 5% to 39%, 79%, and 98% by  $N_2$  purge and use of saturated  $MgCl_2$ ,  $NaCl$ , and  $K_2SO_4$  solution, respectively.

Glass desiccators of volume 0.13 and 5.2 L are used as reactors. The data show that relative humidity has a weak effect on the nanopattern thickness. However, the supra-monolayer pattern only forms when the reactor volume is sufficiently small. The pattern thickness is around the monolayer thickness when the larger 5.2 L desiccator is used. The small reactor volume is necessary to maintain a sufficiently high OTS vapor pressure for bulk polymerization reaction confined to the interstitial space among the PS particles. It may be possible to make thicker nanorings by methods to maintain high OTS vapor pressure near the sample surface.

**Figure 5.6. Nanoring height variation is plotted against the relative humidity in 5.2 and 0.13 L reactors. The PS900 template is used.**



The SAMs of organosilanes including OTS on silicon substrates have been extensively studied.<sup>48,49,70,71</sup> The hydrolysis of the Si-Cl group to form the Si-OH bonds is initiated with trace amount of water. HCl is the by-product. Then the silanol group reacts with the hydroxyl group on the oxidized silicon surface by condensation. H<sub>2</sub>O is the by-product. The remaining silanol groups can either react with unbound silanol groups from neighboring OTS molecules or the hydroxyl groups on the substrate in the absence of free silanol groups to yield the monolayer structure.<sup>53,72,73</sup> The outmost methyl group makes OTS monolayer hydrophobic (contact angle  $\approx 110^\circ$ ). The close packing of OTS ( $\sim 21\text{\AA}^2/\text{molecule}$ ) could be achieved by prolonged reaction time. Alternatively, the remaining silanol groups can polymerize with the silanol groups from unattached OTS molecules to form supra-monolayers (previously referred to by others as “multilayers”).<sup>53,54,74</sup> Here we term these thicker films as supra-monolayers because there is no evidence that these films display a layered structure. Trichlorosilanes such as OTS has a tendency to polymerize among themselves.<sup>75</sup>

The supra-molecular OTS nanoring formation can be described based on silanol reactivity variation with different water structures in three zones as described in the literature.<sup>76,77</sup> Three zones of unique water structures have been identified in the particle lithographical template:<sup>76</sup> 1) cavity directly underneath the colloidal particle, 2) meniscus beyond the cavity area, and 3) free surface beyond the meniscus area. In Zone 1, ice-like water structures persist up to  $\leq 10$  nm in cavity diameter.<sup>77</sup> The ice-like water structure is characterized by anomalous changes in the density and surface tension of the water, which is attributed to the

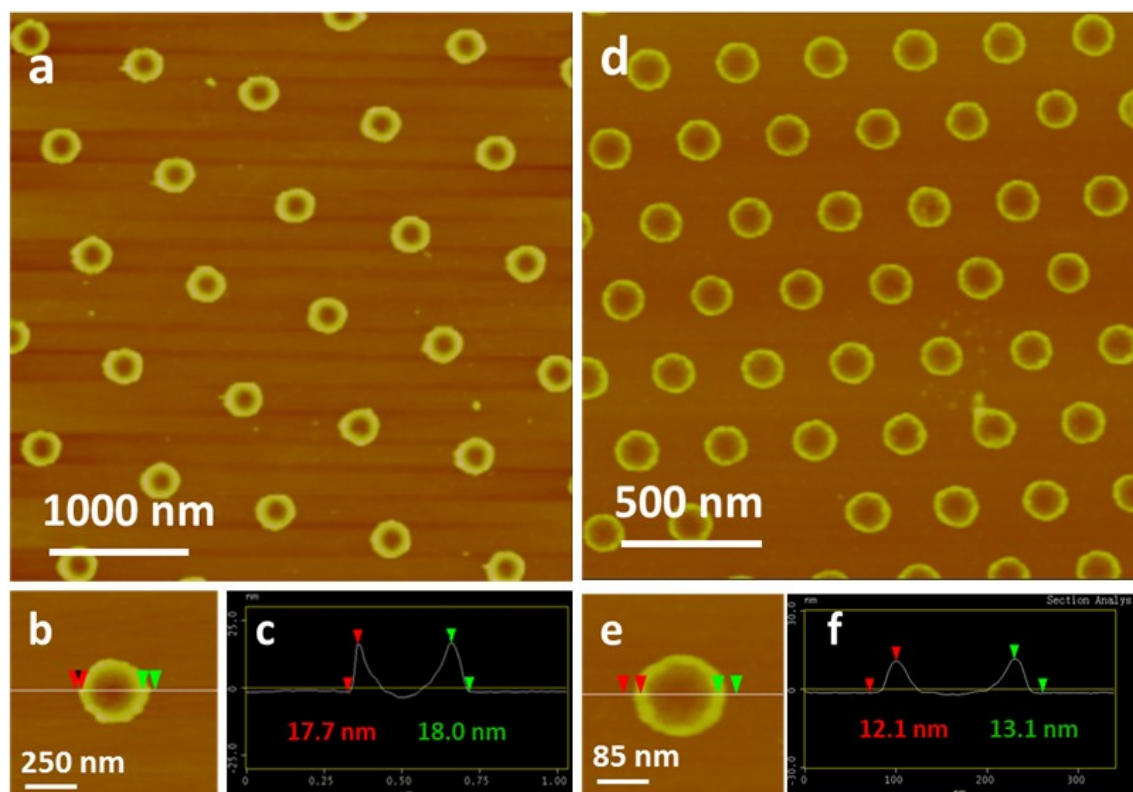


interaction of water molecules with surface hydroxyl groups on the oxidized silicon and hydrogen bond formation among water molecules.<sup>77</sup> Here the ice-like water structure is used to explain the limited reactivity of water in Zone 1. Our results of empty region with no OTS deposition fit the description of Zone 1. In Zone 1, the organosilane deposition is prevented by the steric hindrance imposed by the opposing solid substrates and surrounding liquid meniscus as well as low water reactivity. In Zone 2, water is assumed to liquefy due to capillary condensation. OTS condensation reaction with the surface hydroxyl groups occurs in the direction of the receding water contact line upon water evaporation. This yields the expected OTS monolayer pattern. However, our results show that there exists a competition between surface condensation to form the monolayer and polymerization to form the supra-monolayer in the meniscus zone. At low OTS concentration using the larger reactor volume the surface condensation dominates to yield the monolayer nanorings. At high OTS concentration using the smaller reactor volume the 3D polymerization reaction dominates to yield the supra-monolayer nanorings. Lastly in Zone 3, the free surface area is covered by planar ice-like water structures up to 3 molecular layers with or without a surface liquid layer depending on the relative humidity.<sup>78</sup> The ice-like water structure again hinders the OTS surface condensation reaction. In our case, the hydrophobic OTS nanopattern obtained only at longer reaction times is consistent with the notion that OTS surface condensation reaction occurs in Zone 3 at a slower reaction rate than that in Zone 2.

### 5.3.2. Supra-monolayer nanoring nanopattern used for organic NP deposition

Next we explore the use of the nanorings to regulate the deposition and re-crystallization of small organic molecules from the liquid phase. Three hydrophobic molecules in the crystalline powder form are used for the re-crystallization study: n-docosane, aspirin, and clarithromycin. The nanoring patterns made in 0.13 L reactor at 5% relative humidity and after 90 min reaction time on the PS900 and PS300 templates are used for NP deposition. Figure 5.7 shows the two patterns before filling them with the organic molecules. The nanorings made with the PS900 template are  $14.4 \pm 2.4$  nm in height,  $160 \pm 32$  nm in inner diameter, and  $379 \pm 46$  nm in outer diameter. The nanorings formed on the PS300 template are  $10.3 \pm 2.2$  nm in height,  $56 \pm 14$  nm in inner diameter, and  $121 \pm 25$  nm in outer diameter. The AFM images and sectional height analysis show that the nanopatterns display uniform nanostructures and the nanorings are spherical in shape. If we fill all the spherical caps to the top of the nanoring pattern we expect to create  $10^8$  NPs/cm<sup>2</sup> of uniformly distributed NPs each with a fixed volume of  $(3.0 \pm 1.5) \times 10^{-10}$  nL on the PS900 nanopattern and  $5 \times 10^8$  NPs/cm<sup>2</sup> of particle volume  $(5.0 \pm 2.0) \times 10^{-11}$  nL on the PS300 nanopattern.

**Figure 5.7. AFM height image data of the OTS nanorings made with the PS900 template (a–c) and PS300 template (d–f). Z-range = 60 nm.**

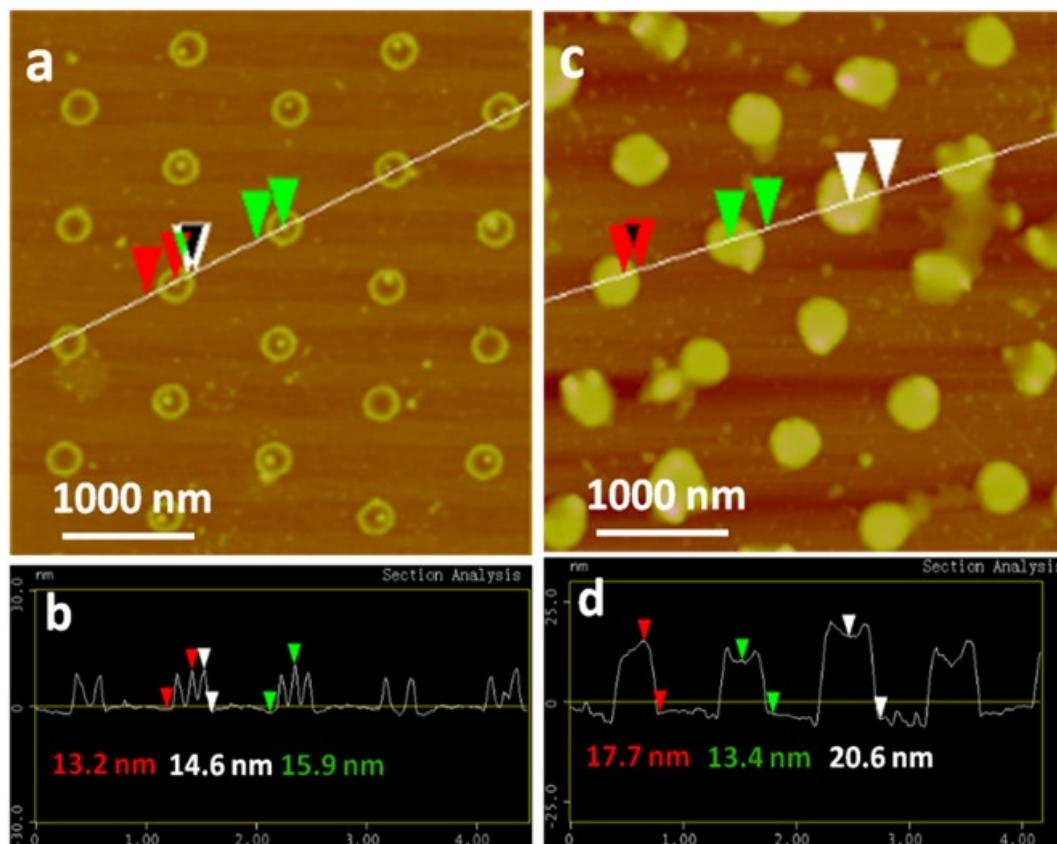


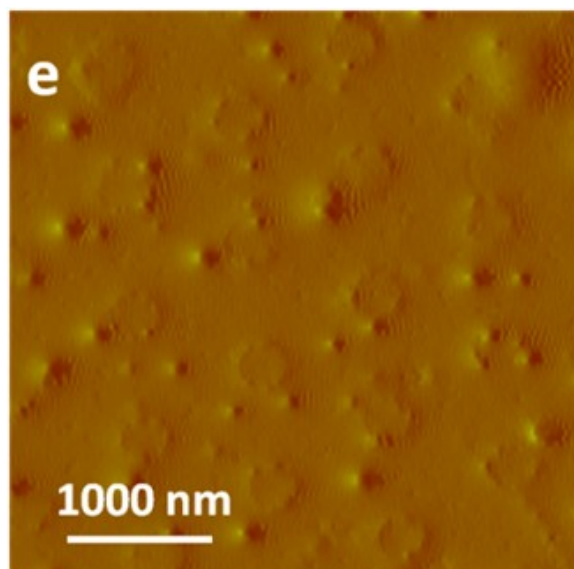
The supra-monolayer nanorings are stable against repeated solvent treatments. We have conducted AFM and contact angle measurements before and after immersing the nanopatterns in organic solvents including chloroform, diethyl ether, heptane, and 1-butanol for at least 30 min and found no evidence of pattern erosion or degradation. We have also imaged the nanopattern in 1-butanol and heptane by AFM and found no evidence of pattern swelling or degradation while immersed in the solvents. It shows that OTS molecules are polymerized to a high degree to form the nanorings.

The first compound used to fill the nanorings is n-docosane. n-Docosane is chosen as a model compound because it belongs to the n-alkane homologous series with known chain length dependent physical properties such as melting temperature and solubility. n-Docosane has a melting temperature of 43 °C. Various solvents have been used to deposit n-docosane films on the OTS nanopattern. Diethyl ether with the highest vaporization rate of all the solvents tested has been found to yield the smoothest n-docosane film. In order to ensure uniform particle formation the as-deposited film is first heated above its melting temperature to yield a uniform film thickness and then is quickly cooled to -20 °C. We have been able to produce uniform particles following this procedure as well as vary the amount of n-docosane deposited per nanoring as a function of its concentration in diethyl ether. Little n-docosane is deposited when the concentration is lower than 0.7 mM. On the other hand, the deposited layer is much thicker than the nanopattern when the concentration is higher than 7 mM. At concentrations between 0.7 and 7 mM increasing amount of n-docosane is deposited inside the nanoring with increasing concentration (Figure 5.8). n-Docosane solidifies almost exclusively inside the nanorings in a concentration range of 0.7–3.5 mM. The average NP height is 15 nm at 1 mM and reaches the maximum value of 19 nm at 3.5 mM. At 3.5 mM the n-docosane volume contained per nanoring is 5–7 times the calculated cap volume indicating that n-docosane overfills the nanoring above the nanopattern height (= 15 nm) by the simple solidification process. After reaching the maximum filling increasing amount of n-docosane is deposited outside the nanoring with increasing

concentration. The substrate is covered by a continuous layer of n-docosane at 7 mM. The uniform n-docosane NP size and distribution clearly demonstrates the ability of the OTS nanopattern to regulate molecular deposition and solidification of organic molecules and its potential use as “nano-flask” arrays for the manufacture of organic NPs and NP arrays via the simple melt solidification route.

**Figure 5.8. AFM images and sectional height analyses of n-docosane NPs deposited on the nanoring pattern (PS900) by melt solidification. The amount deposited is varied by the initial solution concentration used prior to melting of the film: 1 mM (a–b), 3.5 mM (c–d), and 7 mM (e). Z-range for (a–d) is 60 nm. Z-range for (e) is 1 V (amplitude image).**





An alternative route to melt solidification is evaporative precipitation and crystallization of organic NPs from the solution phase on the nanopattern. A 40  $\mu\text{L}$  droplet of n-docosane, aspirin, or clarithromycin of various concentrations in diethyl ether is placed on the patterned substrate followed by fast evaporation of diethyl ether. The amount deposited is a function of the solution concentration. Maximum filling of the nanoring occurs at 0.7, 3, and 0.2 mM for n-docosane, aspirin, and clarithromycin, respectively (Figure 5.9). Figure 5.10 and Figure 5.11 show the dependence of NP size on solution concentration in the PS300 and PS900 case, respectively. The corresponding particle volume versus concentration data are plotted in Figure 5.12. Figure 5.10d is an FE-SEM image of aspirin deposited on the nanopattern made with the PS300 template from 0.1 mM solution that matches closely the features from the AFM images. Both AFM and SEM images show that while the location of the NPs inside the nanorings is not fixed, a high percentage of the NPs are attached to the nanoring suggesting

that the nanoring inner wall is the preferred nucleation site for the organic molecule precipitation and crystallization.

**Figure 5.9. AFM images of n-docosane (a) and clarithromycin (b) on the PS900 substrate and aspirin on the PS900 (c) and PS300 (d) substrates at maximum nanoring filling. Z-range is 60 nm for (a–c) and 40 nm for (d).**

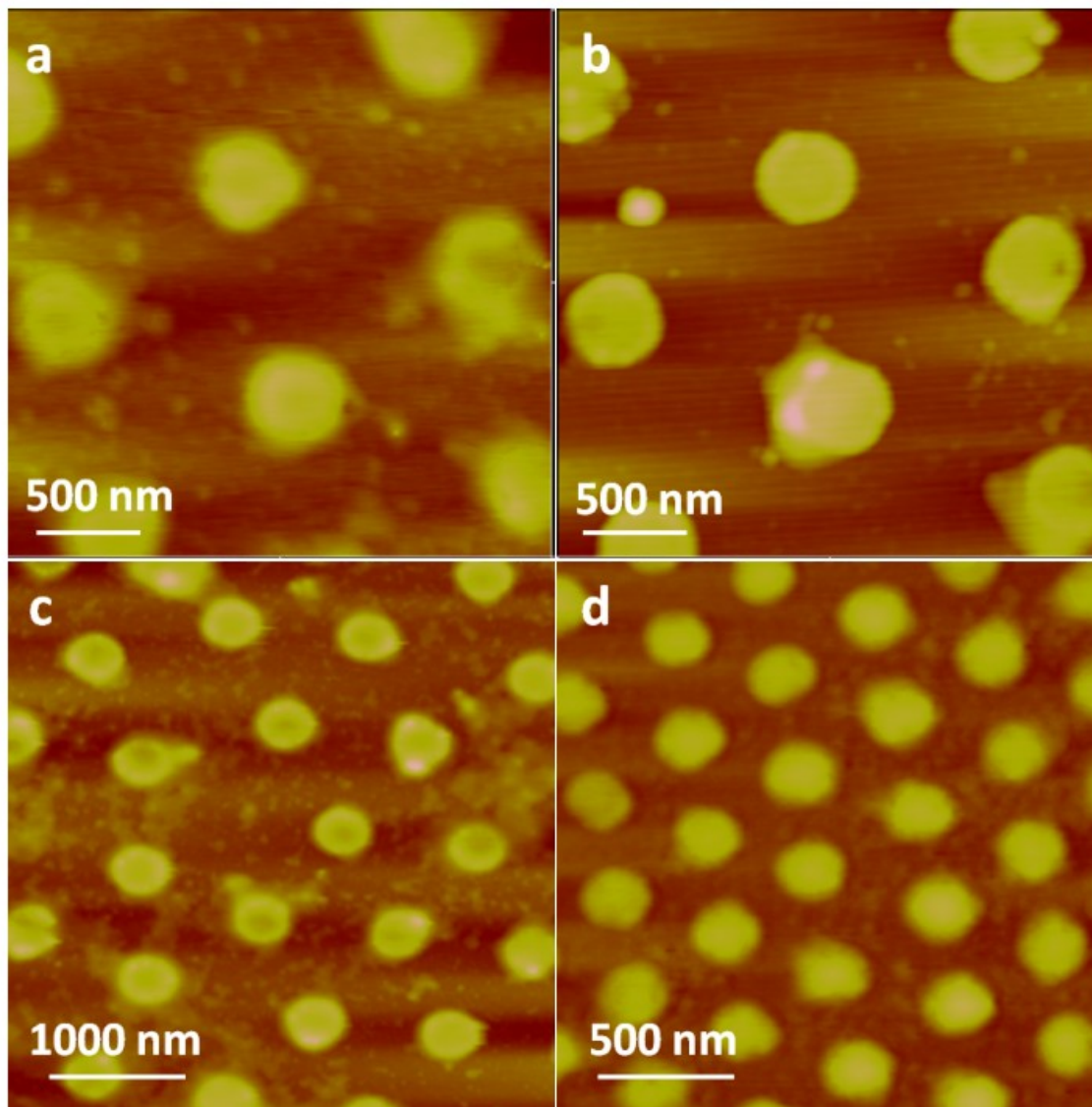


Figure 5.10. AFM images of aspirin NPs deposited on the PS300 nanopattern from 1 (a), 0.3 (b), and 0.1 mM solution (c). Z-range = 20 nm. (d)

FE-SEM image of the (c) sample.

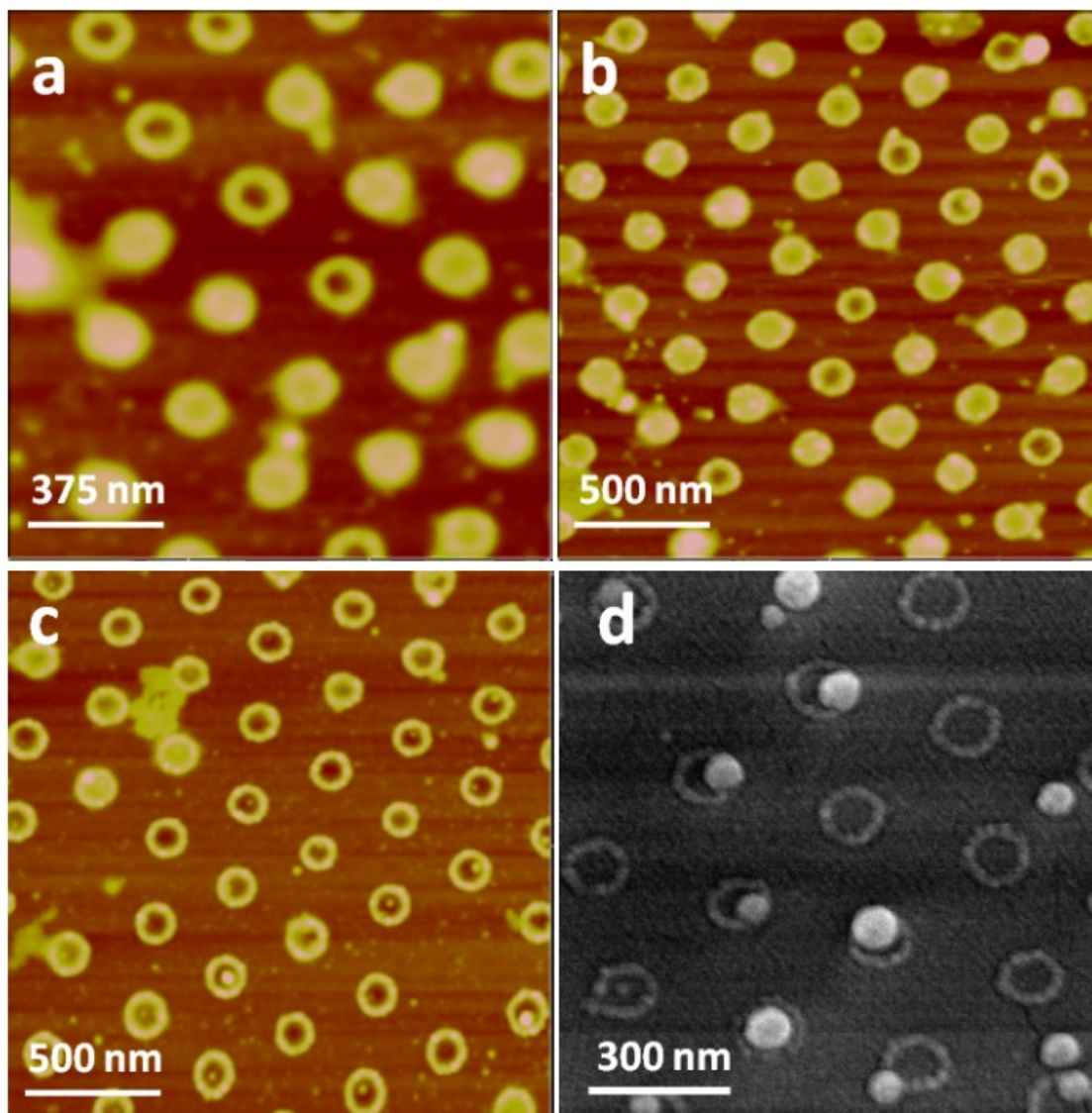




Figure 5.11. AFM images of aspirin NPs deposited on OTS nanopattern (PS900) from 1 (a), 0.3 (b), and 0.1 mM solution (c). Z-range = 60 nm.

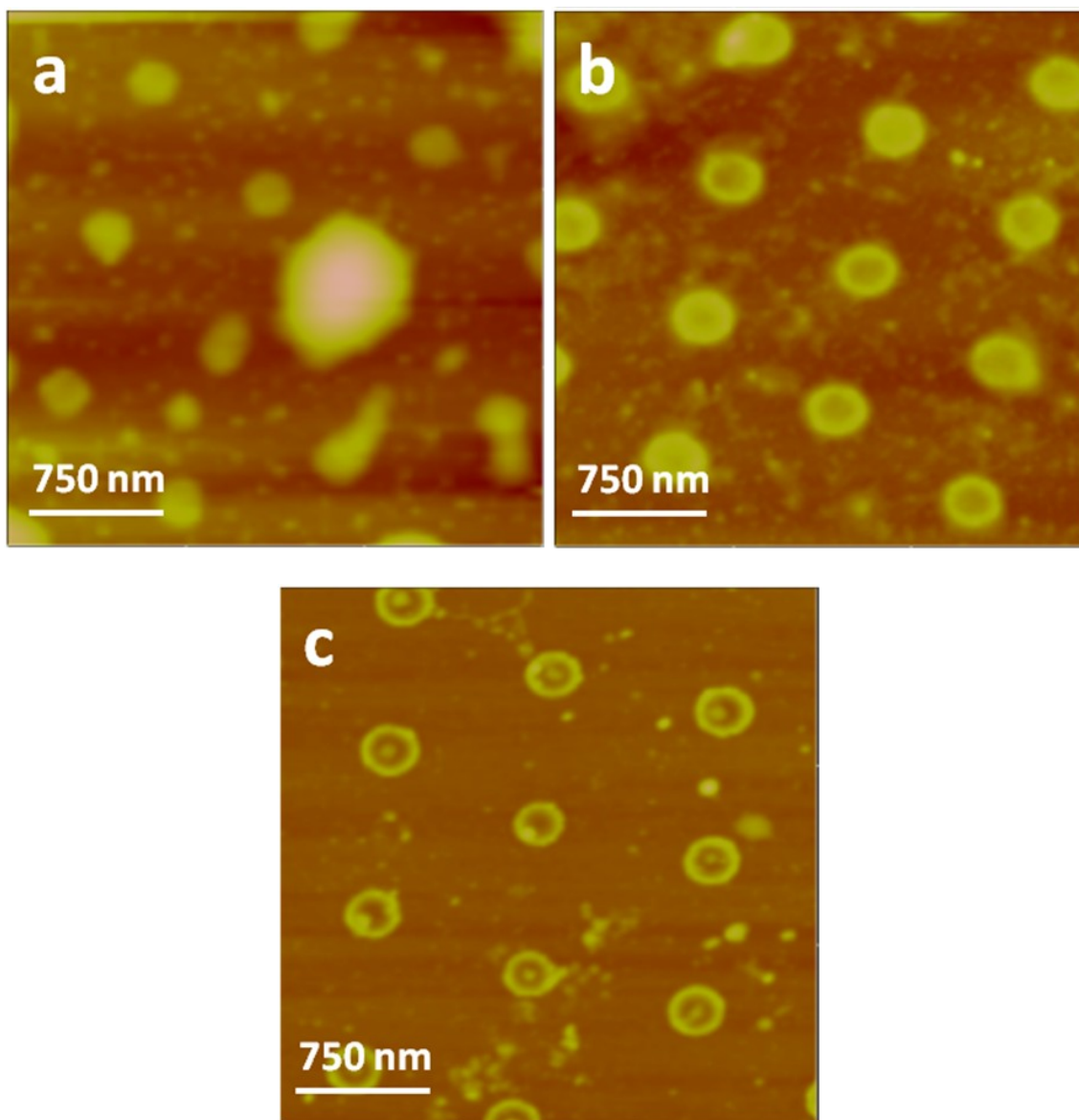
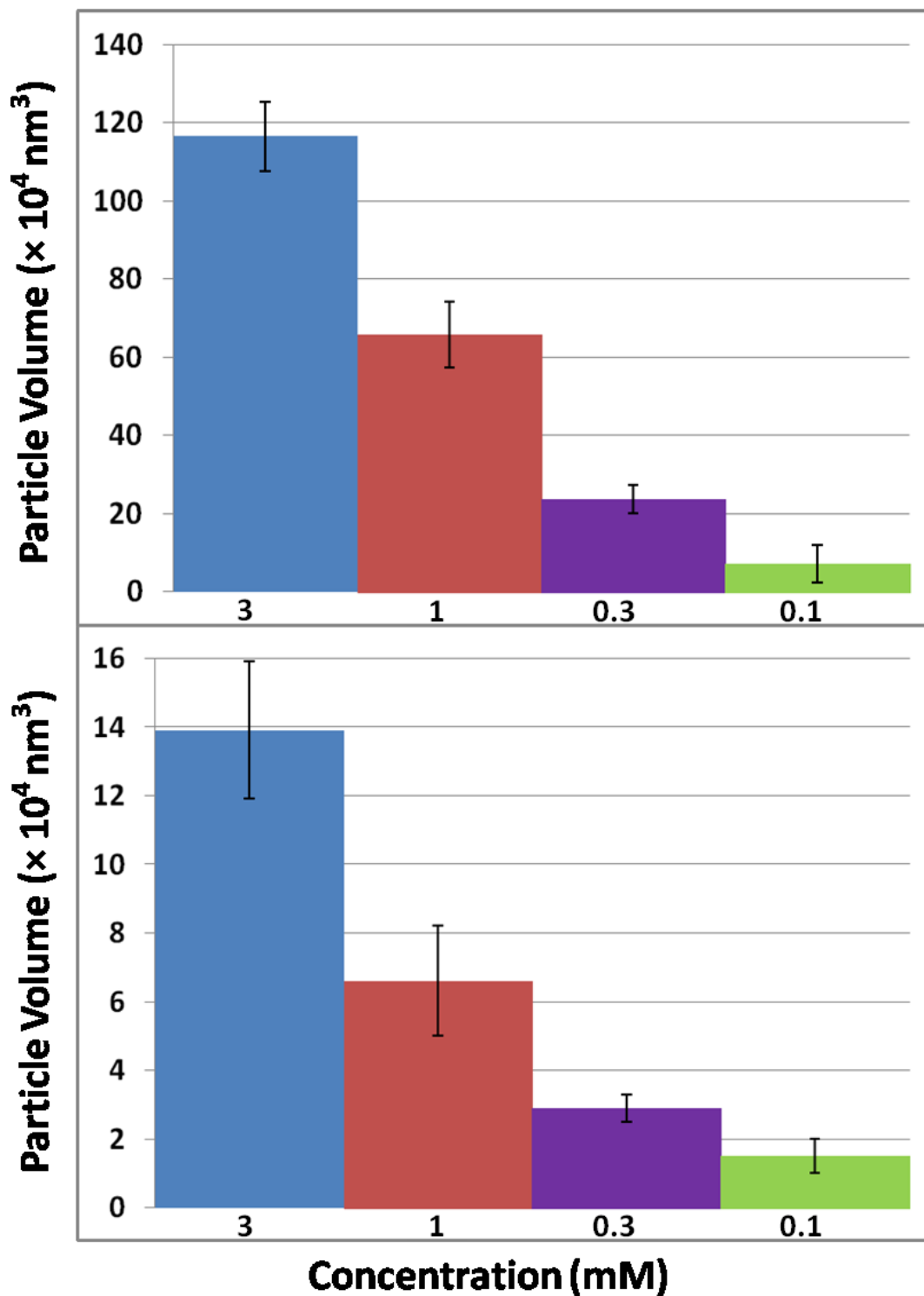


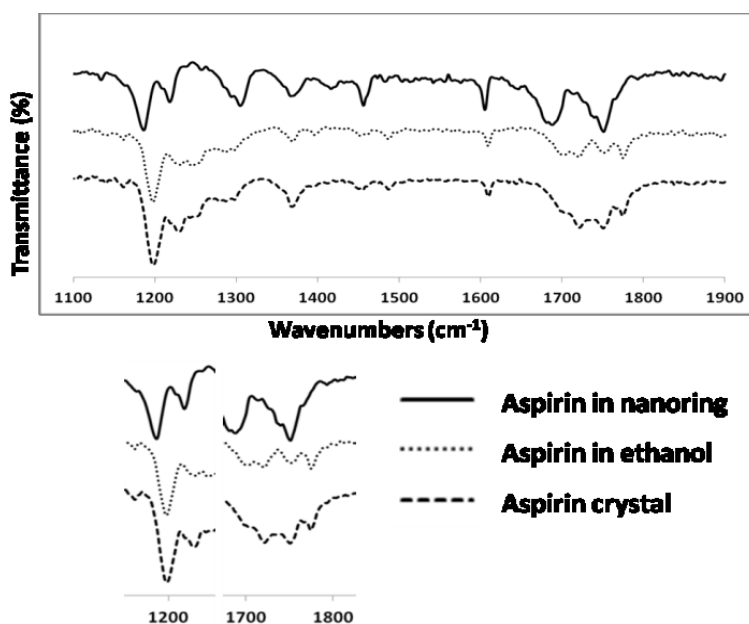
Figure 5.12. The dependence of aspirin NP volume inside the nanoring as a function of solution concentration on both PS900 (a) and PS300 (b) templates.



The molecular NP arrays can be transferred from the nanorings to another substrate such as an adhesive tape or a silicone rubber stamp by pressing the substrate against the nanopattern substrate.

What is the crystalline structure of the NPs deposited in the nanoring? While we do not have the answer for this question our preliminary FT-IR investigation suggests that aspirin NPs deposited in the nanorings are crystalline in nature. Figure 5.13 shows the FT-IR spectra of aspirin in as-purchased crystalline powder form, solution state in ethanol, and the NP form precipitated on the nanopattern, respectively. The sample at maximum filling with least deposition outside the ring is used to minimize the contribution from deposits outside the ring. The FT-IR spectrum of the aspirin NPs resembles more closely that of the crystalline powder.

**Figure 5.13. FT-IR spectra of aspirin in crystalline powder, solution, and NP forms. The y-axis has been offset for clarity.**



Precipitation and crystallization on patterned surfaces and in mesoporous and microfluidic devices are pursued as high-throughput alternatives to the traditional manual screening of protein and small molecule drug crystallization conditions because of the rapid advances in nanomedicine and genome sequencing.  $\omega$ -Terminated alkanethiol SAM micropatterns, made by micro-contact printing, have been used to study  $\text{CaCO}_3$  precipitation and crystallization.<sup>79</sup> The geometry, surface chemistry, and number of preferred nucleation sites are precisely defined by the micropattern. By making the distance between neighboring preferred nucleation sites smaller than their overlapping depletion zone calcite nucleation is confined only to the patterned area. The depletion zone is defined by the rapid molecular flux into the nucleation site that lowers the nearby concentration to below the critical nucleation concentration. In our case, rapid cooling or evaporation necessary for uniform film formation corresponds to nucleation with the smallest depletion zone. Therefore it is unlikely that the high fidelity between the NP arrays and nanoring pattern is achieved under the same mechanism as in the case of calcite nucleation on the SAM micropattern. Instead we propose that the preferential deposition of the organic molecules inside the nanoring below a certain concentration is due to the dewetting of the liquid film on the nanoring template. If the substrate were to be completely immersed in the liquid during nucleation then one would expect at least some organic molecules to deposit outside the ring at these very high solidification rates. The proposed dewetting process effectively distributes the liquid film among the “nano-flasks” so that millions of solution

experiments can be carried out in isolated droplets with droplet volume as small as  $10^{-10}$  nL on the patterned wafer substrate. When nucleation occurs in such small volumes the number of nuclei is limited due to the large depletion zone size relative to the liquid droplet size. In fact of all the nanorings examined very few of them contain more than one NP per nanoring on either the PS300 or the PS900 pattern. The uniform particle size is achieved on the nanorings by allowing only one nucleus formation per small droplet volume. Reducing liquid droplet size to the nanometer size is also effective in eliminating the dominant role of a few contaminants in nucleation studies. There is evidence that nucleation occurs at the inner wall of the nanoring likely due to the high flux at the three-phase contact line between the liquid droplet and ring inner wall perimeter.

#### **5.4. Conclusions**

This research has determined OTS CVD conditions for particle lithography using PS colloidal particles of 300 and 900 nm in diameter that yield nanorings with multilayer thickness. The OTS nanoring thickness varies between 14 and 23 nm with the maximum value obtained at the beginning of the reaction. The patterned substrate hydrophobicity can be further tuned by OTS reaction time. The supra-monolayer nanorings are stable against repeated solvent treatments, which make them suitable for use in organic solvents. The supra-monolayer nanorings have been used as “nano-flasks” to solidify NPs of small crystalline molecules including n-docosane, aspirin, and clarithromycin. The supra-monolayer OTS nanopattern has been found to be an effective template for NP

array deposition of all three chemicals with uniform particle size and spatial distribution as dictated by the OTS pattern. The particle size can be further reduced by solution concentration. The research demonstrates a particle lithographical method to manufacture supra-monolayer patterns as containers of extremely small liquid droplets and their potential use for high-throughput crystallization trials and manufacture of monodisperse organic/drug NPs. The pattern can be used for the study of nanoscale topographical and chemical features on crystal nucleation. The combination of small particle size and even spatial distribution could offer a means to formulate low-dose drug delivery devices with precise dosage control.

## CHAPTER 6

### GNP SYNTHESIS, CHARACTERIZATION, AND INTERACTION WITH MACROPHAGE FOR IMMUNE MODULATION

#### 6.1. Introduction

The overall goal of the project is to use GNP based materials to modulate immune responses by targeting immune cells. The specific aim of the current research is to establish a baseline of macrophage cell uptake and cytokine expression of GNPs of sizes 5, 15, 40, and 65 nm. In this first period, we have synthesized the GNPs, tested different centrifugation procedures for optimal purification of the GNPs, characterized the GNPs using a variety of physical characterization methods, and obtained preliminary results on cell uptake and cytokine expression. For the next aim, we propose to select a NP size with the highest cellular uptake and lowest inflammatory response as a delivery vehicle for anti-inflammatory molecules targeted to macrophage cells.

#### 6.2. Experimental

**Materials.** The following chemicals have been used as received: tetrachloroauric (III) acid trihydrate ( $\geq 99.9\%$  trace metals basis, Aldrich), sodium citrate tribasic dihydrate ( $\geq 99.0\%$ , Sigma-Aldrich), MSA (97%, Aldrich), sodium borohydride ( $\geq 99\%$ , Fluka), methanol ( $\geq 99.8\%$ , EMD), hydrochloric acid (36.5-38.0% assay, EMD), and nitric acid (68-70% assay, Mallinckrodt). Deionized water from the Barnstead Nanopure water purification system (resistivity 18

M $\Omega$ ·cm) was used. All the glassware was treated by aqua regia (3:1 volume ratio of HCl and HNO<sub>3</sub>) and comprehensively rinsed by deionized water before reactions.

**Synthesis and capping of the GNPs.** Citrate-terminated GNPs of diameter range 15 (GNP15), 40 (GNP40), and 65 nm (GNP65) are synthesized by varying the gold salt (HAuCl<sub>4</sub>) to sodium citrate molar ratio.<sup>8,10,80,81</sup> Due to the large amount of GNPs needed for the biological study, we modified the literature method to scale up the synthesis. In a typical reaction, 500 mL of 0.01% w/v HAuCl<sub>4</sub> aqueous solution is heated to boiling. An aqueous solution of 17.5 mL (GNP15), 5 mL (GNP40), or 3 mL (GNP65) 1% w/v sodium citrate is added to the HAuCl<sub>4</sub> solution while stirring. The solution changes first to a gray color, and then to a red color in 3 min. The solution is then cooled to room temperature. Different centrifugation conditions are applied for efficient GNP purification (see Results). The successfully purified GNPs are redispersed in a pH=7 citrate buffer, then applied to the THP-1 cells and cultured overnight.

GNPs of diameter 5 nm (GNP5), capped with the MSA ligand, are synthesized<sup>17</sup> by slowly adding sodium borohydride (NaBH<sub>4</sub>) aqueous solution (0.2 M, 25 mL) to the reaction mixture of HAuCl<sub>4</sub> (0.125 M, 4 mL in deionized water) and MSA (5 mM, 100 mL in methanol). The resulting MSA-GNP is centrifuged (10000 rpm, 5 min at room temperature) and washed by 20% (v/v) water/methanol twice and pure methanol once, then vacuum-dried into a black powder.



**Characterization of the synthesized GNPs.** UV-Vis absorption spectroscopy (Varian Cary 50) is used to determine GNP size and solution concentration based on the Beer-Lambert law.

TEM (JEOL JEM-2010) is used to determine the size distribution of the GNPs' metal core. Samples are prepared by placing a droplet of the GNP solution on Formvar-coated copper TEM grids. After 5 min, excess liquid is removed and the remaining thin liquid layer is allowed to dry in air. TEM imaging is conducted in the bright field mode operating at an accelerating voltage of 200 keV. The particle size analysis is conducted by averaging data manually measured over 50 individual particles by the ImageJ software.

Dynamic light scattering (DLS) and zeta potential of the GNPs are measured using a Malvern Nano-ZS. DLS samples are prepared by diluting the GNP after its purification into 50 µg/mL aqueous solution. 1250 µL of the solution is transferred to a 5.0 mL PS cuvette. The Z-average hydrodynamic diameter (HD), polydispersity index (PDI), and zeta potential are measured in pH=7 citrate buffer and temperature of 25°C. The refractive index of the particles is set to 1.5. Each final measurement is ten 2 min measurements averaged together.

**Cell culture.** Approximately  $1 \times 10^5$  THP-1 cells are treated for 72 h with 200 nM of phorbol 12-myristate 13-acetate (PMA) and are allowed to recover for an additional 72 h in PMA-free media before exposure to the GNPs. Adherent macrophage-like THP-1 cells are exposed overnight to 0 µg/mL, 1 µg/mL, 5 µg/mL, or 10 µg/mL of the GNPs. Lipopolysaccharide (LPS) of varying concentrations (0 ng/mL, 1 ng/mL, 10 ng/mL, 100 ng/mL, 500 ng/mL, and 1000

ng/mL) are used as control. The fixed cells are treated with GoldEnhance LM/Blot (Nanoprobes, Yaphank, NY) to increase the NP size so as to be visible by light microscopy.

**Cellular uptake of the GNPs by inductively coupled plasma mass spectroscopy (ICP-MS).** ICP-MS (Perkin Elmer NexION 300D) is used to determine gold uptake by cells. Samples (cell pellet at centrifuge tube bottom) are digested in 500  $\mu$ L of nitric acid and 1500  $\mu$ L hydrochloric acid for 60 min in 90°C water bath, then diluted into deionized water to make 15 mL solution.

**RNA extraction and real-time reverse-transcription polymerase chain reaction (RT-PCR) analysis.** THP-1 cells are seeded at a density of  $1 \times 10^5$  cells/well of 24-well plates and grown overnight. The cells are treated with different concentrations of the GNPs overnight. Bacterial LPS (100 nM) treated cells serve as a positive control. A matrix has been established so that every GNP concentration is paired with every LPS concentration. Following this paradigm, GNPs and LPS are added to the cultures at the same time and cultured for approximately 18 h. After the treatment period, culture media is removed from the wells and placed into labeled tubes. After removal of the culture media, lysis buffer is immediately added to each well in preparation for total RNA extraction. The concentrations of IL-6, and IL-10 are measured in the culture media by enzyme-linked immunosorbent assay (ELISA). Changes in the relative amounts of mRNA for these three cytokines are determined using TaqMan qPCR assays.

### 6.3. Results and discussion

#### 6.3.1. Purification of the synthesized GNP solution

To remove the unreacted reagents with a maximal recovery of the GNPs, the centrifugation process, that is, centrifugation force and time, needs to be optimized for various GNP sizes. Figure 6.1 shows the GNPs at different stages of purification. The concentration and degree of GNP recovery is determined by UV-Vis spectroscopy according to the Beer-Lambert law. UV-Vis spectroscopy is used to determine GNP solution concentration because GNPs scatter and adsorb light in the visible wavelength range due to its surface plasmonic behavior. Figure 6.2 shows the UV-Vis spectra before and after centrifugation purification of GNP15, GNP40, and GNP65. The peak position could be used to monitor citrate-GNPs diameter approximately following the equation:  $d = [\ln[(\lambda_{spr} - 512)/6.53]] / 0.0216$ .<sup>30</sup> It shows that the recovery efficiency is a function of the centrifugal force and GNP size. The efficiency decreases with increasing GNP size.

**Figure 6.1. GNPs before and after 20 minute centrifugation at various relative centrifugal forces (rcf). The first column lists the rcf. The second column shows the original suspensions (top) and GNPs resuspended (vortexed) after centrifugation. The third column shows the residual hard pellet formed in the tubes containing GNP40 and GNP65 (the one labeled 50 nm is measured to be 40 nm in size and the one labeled 70 nm is measured to be 65 nm in size).**

### Original Suspensions

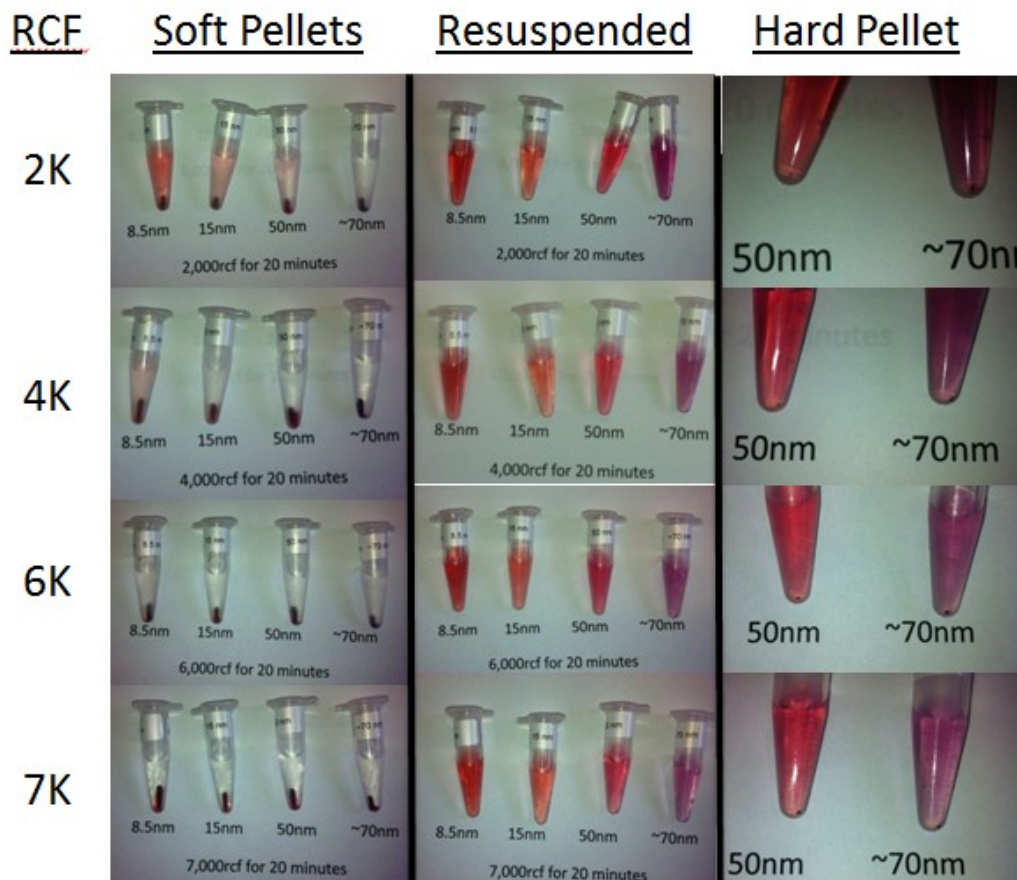
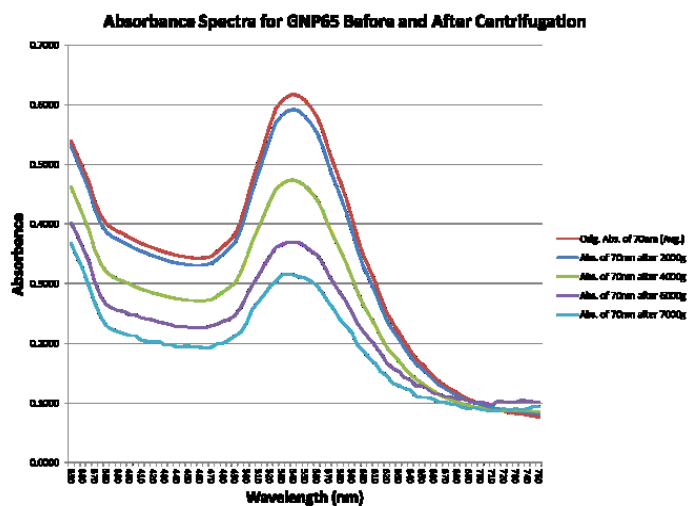
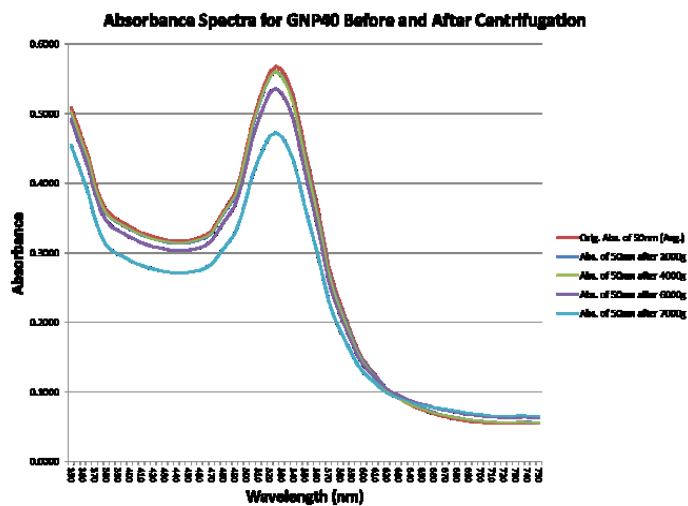
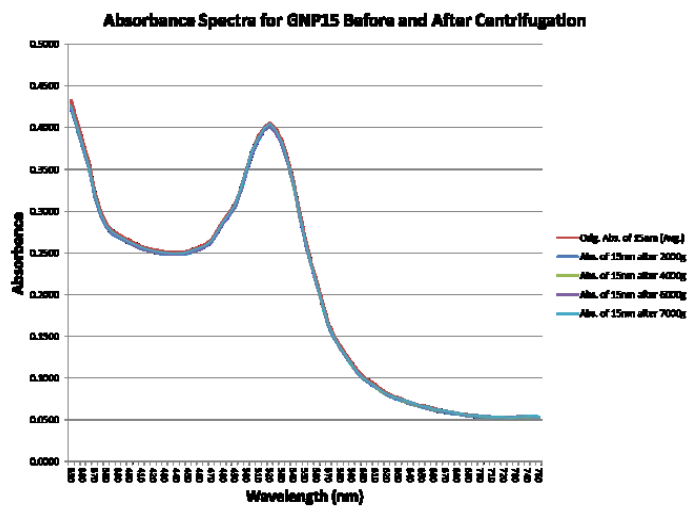


Figure 6.2. UV-Vis spectra of GNP solutions before and after centrifugation.



According to literature, we can estimate the extinction coefficient ( $\epsilon$ ) for different diameter ( $D$ ) of citrate capped GNPs by equation  $\ln(\epsilon) = 3.32 * \ln(D) + 10.8$ .<sup>82</sup> Then we can plot  $\epsilon$  into Beer's Law ( $A = \epsilon bc$ ,  $b$  is path length 1 cm and  $c$  is absolute gold concentration) to calculate  $c$  from GNP solution's UV-Vis absorbance  $A$ . For instance, 15 nm cit-GNP has  $\epsilon = 3.94 * 10^8 \text{ M}^{-1}\text{cm}^{-1}$  so  $A = 0.995$  will result in  $c = 2.53 * 10^{-9} \text{ M}$ , which times 15 nm GNP's molecular weight ( $2.05 * 10^7 \text{ g/mol}$ ), to get weight concentration of 52  $\mu\text{g/mL}$ . By this means, we can get any citrate-GNP's weight concentration once we know its average particle size and absorbance from UV-Vis.

### 6.3.2. Physical characterization of the GNPs

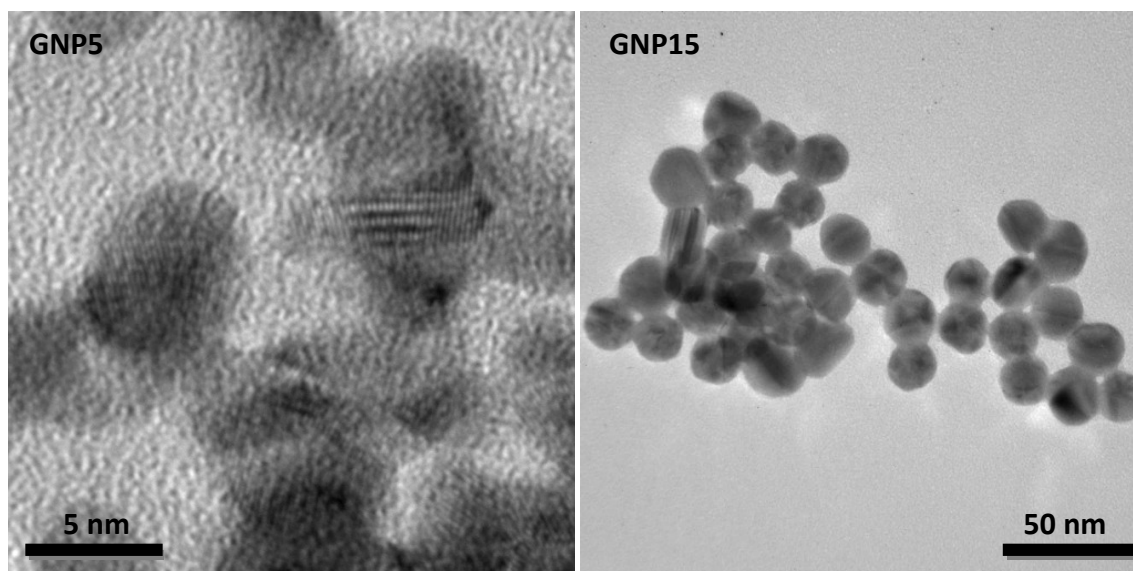
The GNPs are characterized by TEM and DLS (Table 6.1). The size measurements from TEM and DLS are in good agreement with each other except for GNP65. In the case of the smallest 5 nm GNPs, DLS cannot be used because of the detection limit. In the case of the largest particles, GNP65, the size measured by DLS is smaller than that by TEM. This could be due to the increased anisotropy of GNP65 and data fitting of the DLS measurements, which does not take into account the non-spherical shape. Figure 6.3 shows representative TEM images of GNP5, GNP15, GNP40, and GNP65. As the particle size increases, GNPs change from monodisperse spheres to faceted particles with non-spherical shapes. The NIH ImageJ software was used to analyze the sphericity of the particles ( $N \approx 50$ ) by measuring the area ( $A$ ) and perimeter ( $P$ ) of each particle. The average circularity of the GNPs,  $F$  ( $F = 1$  for a

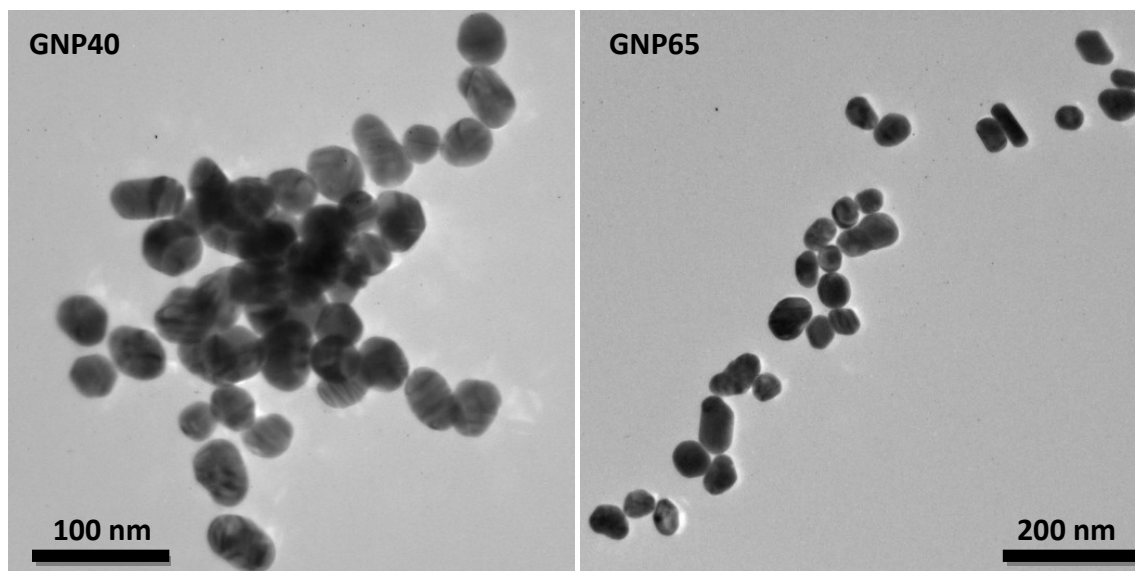
perfect circle), was calculated by equation  $F = 4\pi A/P^2$  and also listed in Table 6.1. The zeta potential data showed that the GNP surface is highly charged, which is consistent with their high dispersion stability in aqueous media.

**Table 6.1. DLS measured size and zeta potential for all 4 kinds of GNPs, size are comparable with TEM analysis.**

| Name  | Size<br>(TEM, nm) | Sphericity<br>(TEM) | Size<br>(zetasizer, nm) | Zeta potential<br>(zetasizer, mV) |
|-------|-------------------|---------------------|-------------------------|-----------------------------------|
| GNP5  | 5.0±0.8           | 0.99                | Below limit             | -50.6                             |
| GNP15 | 15.2±1.4          | 0.98                | 12.4                    | -37.0                             |
| GNP40 | 40.0±2.3          | 0.93                | 38.8                    | -47.6                             |
| GNP65 | 63.6±3.6          | 0.85                | 48.0                    | -40.2                             |

**Figure 6.3. TEM images of synthesized GNPs of different sizes.**



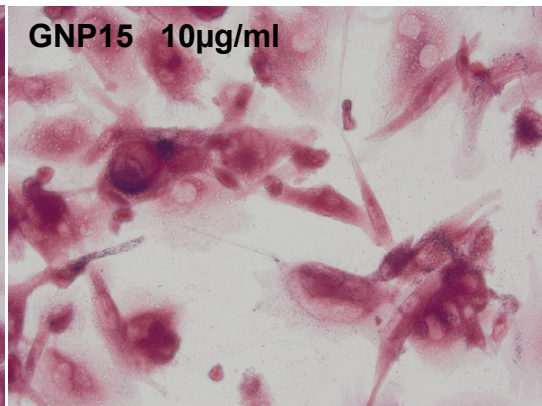
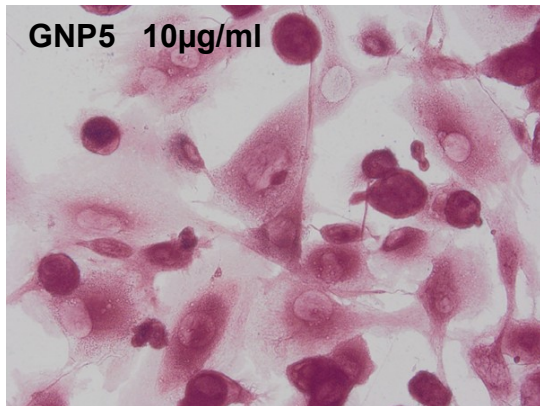
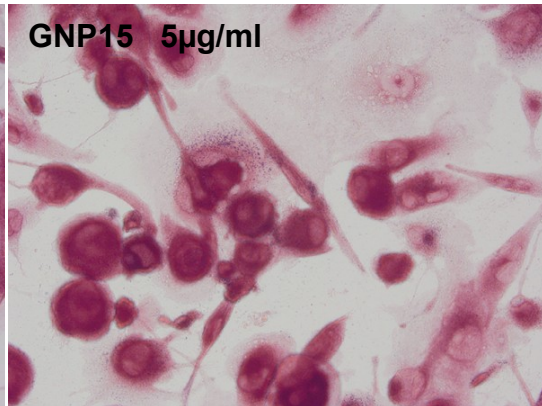
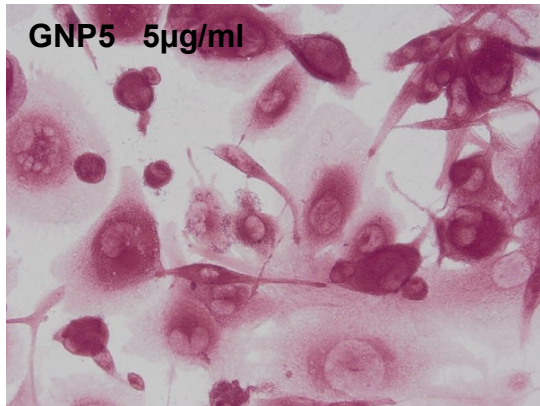
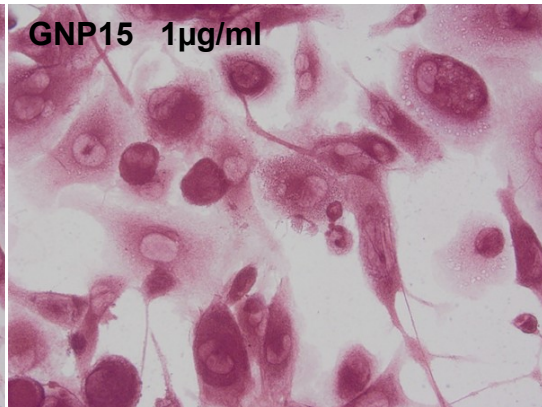
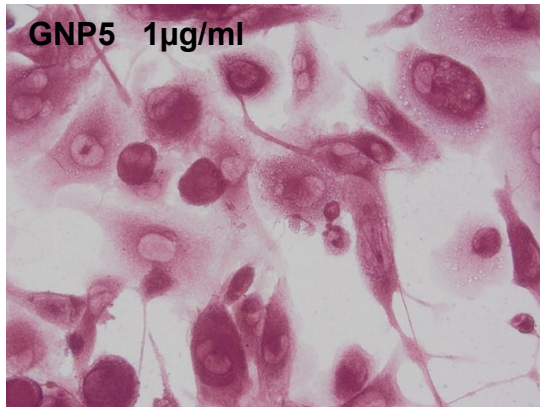
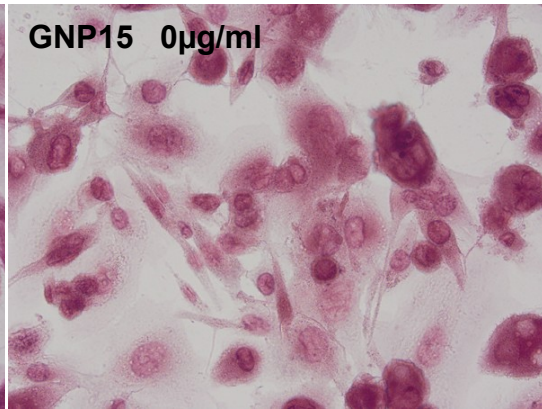
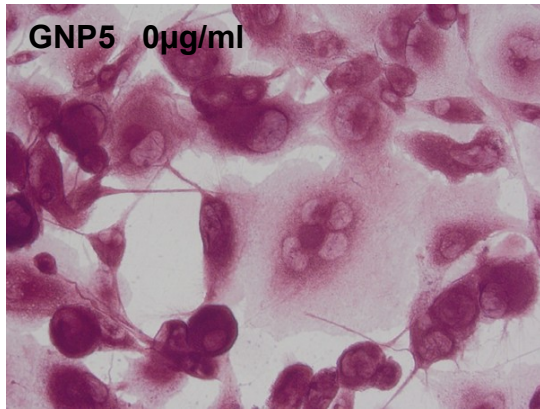


### 6.3.3. THP-1 cell uptake and response to the GNPs

The GNPs of all sizes are taken up by the THP-1 cells (Figure 6.4). The images show that as GNP concentration increases, the uptake also increases. Cytokines are measured in the culture media using the existing stock of previously purchased ELISA kits. The cytokines measured are IL-10 and IL-6. For both IL-10 and IL-6 the amount of cytokine in the culture media following incubation with 1  $\mu\text{g}/\text{mL}$  of GNP15 is similar to the control conditions of (a) no treatment, (b) deionized  $\text{H}_2\text{O}$ , and (c) GNP supernatant (0.05 mM citrate solution). There is a slight increase in IL-10 and IL-6 concentrations following exposure to 5  $\mu\text{g}/\text{mL}$  of GNP15. There is approximately a 4-fold increase in IL-10 and IL-6 concentrations following exposure to 10  $\mu\text{g}/\text{mL}$  of GNP15 (Figure 6.5).

**Figure 6.4. Light microscopy images of THP-1 cells treated with 0, 1, 5, and 10  $\mu\text{g}/\text{mL}$  GNP5, GNP15, GNP40, and GNP65, respectively.**





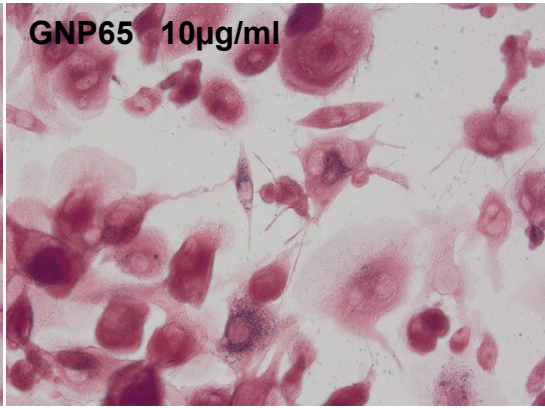
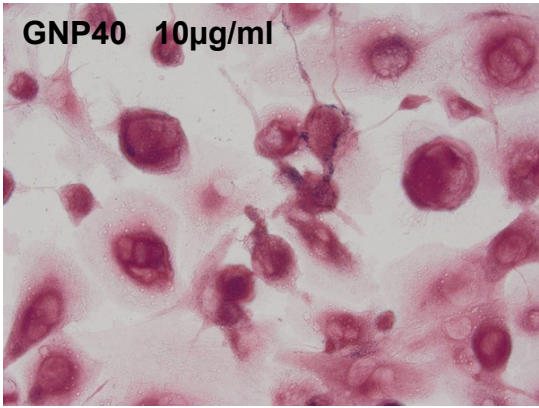
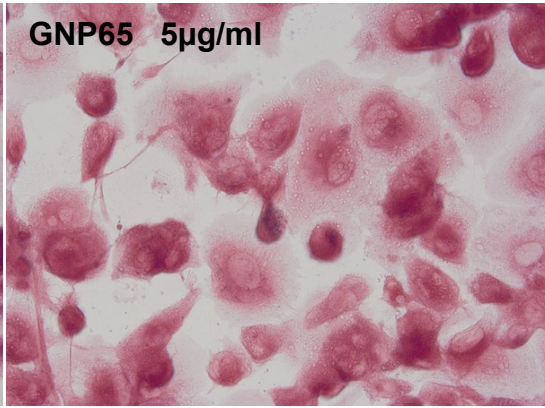
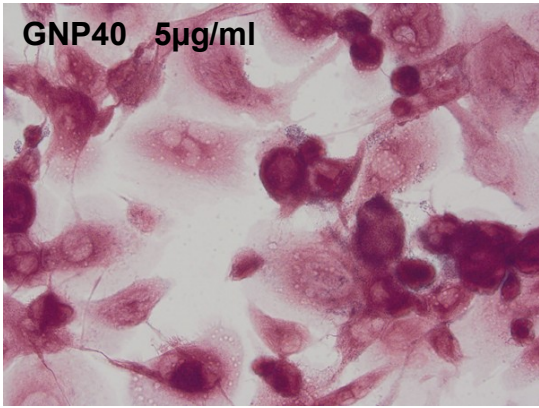
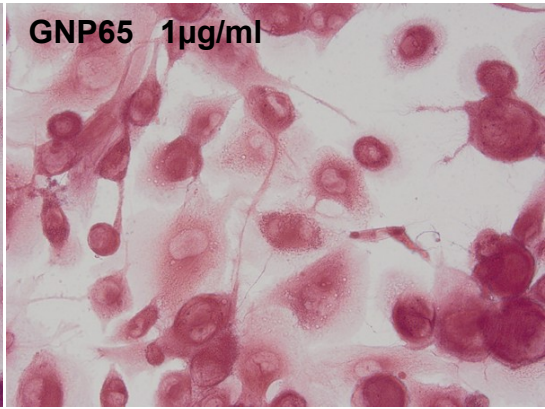
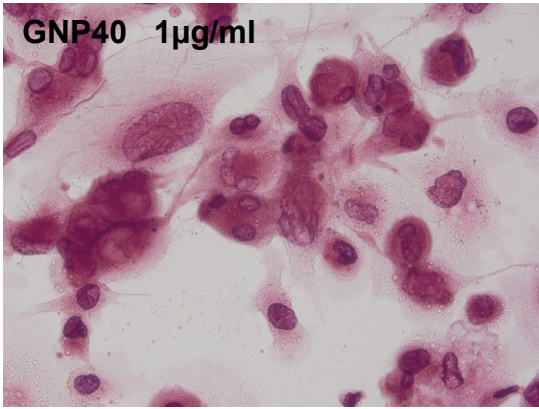
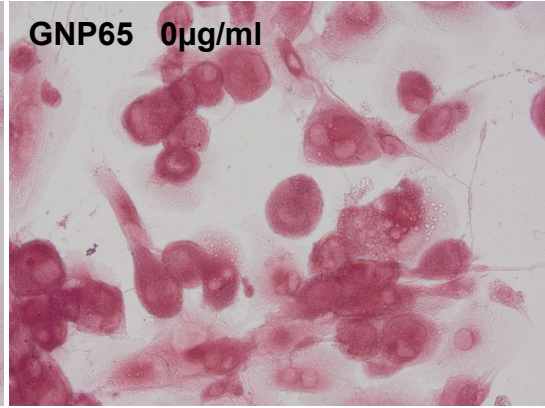
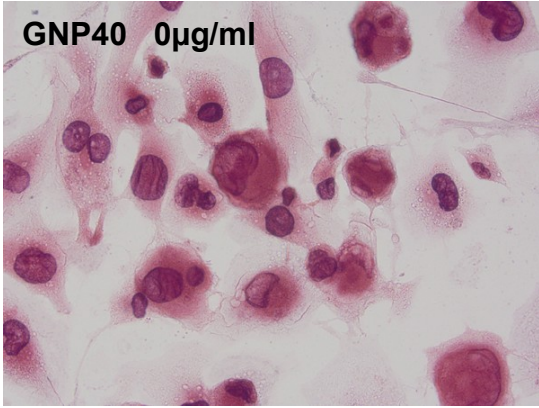
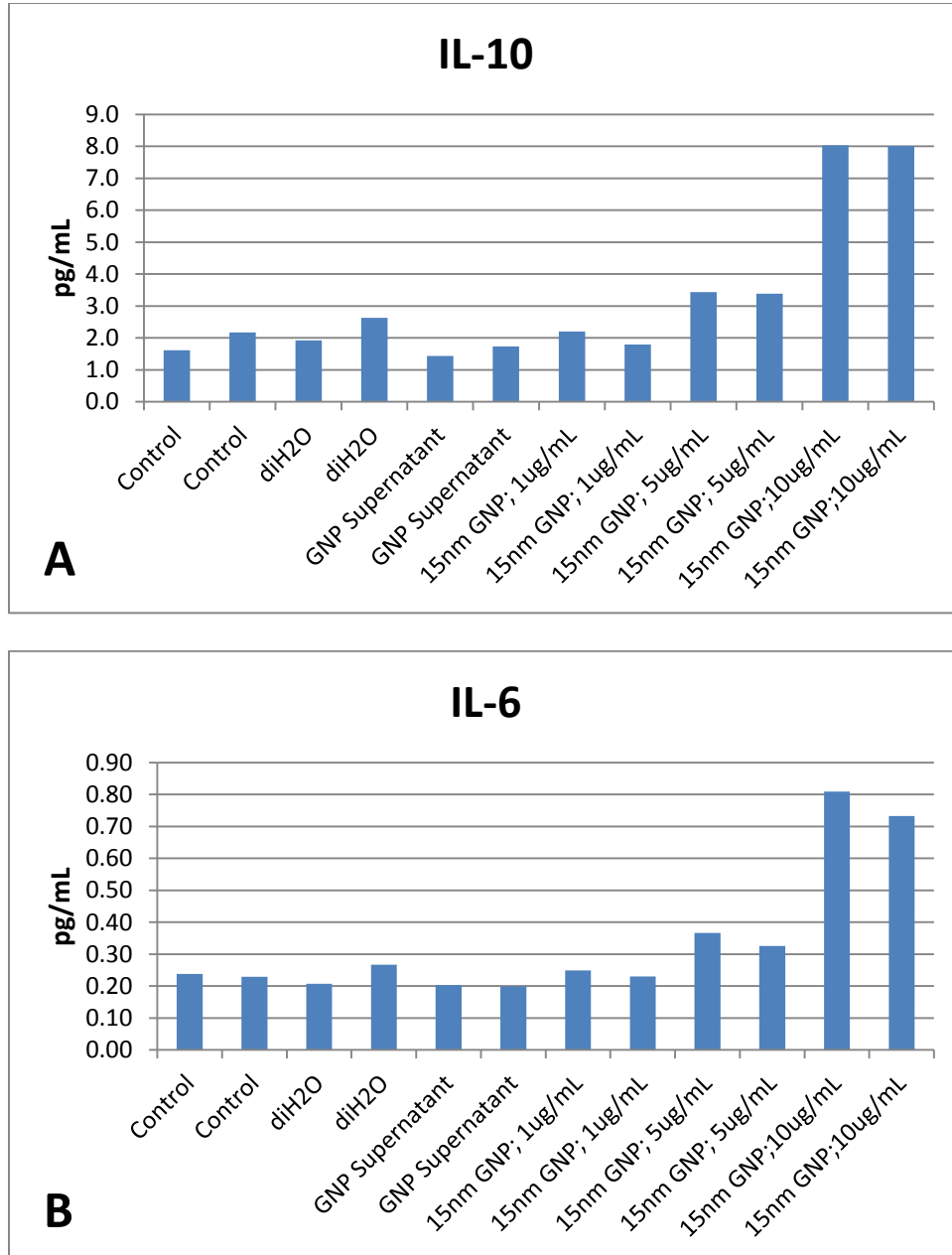
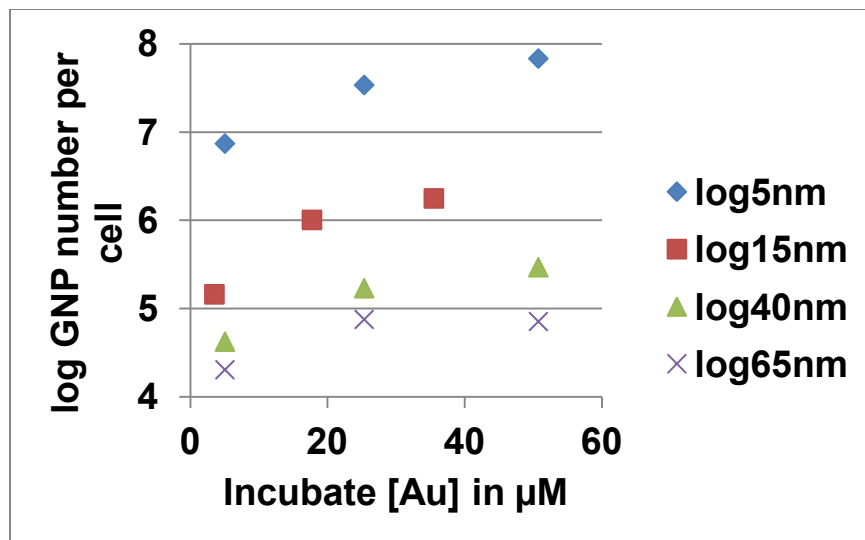
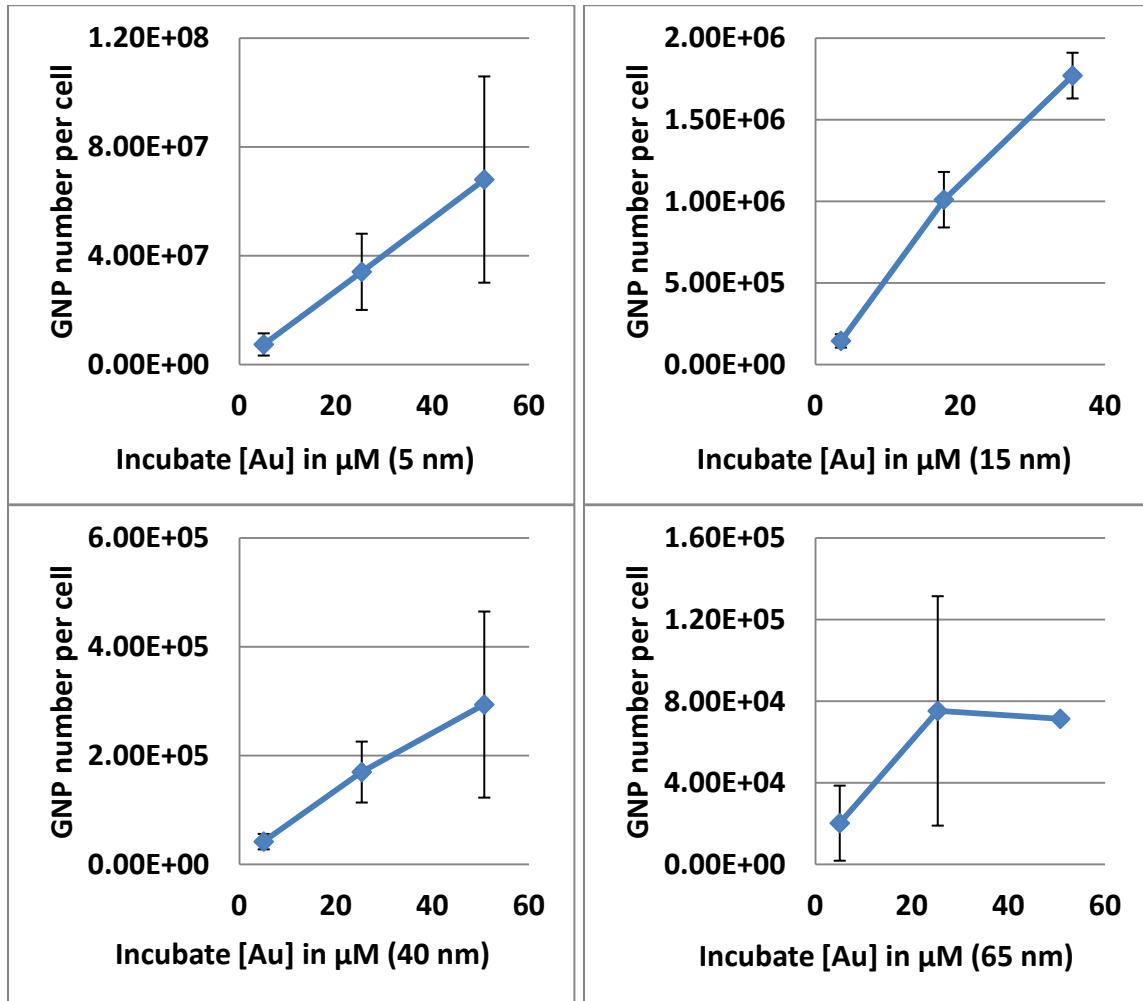


**Figure 6.5. IL-10 and IL-6 measured by ELISA in culture media of THP-1 cells exposed to purified and concentrated GNP15. (A) IL-10 concentrations after overnight exposure to control conditions and GNP15 at 1, 5, and 10 ug/mL. (B) IL-6 concentrations after overnight exposure to control conditions and GNP15 at 1, 5, and 10 ug/mL.**



In order to quantitatively determine the amount of GNPs taken up per cell, we conducted ICP-MS measurements.<sup>83,84</sup> ICP-MS determines the elemental gold concentration per cell with the highest precision with the detection limit of 1 ppb. We used the following equations to convert the number of Gold atoms to number of GNPs from the ICP-MS measurements. For a sphere of diameter  $D$ , the number of atoms ( $N_{Au}$ ) could be calculated by  $N_{Au} = \pi D^3 / 6 / v_{Au}$ , where  $v_{Au}$  refers to the volume of one single Gold atom,  $17 \text{ \AA}^3$ .  $N$  is the measured total Gold atom number from ICP-MS. Therefore the GNP number could be calculated as  $N_{GNP} = N / N_{Au}$ , and the average GNP per cell equals to  $N_{GNP} / N_{cell}$  ( $N_{cell}$  is estimated from microscope image by manually counting). Figure 6.6 shows the average GNP number per cell for 4 different sizes versus initial incubation gold concentration (estimated from UV-Vis absorbance).

Figure 6.6. ICP-MS results for 4 sizes GNP incubation at different concentrations with THP-1 cells.



As incubate [Au] increases, cell uptake increases linearly approximately for all 4 sizes of GNPs (GNP65's last data point does not contain error bar due to the sample limitation). However this system shows almost 10 folds higher uptake than the literature studies (e.g. GNP15). In addition, the cytokine is still quite low, which means GNP could be a good candidate for medical purpose researches, such as drug delivery.

#### **6.4. Conclusions**

This research has investigated the immune response of macrophages (THP-1 cell) to four sizes (5, 15, 40, and 65 nm) of GNPs with citrate ion or MSA as the capping ligand. Centrifugation-redispersion based purification method for citrate-GNP colloidal has been demonstrated by varying time, speed, and redispersion media. The calibration curve for GNP solution concentration based on UV-Vis absorbance has been plotted and other physical characterizations results are obtained with respect to GNP's size, shape, and surface potential. All GNPs have shown high uptake when incubating with THP-1 cells with low cytotoxicity. Low cytokine (IL-10 and IL-6) is also measured by ELISA kits, showing mild immune responses of macrophages to these GNPs.

## CHAPTER 7

### CONCLUSIONS AND RECOMMENDATIONS FOR FUTURE WORK

#### 7.1. Conclusions

In this dissertation, we first generally introduced three topics from the literatures' perspective, including nanohybrids fabrication with SMN, GNPs synthesis and characterizations, and nanopatterns generation for high throughput screening. Secondly, several characterizing instruments including AFM, TEM, TGA, X-ray and so on were discussed with respect of this dissertation. Last but not least, three research projects have been covered to illustrate nanoconfinement's role in nanocrystallization as well as GNPs uptake by macrophage cells.

Molecular crystallization under nanoconfinement is studied on convex (nanoparticle) and concave (nanoflask) surfaces. Shape-confined molecular nanorods nucleate on GNP seeds. Effects of NP size, surface chemistry, and crystalline molecular size have been investigated. New concepts of seed-mediated nanorod growth are applicable to diverse organic nanorod/nanowire manufacture. Molecular nanocrystal arrays are deposited on OTS nanopatterns. Formation mechanism of SMR nanopatterns has been investigated. Drug NPs of uniform size/distribution have been produced on the nanopattern. This new concept is applicable to manufacture of organic NP arrays.

The overall conclusion is that the self-assembled method for fabricating nanohybrids based on SMN was a success. The novel "nano-flasks" used for

nanoconfining drug crystals could be potentially used in high throughput screening.

## **7.2. Recommendations for future work**

In the first project methyl-terminated GNPs have been used to nucleate fatty acid nanorods by spin coating method, which seems to be an uncontrollable way for generating nanohybrids. One possibility to modify the current methodology could be making randomly GNP anchored substrates before spin coating fatty acids. Another aspect that could be addressed is that fatty acid could be replaced by conductive or other functionalized organic molecules to form more unique nanohybrids, which will facilitate this system to be used in electronic device or sensor applications. Also we can generate GNP array patterns for nucleating nanorods to fabricate hybrid network architectures.

For second project, one potential future work could be using PDMS elastomers as the stamp to harvest drug nanocrystal patterns for medical usage to fully realize high throughput screening. Also more kinds of drug molecules, including hydrophilic ones, could be tested to further confirm the universality of this methodology. However hydrophilic molecules may require other organosilane's nanopatterns due to specific bonding scenario. The third point would be to use SMR to contain other nanomaterials such as GNPs or protein molecules.

Finally for the last project, shape and surface chemistry effect of GNPs on cell uptake and immunogenicity can be further investigated.



**APPENDIX**

1. Gerard, H. C.; Mishra, M. K.; Mao, G.; **Wang, S.**; Kannan, R. M.; Hudson, A. P. Dendrimer-enabled DNA delivery and transformation of *Chlamydia pneumoniae*, **Nanomedicine**, in press, 2013.
2. **Wang, S.**; Sobczynski, D.; Jahanian, P.; Xhahysa, J.; Mao, G. **ACS Appl. Mater. Interfaces**, 5(7), 2699-2707, 2013.
3. Lee, J-S.; Hou, X.; Bishop, N.; **Wang, S.**; Mao, G.; Taatjes, D. J.; Sun, F.; Zhang, K.; Jena, B. P. **Micron [cover]**, 47, 50-58, 2013.
4. **Wang, S.**; Li, L.; Mao, G. **JPCC**, 116, 5492-5498, 2012.
5. **Wang, S.**; Lee, J-S.; Chen, X.; Mao, G.; Taatjes, D. J.; Jena, B. P. **Histochem. Cell Biol. [cover]**, 137(6), 703-718, 2012.
6. Shin, L.; **Wang, S.**; Lee, J.-S.; Flack, A.; Mao, G.; Jena, B. P. **J. Cell Mol. Med.**, 16, 1701-1708, 2012.
7. Song, W.; Markel, D. C.; **Wang, S.**; Mao, G.; Ren, W. **Nanotechnology**, 23, 115101, 2012.
8. Song, W.; Yu, X.; **Wang, S.**; Markel, D. C.; Mao, G.; Ren, W. **Int. J. Nanomedicine**, 6, 3173-3186, 2011.
9. Han, H. J.; Kannan, R. M.; **Wang, S.**; Romero, R.; Mao, G. **Adv. Funct. Mater.**, 19, 1-13, 2009.
10. Zhao, Y.; Xie, Y.; Zhu, X.; Yan, S.; **Wang, S.** **Chemistry - A European Journal**, 14(5), 1601-1606, 2008.

11. Zhao, Y.; Zhu, X.; Huang, Y.; **Wang, S.**; Xie, Y. **JPCC**, 111(33), 12145-12148, 2007.

12. Mao, G.; Sobczynski, D.; **Wang, S.**; Jahanian, P.; Xhahysa, J. Nano-beaker Array Formation Process and Its Use for High-throughput Loading and Crystallization Screening and Other Lab-on-the-chip Applications, **U. S. Patent Trademark Office**, filed on 12/12/2012.

13. 10+ papers and posters presented in AIChE and ACS conferences.

14. Several papers and 1 patent in preparation.

## REFERENCES

- (1) Chondroudis, K.; Mitzi, D. B.: Electroluminescence from an organic-inorganic perovskite incorporating a quaterthiophene dye within lead halide perovskite layers. *Chem. Mater.* **1999**, *11*, 3028-3030.
- (2) Martins, M. A.; Fateixa, S.; Girao, A. V.; Pereira, S. S.; Trindade, T.: Shaping Gold Nanocomposites with Tunable Optical Properties. *Langmuir* **2010**, *26*, 11407-11412.
- (3) Shi, Y.; Yang, R.; Yuet, P. K.: Easy decoration of carbon nanotubes with well dispersed gold nanoparticles and the use of the material as an electrocatalyst. *Carbon* **2009**, *47*, 1146-1151.
- (4) Chen, D.; Wang, R.; Arachchige, I.; Mao, G.; Brock, S. L.: Particle-rod hybrids: Growth of arachidic acid molecular rods from capped cadmium selenide nanoparticles. *J. Am. Chem. Soc.* **2004**, *126*, 16290-16291.
- (5) Fletcher, N. H.: Size Effect in Heterogeneous Nucleation. *Journal of Chemical Physics* **1958**, *29*, 572-576.
- (6) Liu, X. Y.: Generic Progressive Heterogeneous Processes in Nucleation. *Langmuir* **2000**, *16*, 7337-7345.
- (7) Cacciuto, A.; Auer, S.; Frenkel, D.: Onset of heterogeneous crystal nucleation in colloidal suspensions. *Nature* **2004**, *428*, 404-406.
- (8) Turkevich, J.; Stevenson, P. C.; Hillier, J.: A Study of the Nucleation and Growth Processes in the Synthesis of Colloidal Gold. *Discuss. Faraday Soc.* **1951**, 55-&.

(9) Brust, M.; Walker, M.; Bethell, D.; Schiffrin, D. J.; Whyman, R.: Synthesis of Thiol-Derivatized Gold Nanoparticles in a 2-Phase Liquid-Liquid System. *J Chem Soc Chem Comm* **1994**, 801-802.

(10) Frens, G.: Controlled Nucleation for Regulation of Particle-Size in Monodisperse Gold Suspensions. *Nature-Phys Sci* **1973**, *241*, 20-22.

(11) Grabar, K. C.; Freeman, R. G.; Hommer, M. B.; Natan, M. J.: Preparation and Characterization of Au Colloidal Monolayers. *Analytical Chemistry* **1995**, *67*, 735-743.

(12) Goodman, S. L.; Hodges, G. M.; Trejdosiewicz, L. K.; Livingston, D. C.: Colloidal gold markers and probes for routine application in microscopy. *Journal of microscopy* **1981**, *123*, 201-12.

(13) Seo, D.; Park, J. C.; Song, H.: Polyhedral Gold Nanocrystals with  $O_h$  Symmetry: From Octahedra to Cubes. *Journal of the American Chemical Society* **2006**, *128*, 14863-14870.

(14) Zhang, W.-B.; Tu, Y.; Ranjan, R.; Van Horn, R. M.; Leng, S.; Wang, J.; Polce, M. J.; Wesdemiotis, C.; Quirk, R. P.; Newkome, G. R.; Cheng, S. Z. D.: "Clicking" Fullerene with Polymers: Synthesis of [60]Fullerene End-Capped Polystyrene. *Macromolecules* **2008**, *41*, 515-517.

(15) Li, Z.; Jin, R.; Mirkin, C. A.; Letsinger, R. L.: Multiple thiol-anchor capped DNA-gold nanoparticle conjugates. *Nucleic Acids Research* **2002**, *30*, 1558-1562.

(16) Lin, S.-Y.; Tsai, Y.-T.; Chen, C.-C.; Lin, C.-M.; Chen, C.-h.: Two-Step Functionalization of Neutral and Positively Charged Thiols onto Citrate-Stabilized Au Nanoparticles. *J. Phys. Chem. B* **2004**, *108*, 2134-2139.

(17) Chen, S. H.; Kimura, K.: Synthesis and characterization of carboxylate-modified gold nanoparticle powders dispersible in water. *Langmuir* **1999**, *15*, 1075-1082.

(18) Chirea, M.; Pereira, C. M.; Silva, F.: Catalytic effect of gold nanoparticles self-assembled in multilayered polyelectrolyte films. *J. Phys. Chem. C* **2007**, *111*, 9255-9266.

(19) Hiramatsu, H.; Osterloh, F. E.: A Simple Large-Scale Synthesis of Nearly Monodisperse Gold and Silver Nanoparticles with Adjustable Sizes and with Exchangeable Surfactants. *Chemistry of Materials* **2004**, *16*, 2509-2511.

(20) Schmitt, J.; Machtle, P.; Eck, D.; Mohwald, H.; Helm, C. A.: Preparation and Optical Properties of Colloidal Gold Monolayers. *Langmuir* **1999**, *15*, 3256-3266.

(21) Park, J. J.; Lacerda, S. H. D. P.; Stanley, S. K.; Vogel, B. M.; Kim, S.; Douglas, J. F.; Raghavan, D.; Karim, A.: Langmuir Adsorption Study of the Interaction of CdSe/ZnS Quantum Dots with Model Substrates: Influence of Substrate Surface Chemistry and pH. *Langmuir* **2009**, *25*, 443-450.

(22) Handa, H.; Gurczynski, S.; Jackson, M. P.; Auner, G.; Walker, J.; Mao, G.: Recognition of *Salmonella typhimurium* by immobilized phage P22 monolayers. *Surface Science* **2008**, *602*, 1392-1400.

(23) Wan, L.; Manickam, D. S.; Oupicky, D.; Mao, G. Z.: DNA Release Dynamics from Reducible Polyplexes by Atomic Force Microscopy. *Langmuir* **2008**, *24*, 12474-12482.

(24) Bechelany, M.; Maeder, X.; Riesterer, J.; Hankache, J.; Lerose, D.; Christiansen, S.; Michler, J.; Philippe, L.: Synthesis Mechanisms of Organized Gold Nanoparticles: Influence of Annealing Temperature and Atmosphere. *Crystal Growth & Design* **2010**, *10*, 587-596.

(25) Sung, M. G.; Lee, T.-Y.; Kim, B.; Kim, T. H.; Hong, S.: Uniform Patterning of Sub-50-nm-Scale Au Nanostructures on Insulating Solid Substrate via Dip-Pen Nanolithography. *Langmuir* **2010**, *26*, 1507-1511.

(26) Li, J.-R.; Lusker, K. L.; Yu, J.-J.; Garno, J. C.: Engineering the Spatial Selectivity of Surfaces at the Nanoscale Using Particle Lithography Combined with Vapor Deposition of Organosilanes. *ACS Nano* **2009**, *3*, 2023-2035.

(27) Grunes, J.; Zhu, J.; Anderson, E. A.; Somorjai, G. A.: Ethylene Hydrogenation over Platinum Nanoparticle Array Model Catalysts Fabricated by Electron Beam Lithography: Determination of Active Metal Surface Area. *J. Phys. Chem. B* **2002**, *106*, 11463-11468.

(28) Ha, J.-M.; Hamilton, B. D.; Hillmyer, M. A.; Ward, M. D.: Phase Behavior and Polymorphism of Organic Crystals Confined within Nanoscale Chambers. *Crystal Growth & Design* **2009**, *9*, 4766-4777.

(29) Aizenberg, J.; Black, A. J.; Whitesides, G. M.: Control of crystal nucleation by patterned self-assembled monolayers. *Nature* **1999**, *398*, 495-498.

(30) Haiss, W.; Thanh, N. T. K.; Aveyard, J.; Fernig, D. G.: Determination of size and concentration of gold nanoparticles from UV-Vis spectra. *Anal. Chem.* **2007**, *79*, 4215-4221.

(31) Niemeyer, C. M.: Nanoparticles, proteins, and nucleic acids: Biotechnology meets materials science. *Angew. Chem. Int. Ed.* **2001**, *40*, 4128-4158.

(32) Leclere, P.; Surin, M.; Jonkheijm, P.; Henze, O.; Schenning, A. P. H. J.; Biscarini, F.; Grimsdale, A. C.; Feast, W. J.; Meijer, E. W.; Mullen, K.; Bredas, J. L.; Lazzaroni, R.: Organic semi-conducting architectures for supramolecular electronics. *Eur. Polym. J.* **2004**, *40*, 885-892.

(33) Mullen, K.; Rabe, J. P.: Macromolecular and supramolecular architectures for molecular electronics. *Ann Ny Acad Sci* **1998**, *852*, 205-218.

(34) Schenning, A. P. H. J.; Jonkheijm, P.; Hoeben, F. J. M.; van Herrikhuyzen, J.; Meskers, S. C. J.; Meijer, E. W.; Herz, L. M.; Daniel, C.; Silva, C.; Phillips, R. T.; Friend, R. H.; Beljonne, D.; Miura, A.; De Feyter, S.; Zdanowska, M.; Uji-i, H.; De Schryver, F. C.; Chen, Z.; Wurthner, F.; Mas-Torrent, M.; den Boer, D.; Durkut, M.; Hadley, P.: Towards supramolecular electronics. *Synth. Met.* **2004**, *147*, 43-48.

(35) Schenning, A. P. H. J.; Meijer, E. W.: Supramolecular electronics; nanowires from self-assembled pi-conjugated systems. *Chem. Commun.* **2005**, 3245-3258.

(36) Ruadelteixier, A.: Supramolecular Assemblies for Molecular Electronics. *Mol Cryst Liq Crys A* **1994**, *255*, 27-33.

(37) Feldheim, D. L.; Keating, C. D.: Self-assembly of single electron transistors and related devices. *Chem. Soc. Rev.* **1998**, *27*, 1-12.

(38) Shipway, A. N.; Katz, E.; Willner, I.: Nanoparticle arrays on surfaces for electronic, optical, and sensor applications. *Chemphyschem* **2000**, *1*, 18-52.

(39) Zabet-Khosousi, A.; Dhirani, A. A.: Charge transport in nanoparticle assemblies. *Chem. Rev.* **2008**, *108*, 4072-4124.

(40) Wu, Y. Y.; Cheng, G. S.; Katsov, K.; Sides, S. W.; Wang, J. F.; Tang, J.; Fredrickson, G. H.; Moskovits, M.; Stucky, G. D.: Composite mesostructures by nano-confinement. *Nat. Mater.* **2004**, *3*, 816-822.

(41) Israel, L. B.; Kariuki, N. N.; Han, L.; Maye, M. M.; Luo, J.; Zhong, C. J.: Electroactivity Of Cu<sup>2+</sup> at a thin film assembly of gold nanoparticles linked by 11-mercaptopundecanoic acid. *J. Electroanal. Chem.* **2001**, *517*, 69-76.

(42) Riskin, M.; Tel-Vered, R.; Bourenko, T.; Granot, E.; Willner, I.: Imprinting of molecular recognition sites through electropolymerization of functionalized au nanoparticles: Development of an electrochemical TNT sensor based on pi-donor-acceptor interactions. *J. Am. Chem. Soc.* **2008**, *130*, 9726-9733.

(43) Krasteva, N.; Besnard, I.; Guse, B.; Bauer, R. E.; Mullen, K.; Yasuda, A.; Vossmeier, T.: Self-assembled gold nanoparticle/dendrimer composite films for vapor sensing applications. *Nano Lett.* **2002**, *2*, 551-555.

(44) van Herikhuyzen, J.; George, S. J.; Vos, M. R. J.; Sommerdijk, N. A. J. M.; Ajayaghosh, A.; Meskers, S. C. J.; Schenning, A. P. H. J.: Self-



assembled hybrid oligo(p-phenylenevinylene) - Gold nanoparticle tapes. *Angew. Chem. Int. Ed.* **2007**, *46*, 1825-1828.

(45) Besteman, K.; Lee, J. O.; Wiertz, F. G. M.; Heering, H. A.; Dekker, C.: Enzyme-coated carbon nanotubes as single-molecule biosensors. *Nano Lett.* **2003**, *3*, 727-730.

(46) Wang, R.; Li, L.; Arachchige, I.; Ganguly, S.; Brock, S. L.; Mao, G.: Nanoparticles Change the Ordering Pattern of n-Carboxylic Acids into Nanorods on HOPG. *ACS Nano* **2010**, *4*, 6687-6696.

(47) Huo, Q.; Liu, X.; Atwater, M.; Wang, J. H.; Dai, Q.; Zou, J. H.; Brennan, J. P.: A study on gold nanoparticle synthesis using oleylamine as both reducing agent and protecting ligand. *Journal of Nanoscience and Nanotechnology* **2007**, *7*, 3126-3133.

(48) Sagiv, J.: Organized Monolayers by Adsorption. 1. Formation and Structure of Oleophobic Mixed Monolayers on Solid Surfaces. *J. Am. Chem. Soc.* **1980**, *102*, 92-98.

(49) Kessel, C.; Granick, S.: Formation and Characterization of a Highly Ordered and Well-Anchored Alkylsilane Monolayer on Mica by Self-Assembly. *J. Am. Chem. Soc.* **1991**, *7*, 532-538.

(50) Dong, J.; Wang, A.; Ng, K. Y. S.; Mao, G.: Self-assembly of octadecyltrichlorosilane monolayers on silicon-based substrates by chemical vapor deposition. *Thin Solid Films* **2006**, *515*, 2116-2122.

(51) Wasserman, S. R.; Tao, Y. T.; Whitesides, G. M.: Structure and Reactivity of Alkylsiloxane Monolayers Formed by Reaction of Alkyltrichlorosilanes on Silicon Substrates. *Langmuir* **1989**, *5*, 1074-1087.

(52) Wasserman, S. R.; Whitesides, G. M.; Tidswell, I. M.; Ocko, B. M.; Pershan, P. S.; Axe, J. D.: The Structure of Self-Assembled Monolayers of Alkylsiloxanes on Silicon - a Comparison of Results from Ellipsometry and Low-Angle X-Ray Reflectivity. *J. Am. Chem. Soc.* **1989**, *111*, 5852-5861.

(53) Ruhe, J.; Novotny, V. J.; Kanazawa, K. K.; Clarke, T.; Street, G. B.: Structure and Tribological Properties of Ultrathin Alkylsilane Films Chemisorbed to Solid-Surfaces. *Langmuir* **1993**, *9*, 2383-2388.

(54) Legrange, J. D.; Markham, J. L.; Kurkjian, C. R.: Effects of Surface Hydration on the Deposition of Silane Monolayers on Silica. *Langmuir* **1993**, *9*, 1749-1753.

(55) Denkov, N. D.; Velev, O. D.; Kralchevsky, P. A.; Ivanov, I. B.; Yoshimura, H.; Nagayama, K.: Mechanism of Formation of 2-Dimensional Crystals from Latex-Particles on Substrates. *Langmuir* **1992**, *8*, 3183-3190.

(56) Denkov, N. D.; Velev, O. D.; Kralchevsky, P. A.; Ivanov, I. B.; Yoshimura, H.; Nagayama, K.: 2-Dimensional Crystallization. *Nature* **1993**, *361*, 26-26.

(57) Li, J. R.; Garno, J. C.: Elucidating the role of surface hydrolysis in preparing organosilane nanostructures via particle lithography. *Nano Lett.* **2008**, *8*, 1916-1922.

(58) Lusker, K. L.; Yu, J. J.; Garno, J. C.: Particle lithography with vapor deposition of organosilanes: A molecular toolkit for studying confined surface reactions in nanoscale liquid volumes. *Thin Solid Films* **2011**, *519*, 5223-5229.

(59) Briseno, A. L.; Mannsfeld, S. C. B.; Ling, M. M.; Liu, S. H.; Tseng, R. J.; Reese, C.; Roberts, M. E.; Yang, Y.; Wudl, F.; Bao, Z. N.: Patterning organic single-crystal transistor arrays. *Nature* **2006**, *444*, 913-917.

(60) Cheng, W. L.; Park, N. Y.; Walter, M. T.; Hartman, M. R.; Luo, D.: Nanopatterning self-assembled nanoparticle superlattices by moulding microdroplets. *Nat. Nanotechnol.* **2008**, *3*, 682-690.

(61) Courty, A.; Mermet, A.; Albouy, P. A.; Duval, E.; Pileni, M. P.: Vibrational coherence of self-organized silver nanocrystals in f.c.c. supra-crystals. *Nat. Mater.* **2005**, *4*, 395-398.

(62) Mao, G.; Chen, D.; Handa, H.; Dong, W.; Kurth, D. G.; Mohwald, H.: Deposition and aggregation of aspirin molecules on a phospholipid bilayer pattern. *Langmuir* **2005**, *21*, 578-585.

(63) Mao, G.; Dong, W.; Kurth, D. G.; Mohwald, H.: Synthesis of copper sulfide nanorod arrays on molecular templates. *Nano Lett.* **2004**, *4*, 249-252.

(64) Zhong, Z.; Gates, B.; Xia, Y.; Qin, D.: Soft lithographic approach to the fabrication of highly ordered 2D arrays of magnetic nanoparticles on the surfaces of silicon substrates. *Langmuir* **2000**, *16*, 10369-10375.

(65) Dong, W.; Wang, R.; Mao, G.; Mohwald, H.: Self-assembled molecular patterns of fatty acid on graphite in the presence of metal ions. *Soft Matter* **2006**, *2*, 686-692.

- (66) Wang, S.; Li, L.; Mao, G.: Formation of Carboxylic Acid Nanorods on Oleylamide-Capped Au Nanoparticles. *J. Phys. Chem. C* **2012**, *116*, 5492-5498.
- (67) Cassie, A. B. D.: Contact Angles. *Discuss. Faraday Soc.* **1948**, *3*, 11-16.
- (68) Wu, B.; Mao, G.; Ng, K. Y. S.: Stepwise adsorption of a long trichlorosilane and a short aminosilane. *Colloids Surf., A* **2000**, *162*, 203-213.
- (69) Chen, J.; Liao, W. S.; Chen, X.; Yang, T.; Wark, S.; Son, D. H.; Batteas, J. D.; Cremer, P. S.: Evaporation-Induced Assembly of Quantum Dots into Nanorings. *Acs Nano* **2009**, *3*, 173-180.
- (70) Dong, J.: Self-assembly of octadecyltrichlorosilane monolayers on silicon-based substrates by chemical vapor deposition. *Thin Solid Films* **2006**, *515*, 2116-2122.
- (71) Wasserman, S.; Tao, Y.; Whitesides, G.: Structure and Reactivity of Alkylsiloxane Monolayers Formed by Reaction of Alkyltrichlorosilanes on Silicon Substrates. *Journal of the American Chemical Society* **1989**, *5*, 1074-1087.
- (72) Hair, M. L.; Hertl, W.: Reactions of Chlorosilanes with Silica Surfaces. *J. Phys. Chem.* **1969**, *73*, 2372-&.
- (73) Angst, D. L.; Simmons, G. W.: Moisture Absorption Characteristics of Organosiloxane Self-Assembled Monolayers. *Langmuir* **1991**, *7*, 2236-2242.
- (74) Fadeev, A. Y.; McCarthy, T. J.: Self-assembly is not the only reaction possible between alkyltrichlorosilanes and surfaces: Monomolecular and

oligomeric covalently attached layers of dichloro- and trichloroalkylsilanes on silicon. *Langmuir* **2000**, *16*, 7268-7274.

(75) Ashurst, W. R.; Carraro, C.; Maboudian, R.: Vapor phase anti-stiction coatings for MEMS. *IEEE Trans. Device Mater. Reliab.* **2003**, *3*, 173-178.

(76) Ahn, W.; Roper, D. K.: Periodic Nanotemplating by Selective Deposition of Electroless Gold Island Films on Particle-Lithographed Dimethyldichlorosilane Layers. *Acs Nano* **2010**, *4*, 4181-4189.

(77) Takei, T.; Mukasa, K.; Kofuji, M.; Fuji, M.; Watanabe, T.; Chikazawa, M.; Kanazawa, T.: Changes in density and surface tension of water in silica pores. *Colloid Polym. Sci.* **2000**, *278*, 475-480.

(78) Asay, D. B.; Kim, S. H.: Evolution of the adsorbed water layer structure on silicon oxide at room temperature. *J. Phys. Chem. B* **2005**, *109*, 16760-16763.

(79) Aizenberg, J.: Crystallization in patterns: A bio-inspired approach. *Adv. Mater.* **2004**, *16*, 1295-1302.

(80) Frens, G.: Particle-Size and Sol Stability in Metal Colloids. *Kolloid Z Z Polym* **1972**, *250*, 736-&.

(81) Kimling, J.; Maier, M.; Okenve, B.; Kotaidis, V.; Ballot, H.; Plech, A.: Turkevich method for gold nanoparticle synthesis revisited. *J. Phys. Chem. B* **2006**, *110*, 15700-15707.

(82) Liu, X. O.; Atwater, M.; Wang, J. H.; Huo, Q.: Extinction coefficient of gold nanoparticles with different sizes and different capping ligands. *Colloid Surface B* **2007**, *58*, 3-7.

(83) Albanese, A.; Chan, W. C. W.: Effect of Gold Nanoparticle Aggregation on Cell Uptake and Toxicity. *Acs Nano* **2011**, *5*, 5478-5489.

(84) Chithrani, B. D.; Ghazani, A. A.; Chan, W. C. W.: Determining the size and shape dependence of gold nanoparticle uptake into mammalian cells. *Nano Lett.* **2006**, *6*, 662-668.

**ABSTRACT****ENGINEERING NANOPARTICLE AND NANORING PATTERNS FOR THE STUDY OF MOLECULAR CRYSTALLIZATION UNDER NANOCONFINEMENT**

by

SUNXI WANG

August 2013

**Advisor:** Dr. Guangzhao Mao**Major:** Chemical Engineering**Degree:** Doctor of Philosophy

This dissertation focuses on generating the inorganic nanoparticle/organic nanorod hybrid nanostructures by the strategy of nanoparticle induced molecular crystallization developed by us. We synthesize the gold nanoparticles with different sizes and functional groups and then fabricate the nanohybrids with fatty acid nanorods by spin coating method. Atomic force microscope monitors the topography of the hybrid nanostructures to help understand the underlying mechanism of the crystallization process. This successful self-assembled method could be used to fabricate nanohybrids based on seed-mediated nucleation. Also the novel "nano-flasks" have been generated by particle lithography method, which could be served for nanoconfining drug crystals and be used in high throughput screening applications. Both nanoparticles (convex) and nanoring patterns (concave) serve as two different systems for molecular crystallizations.

**AUTOBIOGRAPHICAL STATEMENT**

SUNXI WANG

## Education

- Ph. D., Chemical Engineering, Department of Chemical Engineering and Materials Science, Wayne State University, Detroit, MI, 2013
- M. S., Chemical Engineering, Department of Chemical Engineering and Materials Science, Wayne State University, Detroit, MI, 2012
- B. S., Material Chemistry, School of Chemistry and Materials Science, University of Science and Technology of China, Hefei, China, 2007

## Experience

- 09/2008 - Present, Graduate Research/Teaching Assistant, Department of Chemical Engineering and Materials Science, Wayne State University, Detroit, MI
- 09/2007 - 08/2008, Graduate Teaching Assistant, Department of Chemistry, Wayne State University, Detroit, MI
- 09/2005 - 07/2007, Research Assistant, National Laboratory for Physical Sciences at Microscale, University of Science and Technology of China, Hefei, China